

**REAL-TIME MONITORING OF EXPOSURE CONTROLLED  
PROJECTION LITHOGRAPHY (ECPL) PROCESS**

A Thesis  
Presented to  
The Academic Faculty

by

Changxuan Zhao

In Partial Fulfillment  
of the Requirements for the Degree  
Master of Science in Mechanical Engineering

Georgia Institute of Technology  
August 2017

**COPYRIGHT © 2017 BY CHANGXUAN ZHAO**

**REAL-TIME MONITORING OF EXPOSURE CONTROLLED  
PROJECTION LITHOGRAPHY (ECPL) PROCESS**

Approved by:

Dr. David W. Rosen, Advisor  
School of Mechanical Engineering  
*Georgia Institute of Technology*

Dr. Amit S. Jariwala  
School of Mechanical Engineering  
*Georgia Institute of Technology*

Dr. Suresh K. Sitaraman  
School of Mechanical Engineering  
*Georgia Institute of Technology*

Date Approved: April 26, 2017

## ACKNOWLEDGEMENTS

I would like to take this opportunity to express my sincere appreciation to my Master advisor, Dr. David W. Rosen for providing me a great research opportunity to challenge myself. His patience on me, and his willingness to help and share as an advisor with abounding experience, have comprehensively supported and inspired me through my persuasion of my thesis study. I would also like to express my cordial thanks to my co-advisor, Dr. Amit S. Jariwala, for guiding me through the project. I appreciate Dr. Jariwala for his support, wisdom, and prevailing confidence in me. I feel very fortunate to have been able to work with Dr. Rosen and Dr. Jariwala.

I would like to thank Dr. Suresh K. Sitaraman for being my reading committee member for this thesis. I appreciate for his time and effort in helping me improve my dissertation. I would also like to thank Dr. Wenshan Cai for his advice in my ICM system equipment setup. His rich experience in optics helped greatly helped me when I consulted him for my system equipment setup.

I would like to thank Dr. Xiayun Zhao, one of my labmate who work on the similar project, for her significant help to me in my signal decoding algorithm. I was fortunate to have the opportunity to work with the other labmates including Harrison Jones, Ying Zhang, Bereket Tebikew, and Jenny Wang, who contributed a lot to this project. I would also like to thank the other people in Dr. Rosen's research group (Mahmoud Dinar, John-Travis Hansen, Chad Hume, Sang-in Park, Narumi Watanabe, Yeming Xian and everyone else), for their help in all things research and non-research.

I thank all my friends at home and abroad for their friendship and support non-research.

Finally, I would greatly like to thank my parents. They have been educating, supporting, and encouraging me throughout my entire life mentally, physically and financially in every aspect of my life.

# TABLE OF CONTENTS

<b>ACKNOWLEDGEMENTS</b>	<b>iii</b>
<b>LIST OF TABLES</b>	<b>vii</b>
<b>LIST OF FIGURES</b>	<b>viii</b>
<b>LIST OF SYMBOLS AND ABBREVIATIONS</b>	<b>xii</b>
<b>SUMMARY</b>	<b>xiii</b>
<b>CHAPTER 1. Introduction &amp; Motivation</b>	<b>1</b>
<b>1.1 Introduction</b>	<b>2</b>
1.1.1 Mask Projection Micro-stereolithography	2
1.1.2 Interferometer	5
<b>1.2 ECPL and ICM Process Overview</b>	<b>11</b>
<b>1.3 Motivation of Study</b>	<b>14</b>
<b>1.4 Research Objective</b>	<b>15</b>
<b>1.5 Organization of This Thesis</b>	<b>16</b>
<b>CHAPTER 2. Literature review and research problem statement</b>	<b>17</b>
<b>2.1 Photopolymerization Model and Process Planning Method</b>	<b>17</b>
<b>2.2 Existing Monitoring Methods for Additive Manufacturing Processes</b>	<b>20</b>
<b>2.3 Existing Monitoring and Controlling Methods for ECPL System</b>	<b>28</b>
<b>2.4 Research Questions and Hypothesis</b>	<b>43</b>
<b>2.5 Chapter Summary</b>	<b>44</b>
<b>CHAPTER 3. EXISTING ECPL and ICM SYSTEM DESIGN AND EXPERIMENT PROCEDURE</b>	<b>46</b>
<b>3.1 Existing System Design</b>	<b>46</b>
<b>3.2 Experimental Procedure and Resultant Samples</b>	<b>48</b>
<b>3.3 Chapter Summary</b>	<b>54</b>
<b>CHAPTER 4. improved icm system and working procedure</b>	<b>55</b>
<b>4.1 Improved ECPL and ICM System</b>	<b>55</b>
<b>4.2 Revised Experimental Procedure</b>	<b>64</b>
4.2.1 ICM System Alignment and Contrast Check	64
4.2.2 Time-varying Scanning Method and ICM Detecting Frame Identification Procedure	68
4.2.3 Signal Processing Procedure	79
<b>4.3 Chapter Summary</b>	<b>83</b>
<b>CHAPTER 5. Experimental Validation</b>	<b>84</b>
<b>5.1 Experimental Validation and Analysis</b>	<b>84</b>
5.1.1 Experiment 5.1.1: Using Time-varying ICM Scanning Method to Determine Multiple Heights in One Sample	84

5.1.2	Experiment 5.1.2: Using Time-varying ICM Scanning Method to Determine 1D Lateral Dimension with High Resolution	91
5.2	Error Analysis	96
5.3	Limitations	110
5.4	Chapter Summary	111
<b>CHAPTER 6. closure and recommendations</b>		<b>113</b>
6.1	Summary of the Thesis	113
6.2	Evaluation of Hypothesis	115
6.3	Contributions	117
6.4	Future Work	120
<b>APPENDIX A. Matlab codes</b>		<b>123</b>
A.1	MATLAB Code for Controlling the SLM	123
A.2	MATLAB Code for Convert the Contrastness of ICM Gathered Video	123
A.3	MATLAB Code for Splitting the ICM Gathered Video	124
<b>REFERENCES</b>		<b>127</b>

## LIST OF TABLES

Table 1	– Phase Components of the Multi-beam Interference Optics Model in ICM [40]	38
Table 2	– Average Value and Standard Deviation of Height 1 and Height 2 Measured by ICM System and Confocal Microscope	90
Table 3	– Length 1 and Length 2 Measured by ICM System and Confocal Microscope	91
Table 4	– Estimated and Measured Part Widths	96
Table 5	– Errors and Percentage Errors for the ICM Measurements of Length 1 and Length 2 in Experiment 5.1.1	97
Table 6	– Errors and Percentage Errors for the ICM Measurements of Height 1 and Height 2 in Experiment 5.1.1	98
Table 7	– Errors and Percentage Errors for the ICM Measurements of Cured Part Widths in Experiment 5.1.2	98
Table 8	– Allowable Error Sources and Corresponding Error Contributions for ICM Edge Detection	102
Table 9	– Allowable Error Sources and Corresponding Error Contributions for ICM Height Measurements	105
Table 10	– Comparison Between the New ICM System Developed in This Thesis and the Alternative ICM System Developed by Zhao X. et al. [51]	109

## LIST OF FIGURES

Figure 1	– Schematic of A Mask Projection Micro-Stereolithography Process [3]	--3
Figure 2	– Photos of Carbon3D M2 (left) [10], Rapidshape D40 II (middle) [13], and Formlabs Form 2 [14]	--4
Figure 3	– A Schematic of Mach-Zehnder Interferometer [16]	--5
Figure 4	– A Photo of Zygo NewView 8000 Optical Surface Profiler [17]	--7
Figure 5	– Top View of the Mach-Zehnder Interferometer System Proposed by Lightman et al. [16]	--8
Figure 6	– Side View (View A-A in Figure 5) of the Mach-Zehnder Interferometer System Proposed by Lightman et al. [16]	--8
Figure 7	– The Mach-Zehnder Interferometer System Proposed by Tran-Cong-Miyata et al. [19]	--10
Figure 8	– Schematic of the Michelson Interferometer System Proposed by Dudi et al. [27]	--11
Figure 9	– Block Diagram of ECPL and ICM System	--12
Figure 10	– Schematic of the ICM System and Resin Chamber [9]	--12
Figure 11	– Block Diagram of Process Planning Method Utilized In ECPL System	--20
Figure 12	– A Schematic of SRAS [34]	--21
Figure 13	– Schematic of OCT Used by Lewis et al. [37]	--23
Figure 14	– Schematic of SAM System [49]	--26
Figure 15	– ICM-Captured Interferogram by Jariwala et al. [9]	--29
Figure 16	– Flow Chart of the Close-loop Control Using the ICM System [39]	--31
Figure 17	– Overview of the ICM System and the ECPL System [39]	--32
Figure 18	– Experiment Done by Jones et al. to Show the Limitation of ICM with Large Laser Beam [24]	--33

Figure 19	– Experiment Results Done by Jones et al. to Show the Limitation of ICM with Large Laser Beam [24]	--34
Figure 20	– A Schematic of Noise Signal Generation Due To Internal Reflections Proposed by Jones et al. [24]	--36
Figure 21	– Detailed ICM Laser Reflection Model by Zhao, X. et al. [40]	--37
Figure 22	– Schematic of the Original ICM System (Y axis is perpendicular into the paper)	--46
Figure 23	– The Original ECPL and ICM System [42]	--47
Figure 24	– Schematic of Resin Chamber Preparation Procedure	--49
Figure 25	– Schematic of the Prepared Resin Chamber [33]	--50
Figure 26	– Schematic of Washing Process	--51
Figure 27	– Desired Feature Fabricated By ECPL System Sample 1 (Left: Measurement from Confocal Microscope; Right: Measurement from Optical Microscope)	--53
Figure 28	– Desired Feature Fabricated By ECPL System Sample 2 (Left: Measurement from Confocal Microscope; Right: Measurement from Optical Microscope)	--53
Figure 29	– Desired Feature Fabricated By ECPL System Sample 3 (Left: Measurement from Confocal Microscope; Right: Measurement from Optical Microscope)	--54
Figure 30	– Schematic of ECPL system and ICM system (Y axis is perpendicular into the paper) [46]	--56
Figure 31	– Photo of the ECPL System	--56
Figure 32	– Photograph showing the experimental ICM System Setup (Y axis is perpendicular into the paper) [46]	--59
Figure 33	– Top Figure: Light Passing Through a Convex Lens Without Spherical Aberration; Bottom Figure: Light Passing Through a Convex Lens With Spherical Aberration [45]	--62
Figure 34	– A Schematic of The “Un-Collimated” Light Path When the Laser Passed The Spatial Filter Consisting Of Two Normal Convex Lenses	--63
Figure 35	– A Zoomed-in View of Section A in Figure 34.	--63

Figure 36	– First Set of ICM Detecting Locations on the ICM Video	--70
Figure 37	– An Example of Overly-exposed Interferogram and Its Corresponding Adequately-exposed Interferogram	--71
Figure 38	– An Example of “Blurred” ICM Video Frame	--73
Figure 39	– The Original ICM Video Frame of Figure 36	--74
Figure 40	– Comparison Between Converted Interferogram and Original Interferogram	--75
Figure 41	– Second Set of ICM Detecting Locations on the Converted ICM Video	--77
Figure 42	– Third Set of ICM Detecting Locations on the Converted ICM Video	--77
Figure 43	– Fourth Set of ICM Detecting Locations on the Converted ICM Video	--78
Figure 44	– Fifth Set of ICM Detecting Locations on the Converted ICM Video	--78
Figure 45	– Sixth Set of ICM Detecting Locations on the Converted ICM Video	--79
Figure 46	– Flow Chart of the ICM Signal Processing Procedure	--82
Figure 47	– Curing Profiles and Exposure Times Used to Fabricate 8 Samples in Experiment 5.1.1	--85
Figure 48	– 3D View of the Expected Cured Sample and Measured Parameters in Experiment 5.1.1	--85
Figure 49	– Height Distribution vs Length in X Direction of Sample 1	--87
Figure 50	– Height Distribution vs Length in X Direction of Sample 2	--87
Figure 51	– Height Distribution vs Length in X Direction of Sample 3	--88
Figure 52	– Height Distribution vs Length in X Direction of Sample 4	--88
Figure 53	– Height Distribution vs Length in X Direction of Sample 5	--89
Figure 54	– Height Distribution vs Length in X Direction of Sample 6	--89
Figure 55	– Height Distribution vs Length in X Direction of Sample 7	--90

Figure 56 – Interferograms at Point 20, 28, and 30	--92
Figure 57 – Resultant Number of Oscillation Periods Among the Monitored Points	--93
Figure 58 – Zoomed In View of Figure 57 for the Section A	--93
Figure 59 – Zoomed In View of Figure 57 for the Section B	--94

## LIST OF SYMBOLS AND ABBREVIATIONS

ECPL	Exposure Controlled Projection Lithography
ICM	Interferometric Cure Monitoring
SLM	Spatial Light Modulator
UV	Ultra Violet
3D	Three-dimensional
DMD	Digital Micrometer Device
SFIP1	SLM Frame Indicator Position of 1 <sup>st</sup> Set of ICM Detecting Locations
TISFIP1	Threshold Intensity of the 1 <sup>st</sup> SLM Frame Indicator Position
TIVF	The Timestep of the Current ICM Video Frame
ISFIP1	Average Intensity at the 1 <sup>st</sup> SLM Frame Indicator Positions
IIDP1	Intensity Values of the 1 <sup>st</sup> Set of ICM Detecting Locations
SICMV1	1 <sup>st</sup> Sub-video of the ICM Video
PIDL1	Total Phase Angle Change at the 1 <sup>st</sup> ICM Detecting Location
HIDL1	Estimated Cured Part Height at the 1 <sup>st</sup> ICM Detecting Location

## SUMMARY

Exposure Controlled Projection Lithography (ECPL) is a stereolithographic based additive manufacturing process in which photopolymer resin is used to fabricate lens shaped features. During this process, a dynamic mask projects radiation patterns through a transparent substrate onto the photopolymer resin to grow features from the substrate surface. The Interferometric Cure Monitoring (ICM) system utilizes the principle of Mach-Zehnder interferometer to measure the change in refractive index of the photopolymer resin. Previous monitoring systems for the ECPL process have only focused on thickness measurement of the fabricated parts with homogeneous thickness, and no measurements regarding lateral dimensions of the fabricated parts have been investigated. For this thesis study, an ICM system has been developed for measuring both height and lateral dimensions of the part fabricated by the ECPL process.

This thesis contains six chapters. Chapter 1 introduces the knowledge related to the ECPL and ICM system. Chapter 2 presents the existing monitoring and controlling methods for ECPL system based on literature review, and the research question and hypothesis are presented. Chapter 3 and chapter 4 presented the original and improved ICM systems and the experimental procedure. Chapter 4 also presents the time-varying scanning method developed in this thesis study. Chapter 5 discusses the experimental validation experiments for the research hypothesis. The error sources and limitations uncovered by the validation experiments are discussed in Chapter 5. Chapter 6 summarizes the thesis and evaluates the research question and hypothesis. In addition, future work for this research is proposed in Chapter 6.

## CHAPTER 1. INTRODUCTION & MOTIVATION

Exposure Controlled Projection Lithography (ECPL) a stereolithographic process, based on Mask Projection Micro Stereolithography (MP $\mu$ SLA), in which photopolymer resin is used to fabricate features in micro-scale. These fabricated features are aimed for micro-optics applications. Interferometric Cure Monitoring (ICM) utilizes the principles of interferometry to track the changes in refractive index within the resin chamber in real time, and the ICM system can be used to monitor frontal polymerization processes. With this ICM system, better understandings on the photopolymerization process during the ECPL fabrication process could be gathered with real-time signals gathered by the ICM system. In addition, the information gathered by the ICM system could serve as the real-time feedback for a close-loop control for the ECPL process which could improve the precision for the features fabricated by the ECPL process. The motivation for this study is to develop an ICM system that could monitor the fabrication process and help the accuracy of the fabrication process.

The following section will provide an introduction and background to mask projection micro-stereolithography which leads to the ECPL system. The background to the interferometer will also be introduced, which is the theoretical foundation of the ICM system. The motivation for the study will be further explained in Section 1.3. The research objective is investigated in Section 1.4. Section 1.5 will present the organization of the thesis.

## 1.1 Introduction

### 1.1.1 Mask Projection Micro-stereolithography

Stereolithography is a type of additive manufacturing process. In 1981, Dr. Hideo Kodama first published the modern layered approach to stereolithography by using ultraviolet light to cure photo-hardening polymers [1]. In 1986, the published patent by Charles W. Hull, “Apparatus for production of three-dimensional objects by stereolithography”, firstly defined the term “stereolithography” as a method to fabricate 3D features by successively using UV to fabricate layers of photopolymers [2]. Micro-stereolithography is a stereolithographic process used to fabricate features in micro-scale. Mask projection micro-stereolithography is a type of micro-stereolithography. The mask projection micro-stereolithography is unique from micro-stereolithography since the entire cross-section layers are cured at the same instant during the mask projection micro-stereolithography, whereas the micro-stereolithography processes usually use a point curing laser to fabricate each cross-section layer point by point. Since the mask-projection micro-stereolithography process eliminates the laser’s XY movement, the error caused from the movement is reduced.

As an example, Figure 1. Schematic of A Mask Projection Micro-Stereolithography Process [3] presents the schematic of the mask projection micro-stereolithography process proposed by Sun et al [3]. The desired 3D feature, represented by CAD model, is imputed into the controlling computer. The computer utilize slicing method to decompose the input 3D model into thin layers. When the 3D feature is fabricated, the computer controls the

Digital Micromirror Device (DMD) to control the curing profile for fabricating each layer, and the 3D feature is fabricated layer by layer from bottom to top [3].

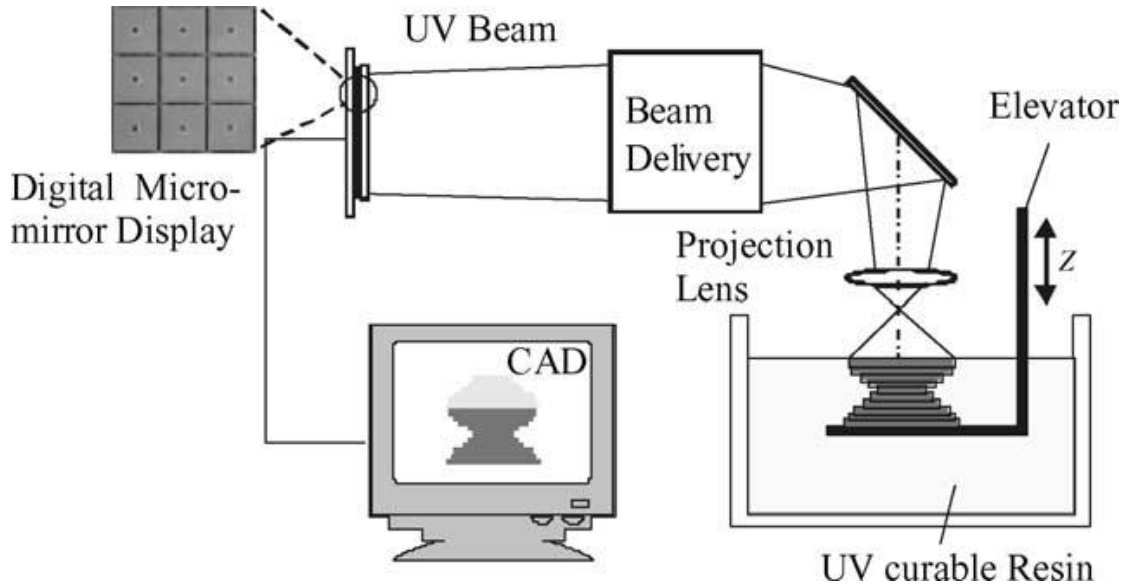


Figure 1. Schematic of A Mask Projection Micro-Stereolithography Process [3]

In addition, Limaye & Rosen [4], Chatwin [5], Monneret et al. [6], Jariwala et al. [7], and Zheng et al. [8] investigated building 3D features with dynamic masks which control the radiating patterns of the exposure light source onto photopolymer resins. Jariwala et al. proposed the ECPL system [9]. The ECPL system controls the curing light source with dynamic masks and projects this curing source into the resin chamber.

Through literature review, mask projection stereolithography has been commercialized for industrial applications. Examples include M2 from Carbon3D, D40 II from Rapidshape, and Form 2 from Formlabs. Figure 2 shows the photos of M2, D40II, and Form 2. The M2 from Carbon 3D is proposed to be ideal for “functional prototyping and low volume manufacturing”. The M2 has a build volume of 7.5 x 4.6 x 12.8 inch [10].

The M2 utilizes the Continuous Liquid Interface Production (CLIP) technology, which belongs to the category of mask projection stereolithography. The features fabricated by M2 can have Young's modulus up to 250-280 MPa. With heat treatment, the treated features fabricated by M2 can have Young's modulus up to 3800-4000 MPa [11]. The D40 II from Rapidshape has building volume of 2 x 130 x 75 mm. The curing light source is 385 nm UV LED, and the resolution of the machine is 34  $\mu\text{m}$  native pixel [12]. The D40 II is suggested to fabricate resin prototypes for dental indications [13]. The Form 2 from Formlabs features building volume of 145 x 145 x 175 mm, the resolution in the lateral directions on the layer surface is 140  $\mu\text{m}$ , and the layer thickness ranges from 25 -100  $\mu\text{m}$ .



Figure 2. Photos of Carbon3D M2 (left) [10], Rapidshape D40 II (middle) [13], and Formlabs Form 2 [14]

### 1.1.2 Interferometer

Interferometry is a family of techniques in which interference, caused by several waves superimposed together, is measured to gather information [15]. The ICM system in this thesis utilize the principle of Mach-Zehnder interferometer. The Mach-Zehnder interferometer is used to determine the relative phase shift between two collimated beams being split from the same source. Figure 3 shows a schematic of a Mach-Zehnder interferometer.

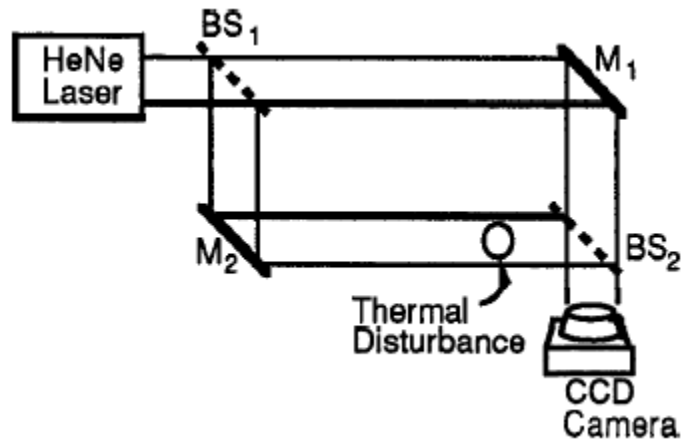


Figure 3. A Schematic of Mach-Zehnder Interferometer [16]

As shown in Figure 3, the collimated laser beams are originated from the HeNe laser diode. After passing the first beam splitter (BS<sub>1</sub>), the laser beams are split into two sub-beams, one travelling towards Mirror 1 (M<sub>1</sub>) at the top right and the other travelling towards Mirror 2 (M<sub>2</sub>) at the bottom left. After the sub-beams get reflected by the mirrors, the corresponding two sub-beams from the same collimated laser beams are superimposed at the second beam splitter (BS<sub>2</sub>), and superimposed beams are captured by the CCD camera. The optical path of the two sub-beams towards to M<sub>1</sub> and M<sub>2</sub> are the all the same except

there is a thermal disturbance in the path between  $M_2$  and  $BS_2$  which changes the optical properties of the path between  $M_2$  and  $BS_2$ . Thus, there will be phase difference between the sub-beam travelling through  $BS_1 \rightarrow M_1 \rightarrow BS_2$  and the sub-beam travelling through  $BS_1 \rightarrow M_2 \rightarrow BS_2$ , although these two sub-beams, split by  $BS_1$ , are originated from the same laser beam from the HeNe laser source. As a result, the laser profile captured by the CCD camera will exist fringe patterns.

From literature review, the principle of interferometry is widely used to measure small displacements and changes in refractive indices. A commercialized example is the Zygo NewView 8000 optical surface profiler which is used to gather 3D distribution of a sample's surface. According to Zygo, the NewView 8000 can gather sample height from  $< 1$  nm up to  $20,000 \mu\text{m}$  [17]. With the 100X magnification factor using the principle of Mirau interferometer, the optical resolution can be  $0.34 \mu\text{m}$ , and the maximum slope that the profiler can measure is  $40.36$  degree [18]. Figure 4 shows a photo of the Zygo NewView 8000 optical surface profiler.



Figure 4. A Photo of Zygo NewView 8000 Optical Surface Profiler [17]

The interferometry is also widely used for monitoring the refractive index of the cured sample. Lightman et al. has proposed the Mach-Zehnder interferometer, as shown in Figure 5 and Figure 6, to monitor the change in refractive index during the stereolithographic processes.

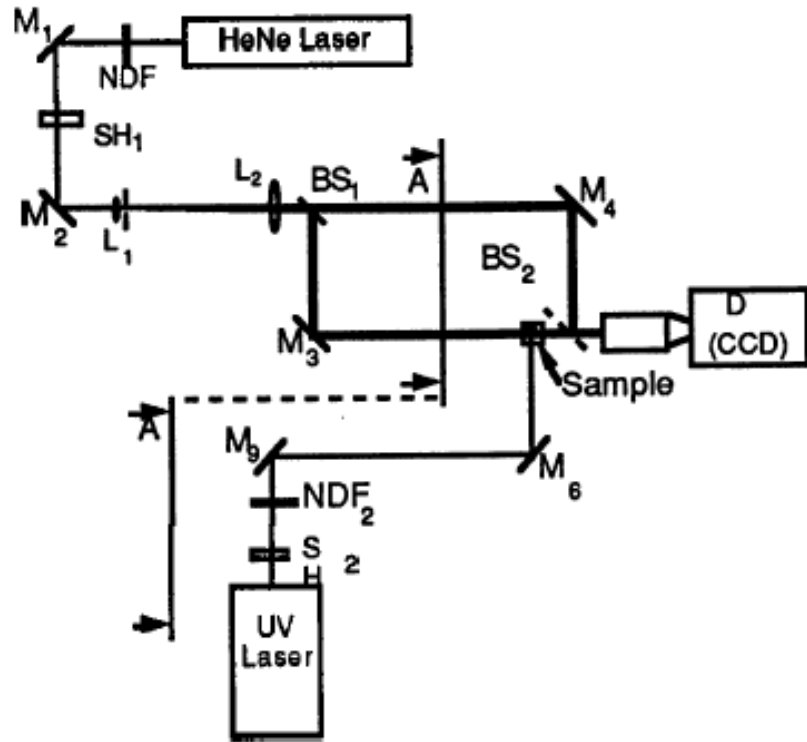


Figure 5. Top View of the Mach-Zehnder Interferometer System Proposed by Lightman et al. [16]

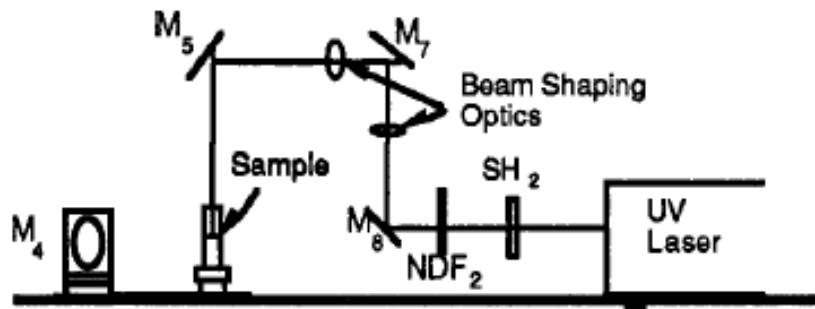


Figure 6. Side View (View A-A in Figure 5) of the Mach-Zehnder Interferometer System Proposed by Lightman et al. [16]

As shown in Figure 5, during the stereolithographic process, the UV laser passes through the projection system to cure the sample (UV Laser  $\rightarrow$  M<sub>9</sub>  $\rightarrow$  M<sub>6</sub>  $\rightarrow$  Sample). The collimated detecting laser beam from the HeNe laser source passes through the designed interferometer system composed of BS<sub>1</sub>, M<sub>3</sub>, M<sub>4</sub>, and BS<sub>2</sub>, and the re-combined laser profile is captured by the CCD camera. During the curing process, the cured sample changes the refractive index, and this change causes the change in optical path between M<sub>3</sub> and BS<sub>2</sub>. As a result, there will be phase changes in the interference patterns received by the CCD camera. By analyzing these phase changes, the change in refractive index could be gathered [16]. As shown in Figure 7, the Mach-Zehnder interferometer system is proposed by Tran-Cong-Miyata et al. to monitor the local deformation during the stereolithographic process [19] [20]. The detecting laser beam split into two sub-beams. The reference sub-beam has the optical path HM1  $\rightarrow$  M1  $\rightarrow$  HM2  $\rightarrow$  CCD camera, and the measuring sub-beam has the optical path HM1  $\rightarrow$  M2  $\rightarrow$  Sample  $\rightarrow$  HM2  $\rightarrow$  CCD camera. Compare with this interferometer system, the ICM system discussed in this thesis study has less optical components and features a simpler design, which will be discussed later.

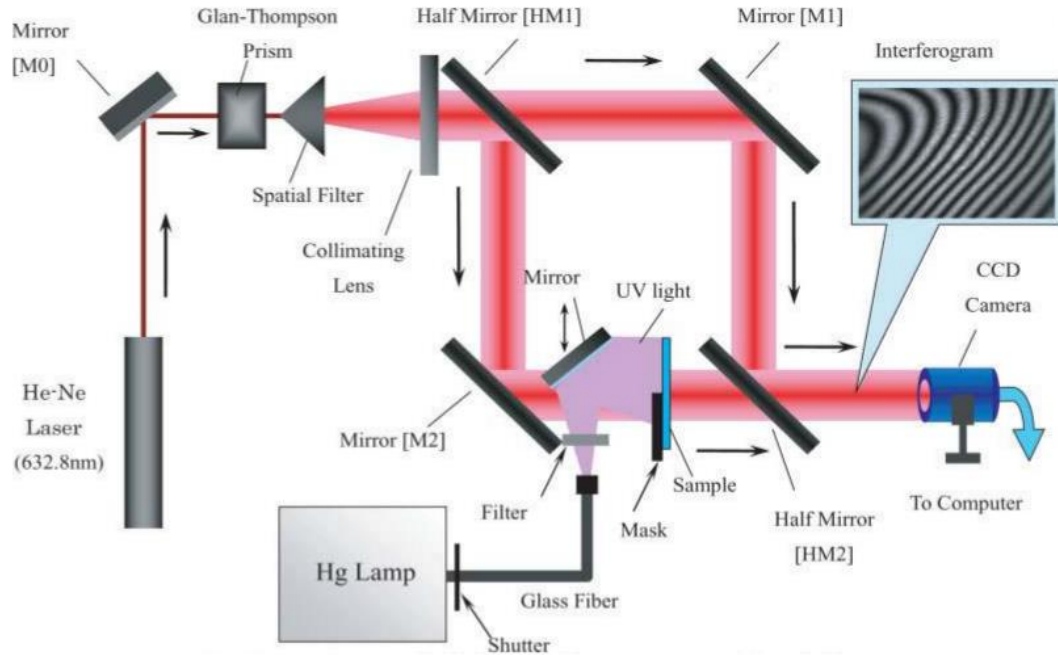


Figure 7. The Mach-Zehnder Interferometer System Proposed by Tran-Cong-Miyata et al. [19]

In addition to Mach-Zehnder interferometer, the Michelson interferometer has also been developed to monitor the change in refractive index and to monitor the photopolymerization during the stereolithography process. As an example, Figure 8 shows the schematic of the Michelson interferometer system proposed by Dudi et al. The total cost for the hardware component of the interferometer system proposed by Dudi et al., excluding the UV source and the signal detectors, is about \$1800 [27].

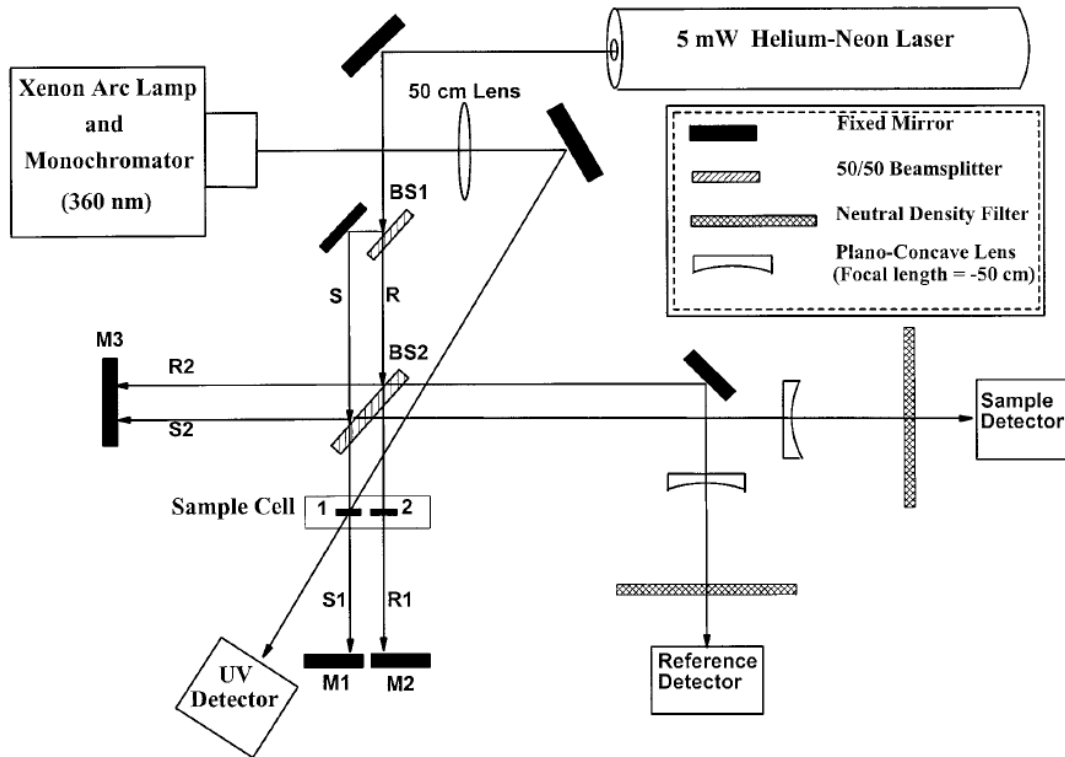


Figure 8. Schematic of the Michelson Interferometer System Proposed by Dudi et al. [27]

## 1.2 ECPL and ICM Process Overview

Jariwala et al. proposed the ECPL system [9]. Figure 9 shows a block diagram of the ECPL system and the ICM system. The ICM blocks involving the ICM system are indicated by green background. Figure 10 shows a schematic of the ICM system with the resin chamber.

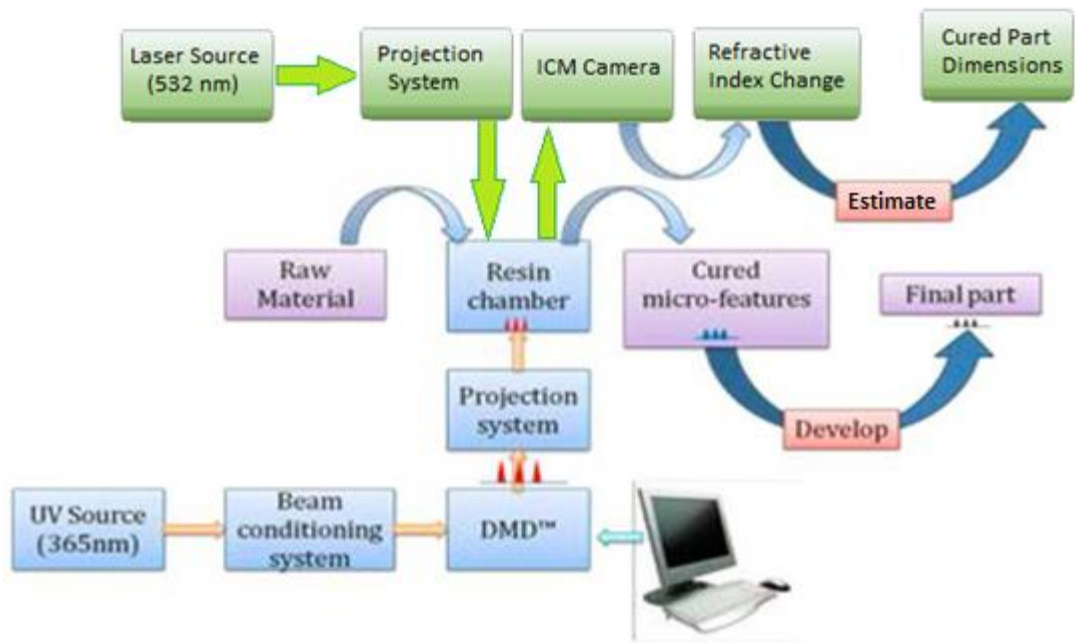


Figure 9. Block Diagram of ECPL and ICM System

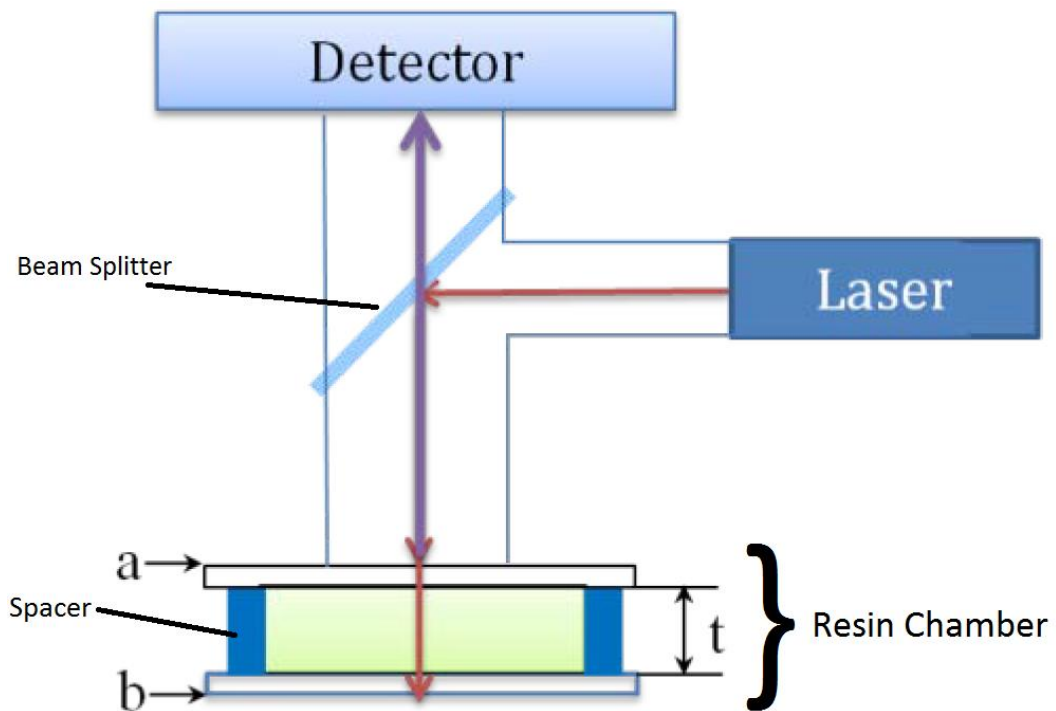


Figure 10. Schematic of the ICM System and Resin Chamber [9]

The ECPL process belongs to the category of mask projection stereolithography. However, the ECPL process differs from the other mask projection processes in that the thickness of each layer is not uniform. Instead, the thickness of each layer could be modified by changing the UV irradiation time for each curing UV profile. In addition, in ECPL system, there is no elevator component as that shown in Figure 1. Without any movements in z-direction, the error caused from the movement is reduced. Note that in Figure 1, the elevator can move the building platform, including the cured layers, to move in z-direction. The UV curable resin between the top surface of the resin bath and the top surface of the previous fabricated layer forms the “resin chamber” where the current layer could be fabricated, whereas all layers are fabricated within the same resin chamber, shown in Figure 10, in the ECPL system.

The ICM system, shown in Figure 10, utilizes the principle of Mach-Zehnder interferometer. Refer to Figure 10, the coherent laser beam originates from the laser source and travels downward to the resin chamber after getting reflected by the beam splitter. When the laser pass hits the resin chamber, it is assumed that part of the laser beam get reflected by the top side of the top substrate (a) of the resin chamber, whereas the other part of the laser beam is assumed to pass through the resin chamber until getting reflected by the bottom side of the bottom substrate (b). These two parts of the laser beams combines together and exhibits the fringe patterns, and the fringe patterns are received and recorded by the detector. When the ECPL process begins, the liquid monomers in the resin chamber get crosslinked to form the solid polymers, and the total refractive index changes during this crosslinking process. The change of refractive index will change the optical path between the top and bottom substrate of the resin chamber, and the detected interference

patterns will change as the crosslinking proceeds. By monitoring the change of the interference patterns using the ICM system, the thickness of the cured part could be calculated, and the dimensions of the cured part could be measured [9].

### **1.3 Motivation of Study**

As mentioned in Section 1.1.1, the mask projection stereolithography show the potential of fast throughput, rapid printing speed, high precision, and low cost. The ECPL process which is a mask projection micro-stereolithographic process is expected to have cost-effective applications in micro-lens fabrications. In order to achieve high accuracy for the final part, Jariwala et al. has developed ray tracing models and photopolymerization kinetic models [21], more accurate model with revised rate constant was then presented [22]. Ying et al. presented modified process planning method to further improve the dimensional accuracy and to reduce the dimensional error within 5% [23]. However, the error of the modified model increased when implementing the revised model into another system with similar equipment setting but different curing parameters. In addition to the process planning method, advanced process control methods were investigated. Jariwala et al. has proposed the Interferometric Curing Monitoring (ICM) system which is an in-situ measurement system to monitor the fabricating process of the ECPL system [9]. Jones et al. has proposed the revised ICM system which utilize a small beam of ICM laser instead of a laser beam with large diameter, in order to reduce the noise signal caused by internal reflections of the ICM laser beam within the two substrates of the resin chamber [24]. However, with only one small beam of laser, the ICM could not monitor the entire curing region. Zhao, X. et al. has proposed the ICM system using a large beam of laser to monitor the entire region and the ICM signal decoding algorithm for online measurement of the

height of a cured part with flat top [25] [26]. However, using a single ICM laser beam with large diameter to cover the entire curing region will contain the noise signal of ICM laser internal reflections proposed by Jones et al. [24]. In addition, no experimental results were done to measure the parts fabricated by the ECPL system with multiple heights within the same part. There exist little investigation in the lateral dimension measurements for ECPL fabricated features. The motivation of this research is to develop a real time ICM system which can measure the lateral dimensions and multiple heights of the parts fabricated by the ECPL system. The ICM system developed in this study also aims to reduce noise signal caused by the internal reflections proposed by Jones et al [24].

#### **1.4 Research Objective**

The primary objective of this research is:

*To develop the ICM monitoring system that is capable for measuring the lateral dimensions and the height distribution at different lateral locations of the transparent parts fabricated by the ECPL process.*

The fundamentals of ICM working principles and the signal decoding algorithm are available in literature review. The goal of this research is to provide an alternative ICM system design for accurately measuring the dimensions of the ECPL fabricated features in all three dimensions.

In order to reach the research objective, the ICM system would be modified to selectively interrogate the curing region and eliminate the amount of noise signal caused

by the internal reflections. The ICM system design should have the potential to further improve the lateral resolution.

## **1.5 Organization of This Thesis**

Chapter 1 is intended to provide a brief introduction to this thesis work. The background of mask projection lithography and ECPL, the principle of interferometry and ICM, and literature review is done. The motivation of the study and research objective is explained.

Chapter 2 presents previous work on the ECPL and ICM system designs in details. The research questions and hypothesis will be discussed.

Chapter 3 introduces the existing ICM system design, the ECPL fabrication procedure and ICM monitoring procedure. The fabricated features used in the experiments will be displayed.

Chapter 4 introduces the revised ICM monitoring system and the improved ICM monitoring method. The signal decoding procedure associated with the revised ICM system will be introduced.

Chapter 5 presents experimental results validating the proposed research hypothesis. The results will be discussed, the error will be analyzed, and the limitations of this study will be discussed.

Chapter 6 concludes the contributions, the evaluation of research hypothesis, and the future work of this study.

## **CHAPTER 2. LITERATURE REVIEW AND RESEARCH PROBLEM STATEMENT**

This chapter presents the literature review about the process planning method and the photopolymerization model. Literature review on the existing monitoring methods for additive manufacturing processes is presented. Previous studies on the monitoring and controlling methods for ECPL system is introduced. The signal decoding algorithm in this thesis study is introduced. Finally, the research question and hypothesis are presented.

### **2.1 Photopolymerization Model and Process Planning Method**

The ECPL fabrication process has been modeled as a photopolymerization process in the previous work. Photopolymerization is defined as a reaction that bonds both monomers and polymers together to form longer polymer chains or polymer networks using absorbed visible or ultraviolet light [28]. Boddapati has summarized the photopolymerization process as four mechanisms: initiation, propagation, termination, and inhibition [29] [30]. The initiation happens when the photoinitiator absorbs energy from radiation and decomposes into two radicals. During the propagation, these radicals can react with monomers and polymers to make the monomers and polymers active and be able to form longer polymer chains or polymer networks.

The termination happens as long as the propagation happens. The termination happens when two radicals come together to form a dead radical, and dead radicals cannot react with monomers or polymers during the propagation. In addition, termination happens when polymers react with another polymer or radical to form dead polymers, and dead

polymers cannot react with other monomers or polymers to form longer polymers or polymer networks. At the same time, inhibition happens when oxygen reacts with radicals and active polymers to form dead radicals and dead polymers. Previous study found that oxygen is considered to be an inhibitor during the ECPL process [23].

During the photopolymerization process, the degree of cure is used to determine the boundary between solidified cured polymer and liquid monomers. Flory has defined the degree of cure to be the fraction of bounded polymer over the original monomer [31]. Equation 1 defines the degree of cure:

$$\text{Degree of Cure} = \frac{[M_0] - [M]}{[M_0]} \quad (\text{Equation 1})$$

where  $M$  represents the monomer concentration remained after photopolymerization, and  $M_0$  stands for the initial monomer concentration. Jariwala et al. has proposed process planning method for ECPL system using the photopolymerization model mentioned above. Jariwala et al. utilized this model to simulate the polymerization reaction within the entire resin chamber of the ECPL system [32]. In his method, the desired feature is achieved by fabricating several layers of materials. The geometries of the desired feature were used as input, and a sequence of curing radiation profiles with corresponding curing times were calculated as output. He utilized COMSOL as simulation tool to simulate the photopolymerization process and get resultant fabricated features based on given curing radiation profiles. He also utilized MATLAB to optimize the curing profiles to improve the accuracy of the fabricated part [32]. In his method, the first layer is optimized for building the base and forming the edge of the desired feature. Then the set of previous radiation profiles and curing times and the desired feature geometries are used as input,

and the process will output the curing radiation profiles and curing times for the subsequent layers [32]. Jariwala et al. summarized that 20% degree of cure is a critical value to separate liquid resin and solid resin fabricated by ECPL process, i.e. in the resin chamber, places which the degree of cure is larger than 20% is considered to be solid cured part. Using this criterion, the estimated boundary of the fabricated part is defined by the contour representing the 20% degree of cure in the resin chamber [33]. Zhang et al. revised this model by modifying the chemical reaction rates as a function of irradiation area and adjusting the thickness of each fabricated layer, and the resultant accuracy of this revised process planning method is improved to be less than 5% between the estimated feature dimension and fabricated feature dimension. Figure 11 shows a block diagram of how this process planning method fits into the ECPL process to fabricate desired features.

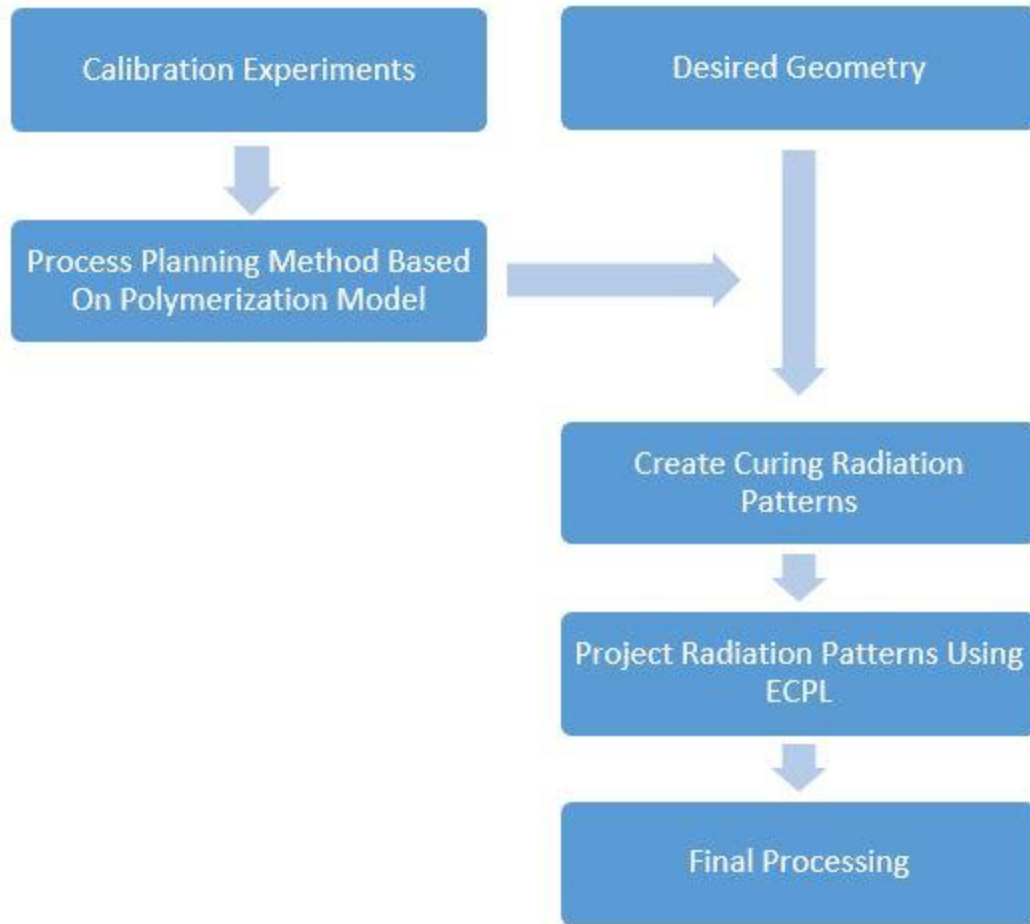


Figure 11. Block Diagram of Process Planning Method Utilized In ECPL System

## 2.2 Existing Monitoring Methods for Additive Manufacturing Processes

In order to understand the fabrication process, monitoring systems have been proposed and developed for various types of additive manufacturing processes. With in-situ signals gathered from the monitoring systems, the dynamic mechanisms happened during the fabrication process could be studied in details. These in-situ signals can also help validate and calibrate the existing empirical models. In addition, the in-situ signal gathered by the monitoring systems can be used as feedback information for close-loop

control methods, which have the potential to improve the accuracy and precision of the fabrication process.

Among literature review, several researchers have developed monitoring systems for additive manufacturing processes. For Selective Laser Melting process, the Spatially Resolved Acoustic Spectroscopy (SRAS) has been used for defects identification by Smith et al. [34]. The SRAS method utilizes one laser to generate the Surface Acoustic Wave (SAW) on the tested surface, and another laser is used for gathering the perturbation caused by the SAW. By analyzing the change of velocity of the SAW and dropout signals at the tested surface, the surface could be mapped by the SRAS method [35]. Figure 12 shows a schematic of the SRAS system setup.

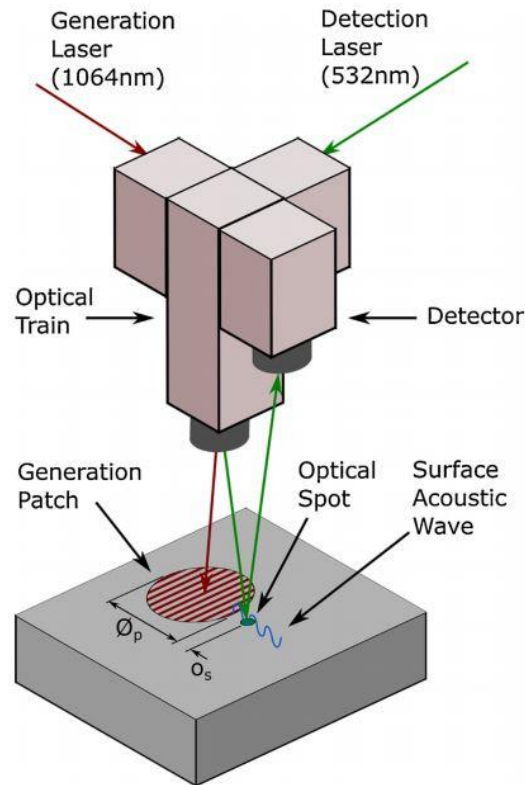


Figure 12. A Schematic of SRAS [34]

The advantage for the SRAS method is that the duration that SRAS method needs for each fabricated layer is acceptable. According to Hirsch et al., for a 10 x 10 mm layer with 25  $\mu\text{m}$  thickness, the SRAS method can scan within 128 second, and this setting is able to detect defects with minimum diameter of 50  $\mu\text{m}$  [34] [36]. The disadvantage of this method is that the SRAS method works on smooth surface, and it might not work for stereolithography which the cured part lays inside the resin chamber. Due to the fact that the solid cured part and the liquid monomers surrounding the solid part has different acoustic properties, propagation for the SAW within the resin chambers of stereolithographic processes are much more complexed to be modeled. Thus, the SRAS might not be suitable for stereolithographic process due to its difficulty.

For Selective Laser Sintering (SLS) processes, Optical Coherence Tomography (OCT) has been used to detect defects and identify the geometry of the fabricated feature. The OCT method utilized the principle of low-coherence interferometry. Figure 13 shows a schematic of OCT used by Lewis et al [37].

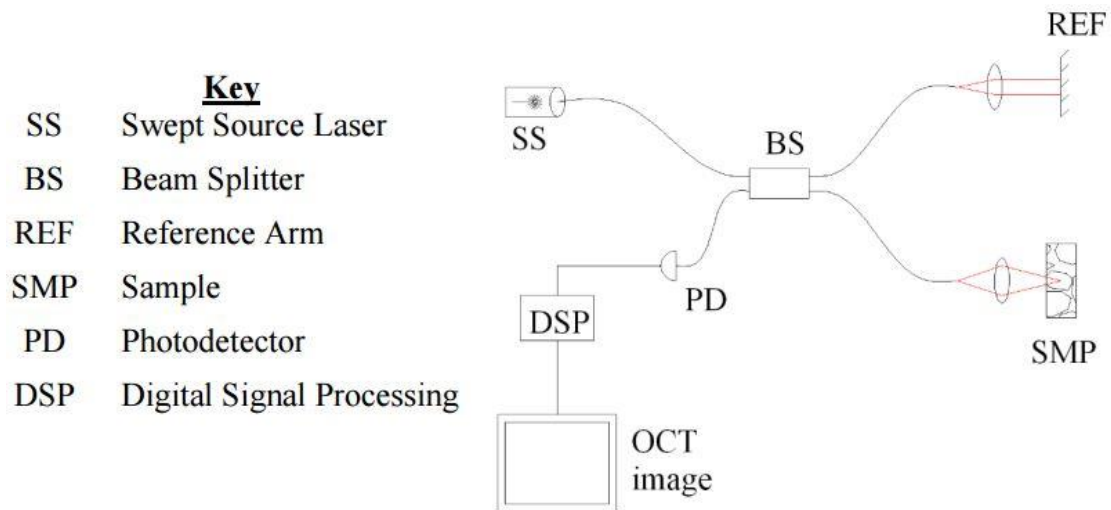


Figure 13. Schematic of OCT Used by Lewis et al. [37]

For the OCT method, one single beam is split into two sub-beams. One of the sub-beam is used as reference beam. The other sub-beam is used as sample beam which penetrates the measured sample, backscatters and recombines with the reference sub-beam. By analyzing the recombined beam profiles which exist interference patterns, the spatial information of the sample can be gathered [37]. Hirsch et al. has utilized a commercialized OCT system (Cirrus HD-OCT 5000) to detect defects of samples fabricated using the SLS process. The reported resolution was  $5\ \mu\text{m}$  with step size of  $15\ \mu\text{m}$ , and the OCT system took 49.284 second to scan through a layer of  $10\ \times\ 10\ \text{mm}$  [36]. The advantage of OCT system is that both the spatial resolution is good. In addition, OCT system also works for transparent parts, so the OCT system has the potential to be utilized as monitoring method for the ECPL system. However, the disadvantage of the OCT system is the cost. A used Cirrus HD-OCT 5000, the OCT system used in Hirsch's publication [36], cost \$58,950 [38], and a new Cirrus HD-OCT 5000 may cost even more. In addition, the OCT scanning

method is not fast enough to provide real-time information of the ECPL fabricating process which requires the OCT method to take several measurement trials.

Interferometers are widely used for stereolithographic processes. As discussed in Section 1.1.2, Lightman et al. has proposed the Mach-Zehnder interferometer system to monitor the change in refractive index of the photomonomers due to temperature change and due to photopolymerization of the monomers during the stereolithographic process. The system setting has been presented as Figure 5 and Figure 6 in Section 1.1.2. The reported theoretical resolution is  $6.2 \mu\text{m}$  with maximum sensing area of  $4 \times 4 \text{ mm}$  [16]. The advantage of this system includes the good resolution and its ability to record time-dependent change during the stereolithographic process. However, the HeNe laser used in this interferometer system [16] has larger wavelength with respect to the laser wavelength used in the ICM system in the thesis study. The larger wavelength used in the interferometer reduce the potential of high resolution, since larger wavelength requires larger pixel size for the detector in order to remain a large Fresnel number which is required for applying the principles of geometrical optics. In addition, the equipment setup for the interferometer system proposed by Lightman et al. is more complexed than that of the ICM system in this thesis study, and this increase both the cost of the equipment and the difficulty for aligning the optical paths. In addition, Mach-Zehnder interferometer system is used by Tran-Cong-Miyata et al. to measure the local deformation during stereolithographic process. The system setup has been presented as Figure 7 in Section 1.1.2. The reported measurement can detect small deformation up to approximately  $5 \text{ nm}$  [19]. The advantage of this interferometer system is also its ability to record real-time measurement with high resolution, and the disadvantage of this system is its complexity

and thus the difficulty to maintain the alignment of the optical path. Dudi et al. also presented a Michelson interferometer system to measure the change in refractive index of the cured sample with respect to various amount of curing radiation period and various exposure radiation intensities. The system setup is presented as Figure 8 in Section 1.1.2 [27]. This Michelson interferometer system precisely measured the change of refractive index, and the in-situ measurements reveal the effect of radiation intensity to the speed of refractive index changes. This system also has the advantage of low-cost. However, the samples needed for this system require thickness of approximately 200  $\mu\text{m}$  [27]. This requirement is not qualified to measure fine features in micro-scale fabricated by the ECPL system.

Another measuring system utilized for measuring features fabricated by stereolithographic processes is Scanning Acoustic Microscopy (SAM). Simonin et al. has presented an SAM system to measure the crosslinking density changes of photopolymers during the stereolithographic processes and to plot the height distribution of the surface of the features fabricated by stereolithographic processes. Figure 14 shows a schematic of SAM proposed by Simonin et al. [49]

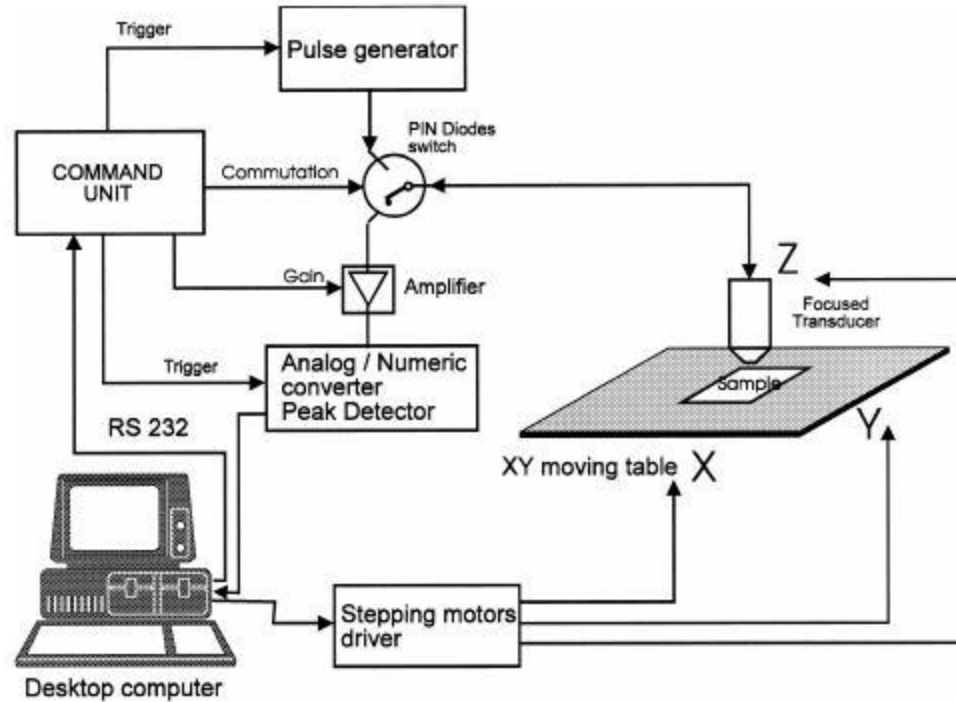


Figure 14. Schematic of SAM System [49]

As shown in Figure 14, the desktop controls the focused transducer to generate a low frequency spherical acoustic wave (25 MHz) which propagates through the measured sample. Part of the acoustic wave reflects back, and a probe positioned above the sample measures the acoustic pressure of the reflected wave. The SAM system has a point-by-point scanning procedure. The positions of the focused transducer and the measuring probe are fixed. The XY moving table, controlled by the computer, moves the sample so that different lateral locations (in the XY plane) of the fabricated part could be measured by the SAM system. For each measuring location, the acoustic pressure of the reflected wave is analyzed to estimate the crosslinking density and the fabricated sample height at that location. By mapping all the measured heights at different locations of the fabricated part, the surface profile of the fabricated part could be gathered [49]. The SAM system presented

by Simonin et al. have a theoretical lateral resolution of  $12.5\ \mu\text{m}$  [50], and the system could have a height resolution of  $3\ \mu\text{m}$  [49]. However, there are two disadvantages of this process. Firstly, the SAM utilizes a point-by-point scanning procedure which could measure only one position for each step. This limits the efficiency of the measuring process. The long measuring period for each complete set of measurements (i.e. measuring all the locations of the cured feature) makes the SAM method unable to conduct real-time in-situ measurement during the stereolithographic fabrication processes. Secondly, as shown in Figure 14, the sample itself needs to be moved in order to take measurements at different positions of the sample. However, movements of the resin bath (refer to Figure 1) could result in local motions of liquid UV curable resin, and these local motions will add significant building errors to the fabricated parts. Even if the SAM system is designed to move the measuring probe instead of moving the entire sample, since the high sampling frequency requires measuring multiple lateral positions within short period for each measuring trial, there will be continuous sequences of impulsive movements for the measuring probe, and these sequences of impulsive movements might makes the measuring probe to vibrate. These vibrations will add noise when the probe measures the reflected wave intensities, and the noise will deteriorate the accuracy of the SAM system measurements. Thus, although the resolutions of the SAM method, proposed by Simonin et al. [49] [50], has sufficient resolution both in height and lateral dimensions, due to the low measuring efficiency and the potential addition of building errors and measuring errors, the SAM could not be used as a real-time in-situ monitoring system for the stereolithographic processes, including the ECPL process.

### 2.3 Existing Monitoring and Controlling Methods for ECPL System

The purpose for the monitoring system is to provide real-time feedback for the ECPL fabrication process which the change of refractive index of the photopolymers in the resin chamber with respect to time steps could be gathered. Since the change of refractive index is associated with the photopolymerization process, the ICM system can be served to monitor the speed of the fabrication, and the dimensions of the cured part could be gathered based on the recorded ICM signals. Jariwala et al. in 2011 presented the ICM system which has the potential to provide feedback control to the ECPL process [9]. The schematic of this ICM system has been presented as Figure 10 in Section 1.2. This monitoring system utilized the principle of Mach-Zehnder interferometer. Compared with the Mach-Zehnder interferometer systems described in Section 2.2, this ICM system simplified the equipment setting that the top glass substrate served as mirror (for example,  $M_1$  in Figure 3) which were used to create paths for the reference laser beam in the Mach-Zehnder interferometer systems. The relation between change in the optical path and change of refractive index of the photopolymers in the resin chamber has been modeled. The change in the optical path has been related to phase change of the ICM laser reflected from the bottom side of the bottom substrate of the resin chamber. The relationship between the phase shift of the ICM laser signal and the thickness of the part fabricated by the ECPL process has been summarized. The term “interferogram” was defined as the plot of intensity detected by the ICM detector with respect to time. Figure 15 shows a typical interferogram gathered by Jariwala et al. The initial inhibition and dark curing period during the ECPL fabrication process has been identified from this ICM-captured interferogram [9]. However, the ICM

system proposed in this system can only measure the thickness of the cured part. No lateral dimension detection could be done by this system.

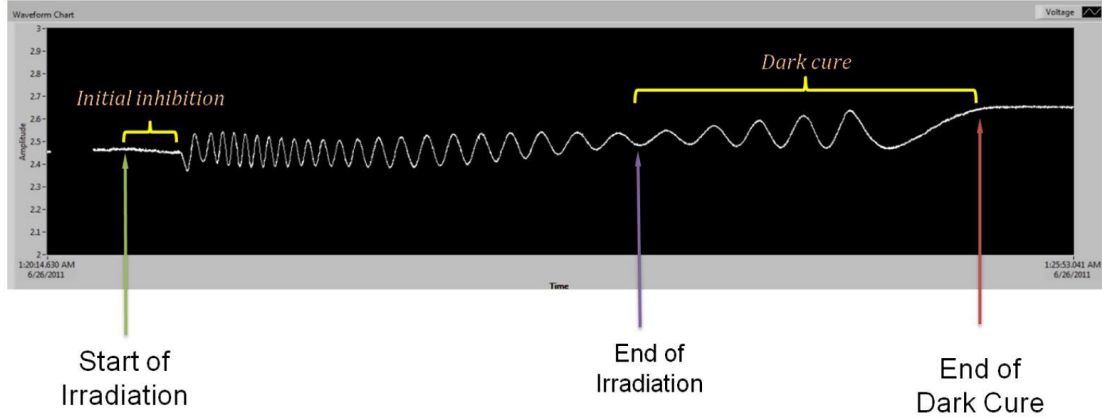


Figure 15. ICM-Captured Interferogram by Jariwala et al. [9]

In 2013, Jones et al. has simplified the relation between the thickness of the cured part and the total phase shift detected by the ICM interferogram as Equation 2:

$$Phase\ Shift = \frac{2 \cdot \Delta n \cdot t}{\lambda} \quad (Equation\ 2)$$

where  $\Delta n$  is the change in refractive index of resin in the resin chamber,  $t$  is the thickness of the fabricated feature, and  $\lambda$  is the wavelength of the ICM laser beam. An experimentally determined relationship between total phase shift of the ICM interferogram and thickness of the fabricated feature is presented as Equation 3:

$$Z = 30.144 \cdot \ln(\phi) - 159.83 \quad (Equation\ 3)$$

where  $Z$  is the thickness of the cured part thickness in  $\mu\text{m}$  and  $\phi$  is the total phase shift from the ICM interferogram in radian [39]. An experimentally determined relationship between the curing radiation exposure time and fabricated part thickness is presented as Equation 4:

$$Z = 36.85 * \ln(t) + 22.07 \quad \text{(Equation 4)}$$

where  $Z$  is the thickness of the cured part thickness in  $\mu\text{m}$  and  $t$  is the curing radiation exposure time in second [39]. A stopwatch close-loop control system design for the ECPL process combined with ICM system was also presented by Jones et al. The flowchart of this close-loop control system is presented as Figure 16 [39].

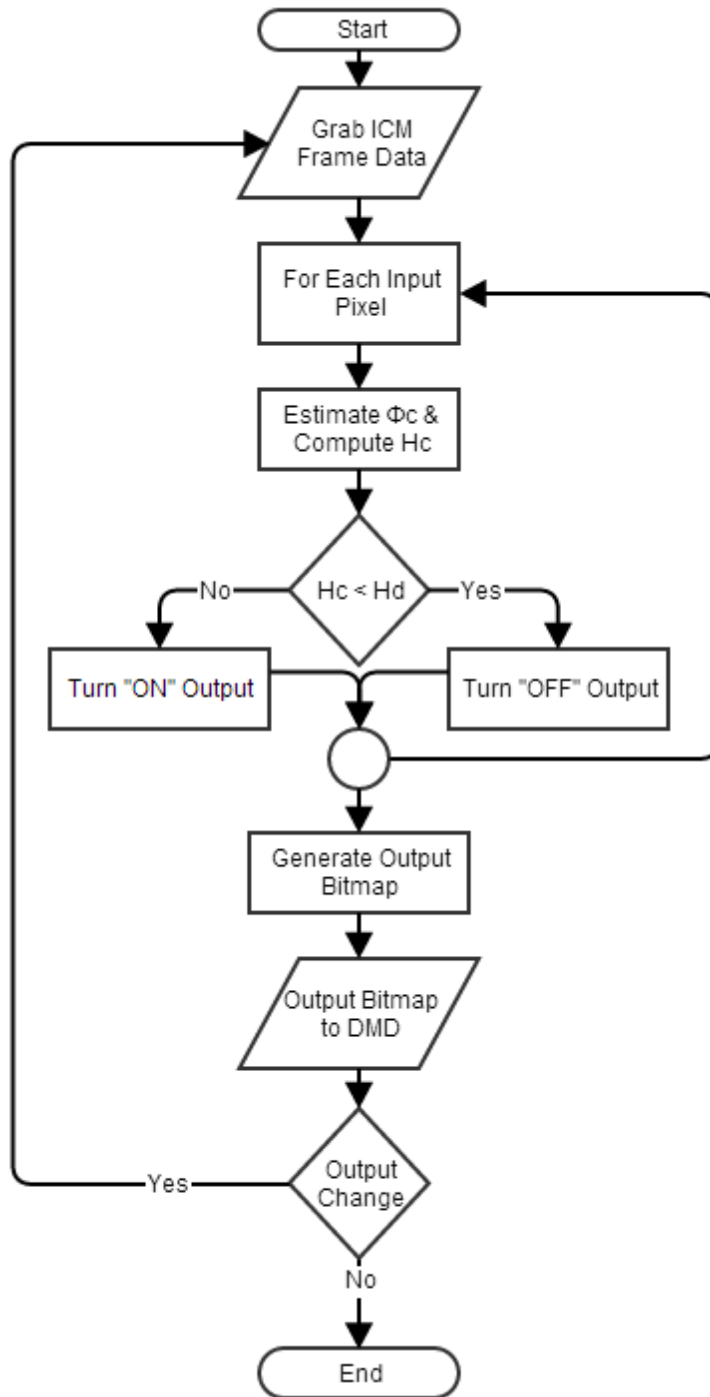


Figure 16. Flow Chart of the Close-loop Control Using the ICM System [39]

Figure 16 shows the flow diagram of the close-loop control system [39]. In this figure,  $\Phi_c$  stands for the total phase angle change counted by the ICM-gathered interferogram,  $H_c$  stands for the estimated cured part height, and  $H_d$  stands for the height of the desired geometry. By comparing this 3-D profile with the 3-D profile of the desired part, the close-loop control is developed to control the curing times for their corresponding curing UV profiles. Figure 17 shows an overview of ECPL system and ICM system, showing how the close-loop control could be achieved with feedback signals gathered by the ICM system.

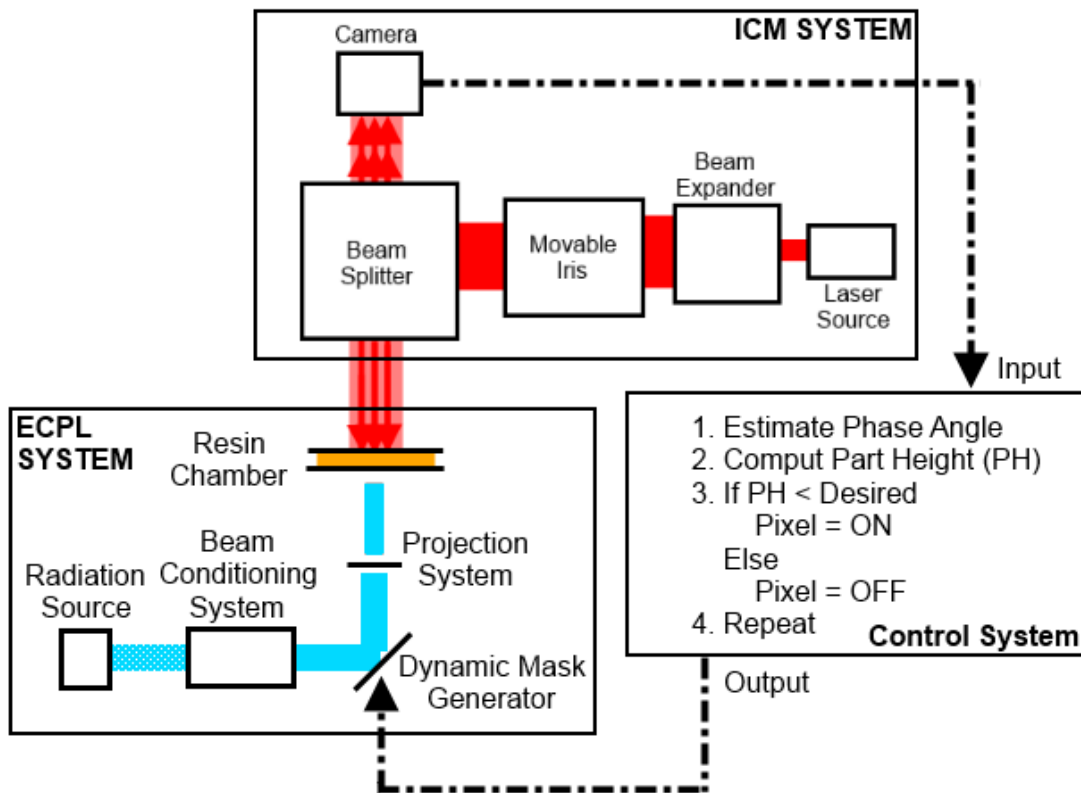


Figure 17. Overview of the ICM System and the ECPL System [39]

Besides simplifying the interferogram relationships and proposing the close-loop control, Jones et al. presented the improved ICM system which the ICM laser beam profile

is large enough to cover the whole curing region and measure the cured part thickness [24]. Jones et al. also presented the disadvantage of this ICM system that when using a laser beam with cross-section profile, the phase change could also be found even outside the curing region. Figure 18 shows an experiment done by Jones et al. which showed that the observable phase change outside the curing region was falsely observed by the original ICM system using a single laser beam with large cross-section profile.

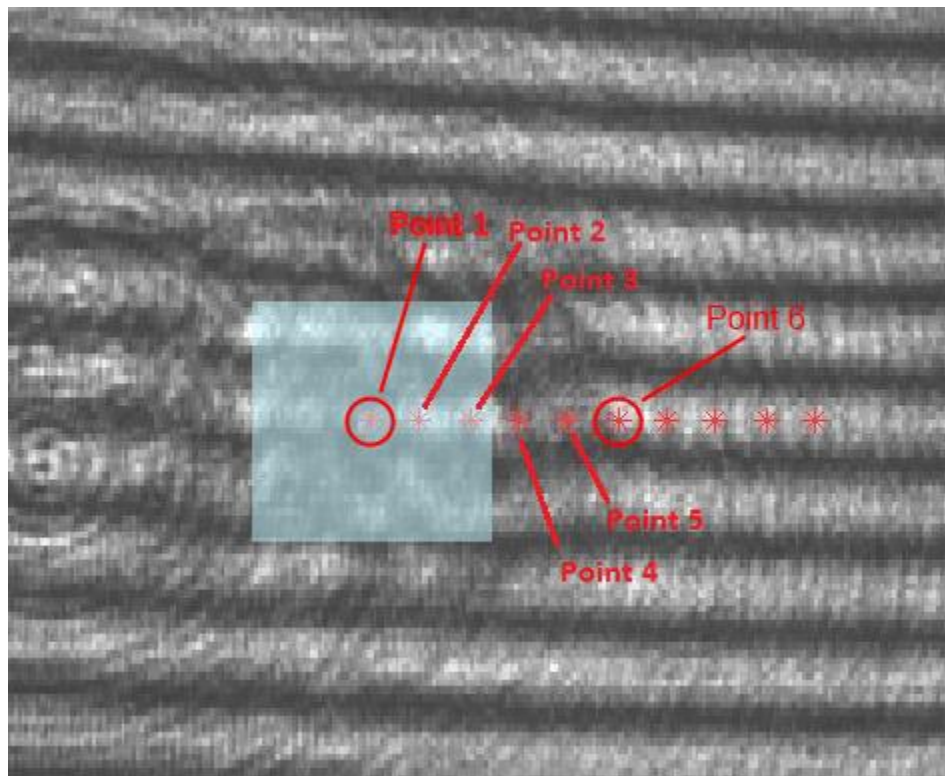


Figure 18. Experiment Done by Jones et al. to Show the Limitation of ICM with Large Laser Beam [24]

In this experiment, the ECPL system was set to shine a UV radiation profile to fabricate a rectangular part. This UV radiation pattern was defined as a square region of 150 x 150 pixel, defined by the DMD. The original ICM system, proposed by Jones et al.

[24], were used to monitor this fabricating process by using a single laser beam with large cross-section profile that could cover the entire curing region. Figure 18 shows a frame of the video gathered by the ICM system when monitoring the fabricating process. The blue square indicates the curing region. The six red star signs in Figure 18 indicates the six points that were analyzed for this experiment: point 1 was at the center of the curing region; point 2 and point 3 were within the curing region; point 4, point 5 and point 6 were outside of the curing region. The distance between each pair of the neighboring points was set to be  $300\ \mu\text{m}$ . During the fabricating process, the interferograms at these six points were recorded. Figure 19 shows the results of this experiment which are the interferograms recorded at these six points.

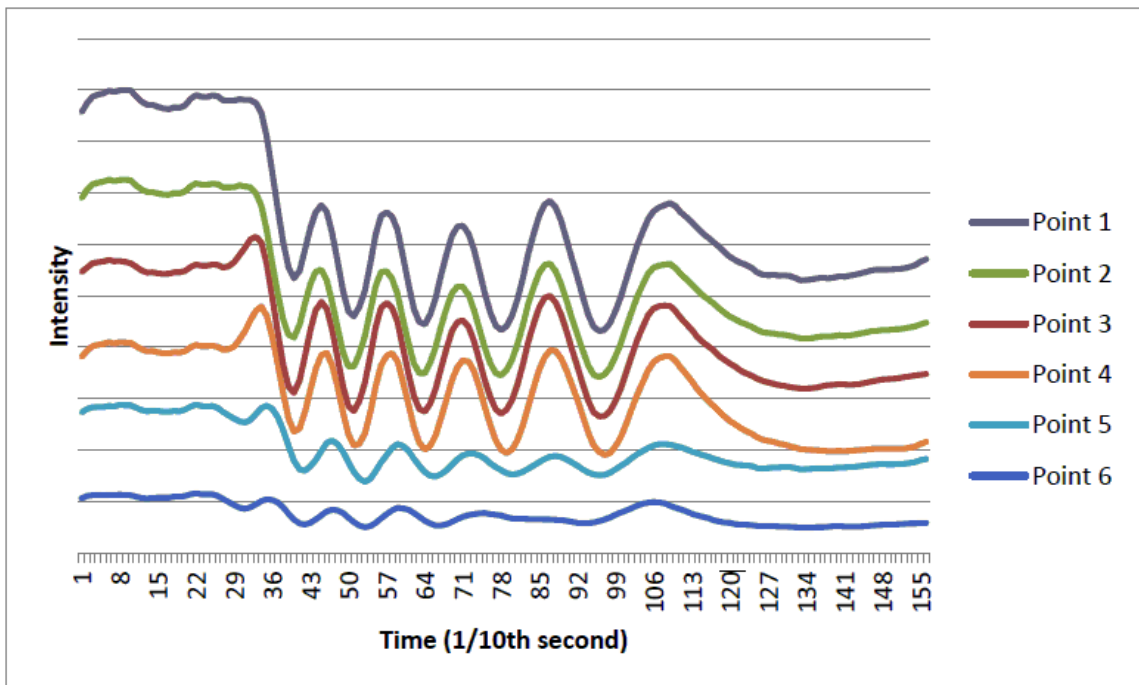


Figure 19. Experiment Results Done by Jones et al. to Show the Limitation of ICM with Large Laser Beam [24]

As shown in Figure 19, the interferograms at point 1, point 2, point 3, point 4, point 5 and point 6 exhibited obvious phase changes during the fabricating process, though the interferograms at point 5 and point 6 exhibited phase change with small amplitude. The phase change in the interferograms indicated that the photopolymers were cured at these positions. However, in reality point 4 to point 6 were outside the UV radiation region. Thus, it could be concluded that although point 4 to point 6 were not cured by the UV radiation, the original ICM system using a single beam with large cross-section profile still indicated that position at point 4 was cured by the UV radiation from the ECPL system, and positions at point 5 and point 6 could be possibly cured by the UV radiation from the ECPL system. Since the edge of the curing region happened to be between point 3 and point 4 while the ICM-indicated edge of the curing region was between point 4 and point 5, the error for the edge detection could be larger than 300  $\mu\text{m}$ , and the resolution for the lateral dimension measurement could be below 600  $\mu\text{m}$  (because the lateral dimension measurements need to detect 2 edges).

Jones et al. proposed that this low lateral resolution is due to the noise signals caused by the internal reflection of the ICM laser beams within the resin chamber. Figure 20 presents a schematic of the noise signal generation due to the internal reflections proposed by Jones et al. [24].

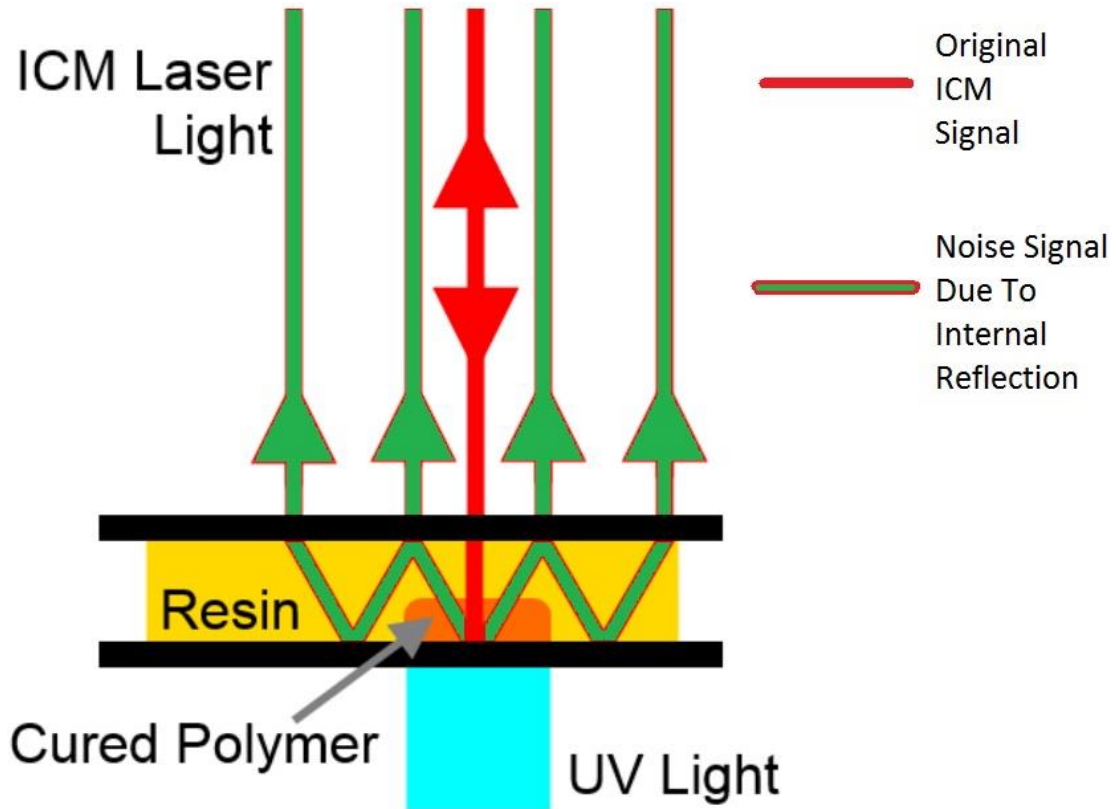


Figure 20. A Schematic of Noise Signal Generation Due To Internal Reflections

Proposed by Jones et al. [24]

As shown in Figure 20, the red lines represents the original ICM laser beam from the laser source, and the green lines represents the noise signals due to the internal reflections from the original ICM laser beam. Jones et al. presented that when an ICM laser beam passes through the resin chamber, in addition to the major beam reflection which travels vertically upwards and forms the original ICM signals, part of the laser reflects multiple times within the resin chamber and forms the noise signals. Since these noise signals come from the reflected laser beam that has passed through the fabricated feature and has affected by change in refractive index with respect to time, these noise signals, which travels upward at positions out of the curing region, also exist phase change with respect to time.

Influenced by these noise signals, the ICM captured interferograms at positions outside the curing region will also exhibit phase changes. Jones et al. presented the solution to reduce these noise signals as to use a laser beam with small cross-section profile as the ICM laser beam [24]. However, since the ICM system used in the paper utilized a lever-actuated iris which could only open one beam as the ICM laser beam, only one laser beam with small cross-section could not cover the entire curing region [24]. This motivates the objective of this thesis study: *to develop an ICM system which can monitor the entire curing region with reduced noise signal from the internal reflections.*

In 2015, Zhao, X. et al. presented investigation in ICM laser signals based on a detailed ICM laser reflection and interference model at the resin chamber [40]. This reflection model is shown as Figure 21.

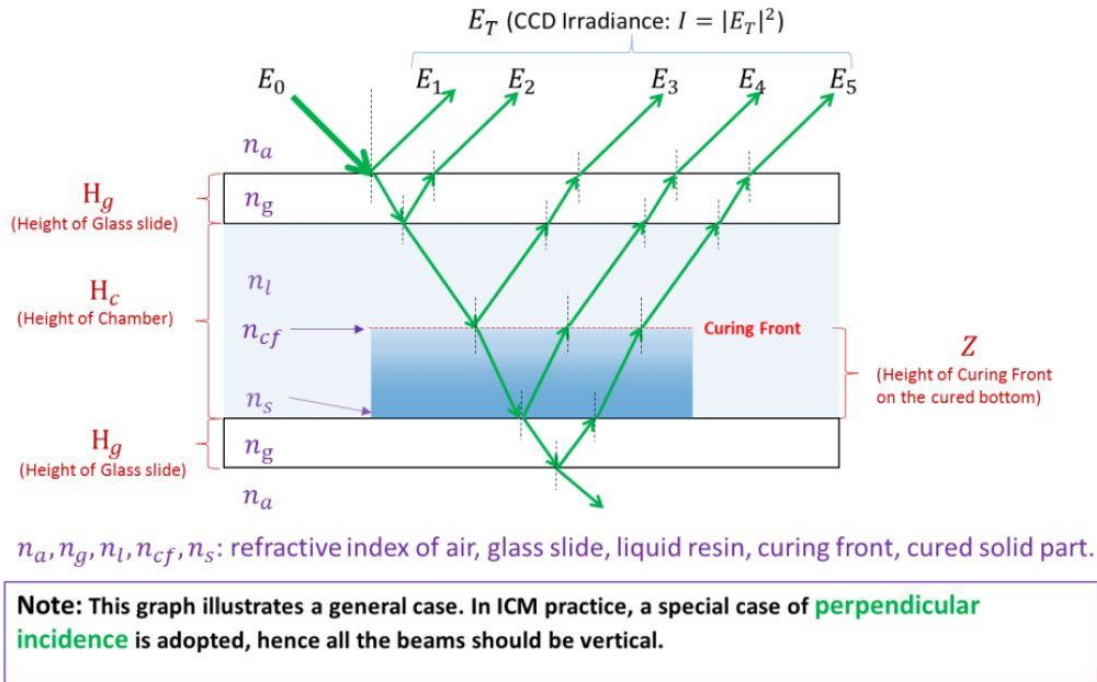


Figure 21. Detailed ICM Laser Reflection Model by Zhao, X. et al. [40]

The wave of the ICM signal from each of the reflection in Figure 21 is presented as Equation 5, and the wave of the ICM signal from the combined reflections is presented as Equation 6:

$$E_n = A_n e^{i\phi_n}, n = 1, 2, \dots, 5 \quad (\text{Equation 5})$$

$$E_T = \sum_{n=1}^5 E_n = \sum_{n=1}^5 A_n e^{i\phi_n} \quad (\text{Equation 6})$$

where  $E_n$  stands for the wave of the reflected ICM laser beams,  $E_T$  stands for the wave from combined reflections,  $A_n$  is the real positive amplitude for each reflection, and  $\phi_n$  is the phase angle of each reflected ICM signal. The intensity of the ICM signal of the combined reflections is presented as Equation 7:

$$I = |E_T|^2 = \left| \sum_{n=1}^5 A_n e^{i\phi_n} \right|^2 = \sum_{n=1}^5 |A_n|^2 + \sum_{j=1}^5 \sum_{\substack{k=1 \\ k \neq j}}^5 A_j A_k \cos(\delta_{jk}) \quad (\text{Equation 7})$$

where  $\delta_{jk} = \phi_j - \phi_k$  is the relative phase difference between the component of each reflected wave [40]. The phase components between each pair of interfered beams were presented as Table 1:

Table 1. Phase Components of the Multi-beam Interference Optics Model in ICM [40]

No.	Phase Difference	Source Beams	Role
1	$\delta_{21} = \frac{4\pi}{\lambda} n_g H_g$	$E_1, E_2$	Constant DC term
2	$\delta_{31} = -\frac{4\pi}{\lambda} n_l Z + \frac{4\pi}{\lambda} n_l H_c + \delta_{21}$	$E_1, E_3$	Oscillating AC term
3	$\delta_{41} = \frac{4\pi}{\lambda} (n_m - n_l) Z + \frac{4\pi}{\lambda} n_l H_c + \delta_{21}$	$E_1, E_4$	Oscillating AC term
4	$\delta_{51} = \frac{4\pi}{\lambda} (n_m - n_l) Z + \frac{4\pi}{\lambda} n_l H_c + 2\delta_{21}$	$E_1, E_5$	Oscillating AC term
5	$\delta_{32} = -\frac{4\pi}{\lambda} n_l Z + \frac{4\pi}{\lambda} n_l H_c$	$E_2, E_3$	Oscillating AC term
6	$\delta_{42} = \frac{4\pi}{\lambda} (n_m - n_l) Z + \frac{4\pi}{\lambda} n_l H_c$	$E_2, E_4$	Oscillating AC term
7	$\delta_{52} = \frac{4\pi}{\lambda} (n_m - n_l) Z + \frac{4\pi}{\lambda} n_l H_c + \delta_{21}$	$E_2, E_5$	Oscillating AC term
8	$\delta_{43} = \frac{4\pi}{\lambda} n_m Z$	$E_3, E_4$	Oscillating AC term
9	$\delta_{53} = \frac{4\pi}{\lambda} n_m Z + \delta_{21}$	$E_3, E_5$	Oscillating AC term
10	$\delta_{54} = \frac{4\pi}{\lambda} n_g H_g = \delta_{21}$	$E_4, E_5$	Constant DC term

In Table 1,  $Z$  stands for the thickness of the fabricated feature;  $\lambda$  is the wavelength of the ICM laser beam which is 532 nm;  $H_g$  and  $H_c$  stands for the thickness of the glass substrate and the resin chamber;  $n_a$ ,  $n_g$ ,  $n_l$ ,  $n_{cf}$ , and  $n_s$  stands for the refractive index of air, glass substrate, liquid resin, curing front, and cured solid feature; *DC* stands for direct current; *AC* stands for alternative current. It was summarized by Zhao, X. et al. that the phase change of the ICM-recorded interferogram is not relative to the interference associated with reflected ICM laser  $E_1$  and  $E_5$  [40]. Zhao, X. et al. also presented the relationship between the ICM signal intensity captured by the ICM camera and the instantaneous thickness of the fabricated feature, which is shown as Equation 8 and Equation 9:

$$I_M = I_0 + I_1 \cos(\delta + \varphi) = I_0 + I_1 \cos\left(\frac{4\pi(n_m - n_l)}{\lambda} * Z + \varphi\right) \quad (\text{Equation 8})$$

$$\omega = 2\pi f = \frac{d(\delta + \varphi)}{dt} = \frac{d\delta}{dt} = \frac{4\pi(n_m - n_l)}{\lambda} * \frac{dZ}{dt} \quad (\text{Equation 9})$$

where  $Z$  is the cured part thickness,  $I_M$  is the measured ICM signal intensity by the ICM camera;  $I_0$  is the overall average intensity;  $I_1$  is the superposed intensity of all the interference beams with the same instantaneous frequency  $f$ ,  $\delta$  is the time-varying phase component in the intensity model,  $\varphi$  is the static superposed phase offset of all the interference beams with the same frequency;  $f$ ,  $\omega$  are the instantaneous frequency and instantaneous angular frequency, respectively;  $\lambda$  is the laser wavelength 532 nm,  $n_m$  and  $n_l$  are mean cured and liquid part refractive index and can be calibrated through experiments [40].

The differential form of the cured part thickness from Equation 9 is rewritten as Equation 10:

$$\frac{dZ}{dt} = \frac{\omega\lambda}{4\pi(n_m - n_l)} = \frac{f}{2\pi(n_m - n_l)} \quad (\text{Equation 10})$$

Thus, the cured part thickness,  $Z$ , could be calculated by using numerical integration approach based on Euler's Method. Equation 11 presents the equation of cured part thickness summarized by Zhao, X. et al.:

$$Z = \sum_i \frac{\lambda T_i}{4\pi(n_m - n_l)} * \omega_i = \sum_i \frac{\lambda T_i}{2\pi(n_m - n_l)} * f_i \quad (\text{Equation 11})$$

where  $T_i$  is the time step of integration,  $f_i$  (or  $\omega_i$ ) is the instantaneous (angular) frequency in the  $i_{th}$  run of parameter estimation. The refractive index term ( $n_m - n_l$ ) could be calibrated by experiments [40].

As a summarization, the ICM signal decoding method presented by Zhao, X. et al. [40] is as follows:

The intensity of the ICM-captured interferogram,  $I_M(t)$  where  $t$  stands for the time steps during the ECPL fabrication process, is cut into  $j$  segments:  $I_M(t_i \sim t_{i+1})$  for  $i = 1, 2, \dots, j-1$ . Within each segment, a Fourier curve fitting has been done to parametrize  $I_M(t_i \sim t_{i+1})$  as a function of Equation 12:

$$I_M(t_i \sim t_{i+1}) = A \cos(\omega_i t + \varphi) + B, i = 1, 2, \dots, j - 1 \quad (\text{Equation 12})$$

where  $\omega_i$  stands for the instantaneous frequency within the  $i_{th}$  ICM interferogram segment. The time step is defined as  $T_i = t_{i+1} - t_i$ . For each segment ( $t_i \sim t_{i+1}$ ), the  $\omega_i$  is determined using Fourier curve fitting method to fit  $I_M(t_i \sim t_{i+1})$ . Plugging all the fitted pairs of  $\omega_i$  and  $T_i$  back to Equation 11, the cured part thickness could be calculated.

The ICM signal decoding method with data mining algorithm has been presented by Zhao, X. et al., and validation experiments have been done to proof the proposed ICM measuring system and the decoding algorithm [25] [41]. The proposed resolution in ICM thickness measurement was 5.59  $\mu\text{m}$ , and the repeatability of the ICM thickness measurement was reported to be less than 1.82  $\mu\text{m}$ . The theoretical ICM measurement resolution in lateral dimensions was proposed to be 8.8  $\mu\text{m}$  [41]. The ICM measurement

system and decoding algorithm developed by Zhao, X. et al. [25] [40] [41] has advantage in the simplicity of system setup and high resolution in cured part thickness measurement. The proposed ICM decoding algorithm is efficient to perform real-time in-situ part thickness measurement during the ECPL fabrication process. However, the noise signals due to internal reflections, proposed by Jones et al. [24], was not solved in this ICM system since it still uses an ICM laser beam with large cross-section profile. No comprehensive validation experiment for ICM's ability in measuring lateral dimensions of the cured part has been reported by ICM system developed by Zhao, X. et al. No validation experiment has been reported for ICM's ability in measuring cured part dimensions with multiple thicknesses at different lateral locations, either.

Compared with the proposed ICM system by Zhao, X. et al. [40], the revised ICM system in this study uses multiple laser beams, each with small cross-section profile, to measure the cured features fabricated by the ECPL process. Since these multiple laser beams are isolated with each other, this reduces the noise signal due to the internal reflections and guarantees the accuracy of the ICM system in measuring the lateral dimensions of the cured parts. On the other hand, the revised ICM system in this thesis study has disadvantage that the system setup is more complexed due to the replacement of lever-actuated iris by the electronic iris system. In addition, since the time-varying scanning method in this thesis study measures different locations at different time, the ICM recording frequency at each of the measured location is reduced, and the resolution of height measurements is lower compared with the ICM system proposed by Zhao, et al. when using the same camera setting. Note that the ICM laser interference model and the

signal decoding algorithm proposed by Zhao, X. et al. [40] has been used in this thesis study.

## **2.4 Research Questions and Hypothesis**

As mentioned in Section 2.3 and illustrated with Figure 18 and Figure 19, the original ICM system, which utilized a single laser beam with large cross-section profile, had the resolution in lateral dimension measurements to be lower than 600  $\mu\text{m}$  [24]. In order to accomplish the research objective, the ICM noise signals that affects the accuracy of lateral dimension measurements should be reduced. The ICM system should be able to measure the whole curing region. Therefore, the research question is formed below.

**Research Question: How to modify the ICM system to accurately measure the dimensions of the cured part fabricated by the ECPL system?**

**Hypothesis:** The dimension measurements of the cured part can be done by using isolated laser beams with small cross-section profiles to cover the interested area. By measuring neighboring positions that are too close to each other at different time steps, the resolution in lateral dimension could be improved.

**Explanation:** The existing literatures shows ICM's ability in determining the height of a flat cured part. The ICM utilizes laser beams to radiate the interested positions and gather the interferograms at these locations to estimate the cured part height at these positions. However, the literature [24] shows that the lateral dimension detection was largely influenced by noise signals caused by internal reflections. Isolated laser beams are introduced into the ICM system in order to reduce these noise signals. By using laser beams

which are isolated with each other and which are with small cross-section profiles, the interference between two neighboring laser beams will be avoided. By only measuring the centers of the isolated laser beams, the effects of noise signals, caused by internal reflections of the ICM laser beams, onto the lateral dimension measurements, will be reduced. The reduced effects of the noise signals in the ICM system will improve the accuracy of the measurement. To improve the lateral resolution of the ICM system, more positions should be monitored. However, with more positions being monitored within a certain area, the neighboring monitored positions could be too close to each other that interference between reflected laser beams at these neighboring locations adds noise signals and reduces the accuracy of the ICM measurements. In order to gather information at both of these neighboring positions, the information at these positions must be measured at a different time steps. The time-varying scanning method developed in this thesis sequentially measures these neighboring positions, which are too close to each other, at different time steps. In addition, the time-varying scanning method sequentially measures these neighboring positions with high sampling frequency. The Spatial Light Modulator (SLM) can move the locations of the small laser beams with respect to time. Thus, it enables the ICM to measure the locations (where the locations will cause interference with the other locations) at different time steps. This can increase the ICM resolution in 2D lateral dimensions by introducing time variance in addition to the 2D spatial dimensions.

## **2.5 Chapter Summary**

This chapter introduced background information related to the ECPL and ICM system. The photopolymerization model has been presented in order to explain the mechanism of refractive change during the ECPL process. The existing monitoring

methods for various additive manufacturing processes was introduced. The merits and drawbacks of each monitoring method has been discussed. Previous work on the ICM system development has been introduced. The ICM signal decoding algorithm used in this thesis study has been introduced. Research question and hypothesis have been claimed in this chapter with explanations.

# CHAPTER 3. EXISTING ECPL AND ICM SYSTEM DESIGN AND EXPERIMENT PROCEDURE

In this chapter, the new ECPL system will be introduced. In addition, the original ICM system will be introduced for comparison with the improved ICM system. The procedure for ECPL system fabrication process will be introduced. The fabricated features will be displayed.

## 3.1 Existing System Design

A schematic of the original ICM system is shown in Figure 22. A photo of the original ECPL and ICM system is shown as Figure 23 [41]. The ICM system includes part 1 to part 5 in green boxes in Figure 23, and the ECPL system includes part 1 to part 5 in blue boxes in Figure 23.

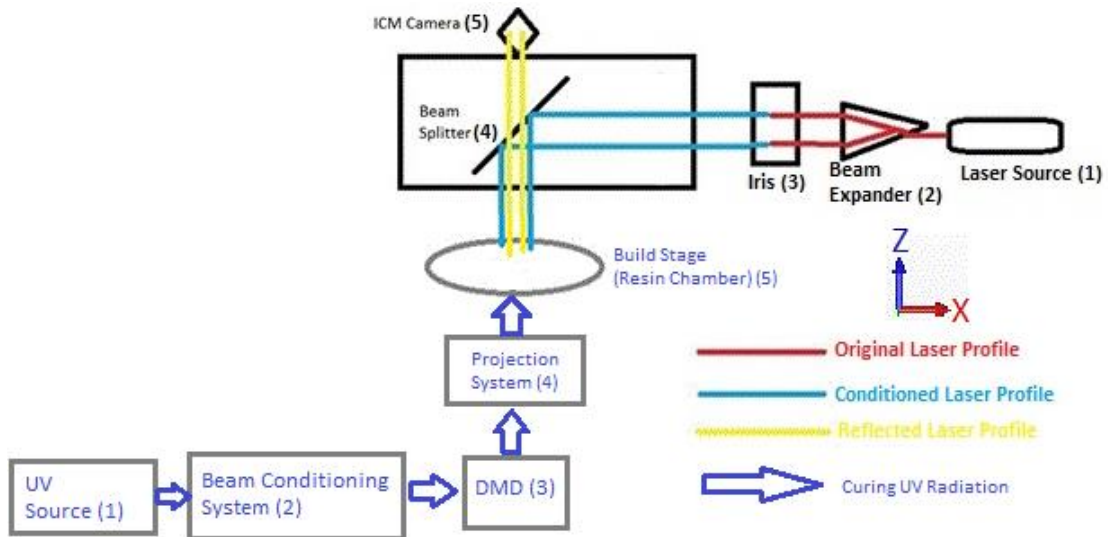


Figure 22. Schematic of the Original ICM System (Y axis is perpendicular into the paper)

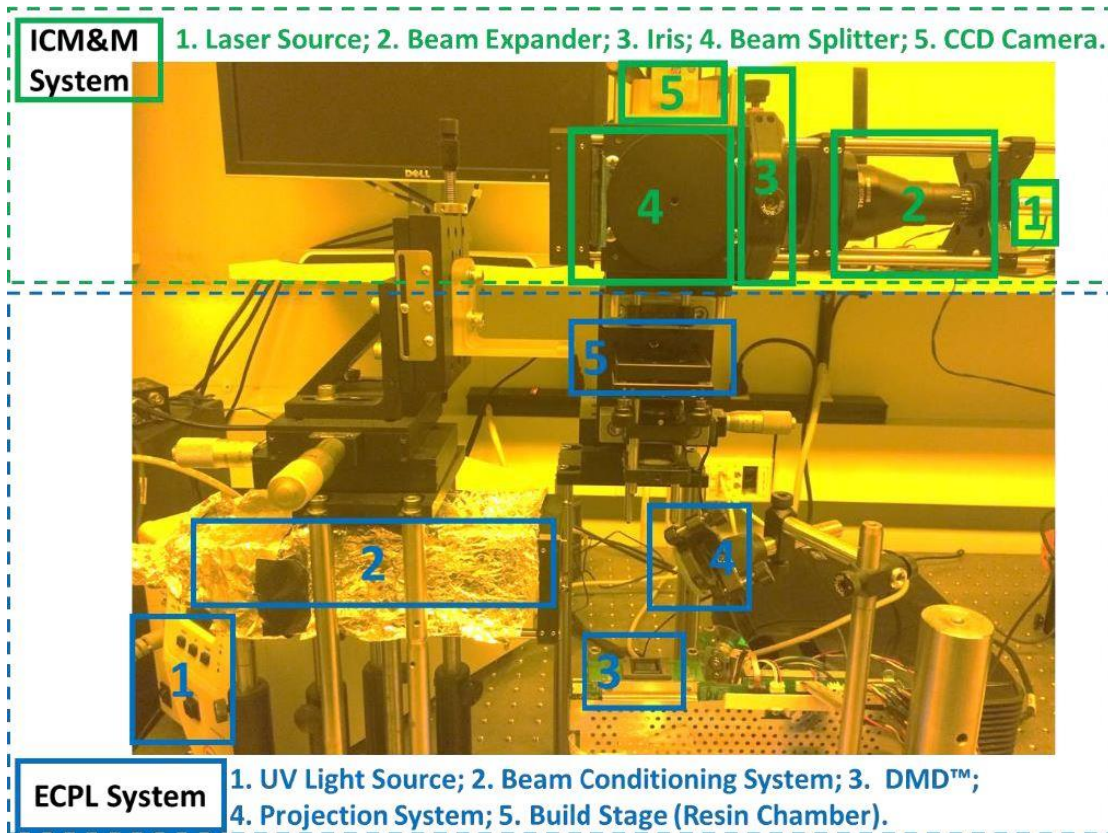


Figure 23. The Original ECPL and ICM System [42]

For the original ECPL system, the curing light from the UV radiation source (part 1 in blue in Figure 22) passes through the beam conditioning system (part 2 in blue in Figure 22) and reach at the dynamic mask generator (DMD) (part 3 in blue in Figure 22). The DMD forms the dynamic masks which control the cross-section profile of the UV radiation and forms the curing UV radiation profiles for the stereolithographic process. The projection system guides the light onto the resin chamber, and the light passes through the bottom transparent substrate of the resin chamber into the photopolymer resin to begin the curing process. The dynamic mask and exposure time determine the 3D dimensions of the part. The following paragraph shows detailed descriptions of the components of the ECPL system.

For the original ICM system, a coherent laser is generated by the laser source (part 1 in Figure 22). The laser is directed through a beam expander (part 2 in Figure 22), a Lever-Actuated Iris (SM1D12 from Thorlabs, Inc.) (part 3 in Figure 22), and beam splitter (part 4 in Figure 22), at the resin chamber (part 6 in Figure 22). Light reflecting off of the top and bottom surface of the resin chamber's two transparent bounding surfaces reflect through the beam splitter and into the ICM camera (part 5 in green box in Figure 22). Due to the phase difference between the light coming from the top surface and the light coming from the bottom surface an interference pattern is observed by the camera. The iris in the original ICM system controls the diameter of the laser profile. However, only one beam of light can be formed by the original ICM system. To generate multiple beams of ICM lasers, an electronic iris system has been introduced to make the new ICM system. The improved ICM system will be introduced in Section 4.1.

### **3.2 Experimental Procedure and Resultant Samples**

The experimental procedure contains three main parts: (1) prepare the resin chamber, (2) prepare the ICM measurements and fabricate the desired features, and (3) washing process. Detailed experiment steps are listed in the following paragraphs of this section.

(1) To prepare the resin chamber: Figure 24 shows a schematic of the resin chamber preparation procedure.

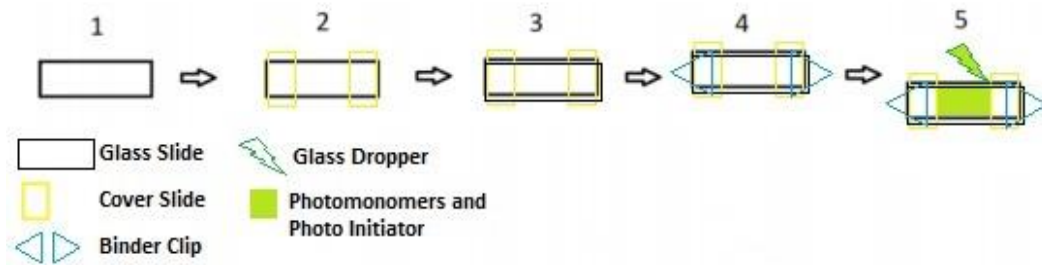


Figure 24. Schematic of Resin Chamber Preparation Procedure

Two glass slides are obtained from the box and cleaned. One is used as the bottom glass slide, and the other is used as the top glass slide. Firstly, place one glass slide on a cleaned platform. This is used as the bottom glass slide. Secondly, two cover slides are placed on the two sides of the bottom glass slide. These two cover slides are used as spacers. Thirdly, the other glass slide is placed on the top of the two spacers (i.e. cover slides). Fourthly, two binder clips are used to constrain the glass slide-spacer-glass slide construction. Finally, the solution of liquid photomonomers combined with photo-initiators are added between the two glass slides using a glass dropper. After the resin chamber is fulfilled with the photomonomer solution, a tissue is used to wipe out the residual photomonomer solutions at the edges of the resin chamber. Figure 25 shows a schematic of the prepared resin chamber [33].

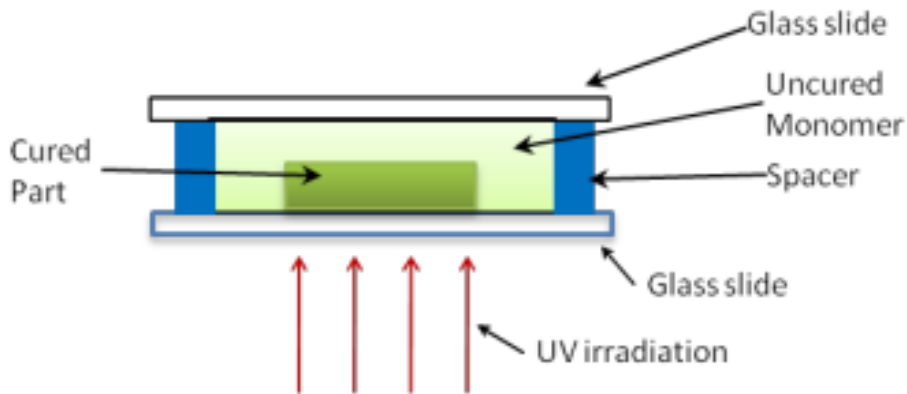


Figure 25. Schematic of the Prepared Resin Chamber [33]

(2) To start ECPL fabricating process and to use the ICM to record the video: the procedure is listed as the following steps:

- 2.1 Wear UV Protecting goggles.
- 2.2 Place the resin chamber onto the resin chamber platform.
- 2.3 Start the OmniCure® S2000, wait for 15 minutes for the intensity to be settled.
- 2.4 Connect the UV light guide to the DMD.
- 2.5 Change the intensity of the OmniCure® S2000 to the desired settings.
- 2.6 Connect power cord for the ICM laser diode.
- 2.7 Connect DMD power cord.
- 2.8 Check if the desired DMD pattern (controlled by Microsoft PowerPoint Software) is shown in the DMD.
- 2.9 Plug Ethernet cord for the ICM camera and start the ICM camera.
- 2.10 Adjust ICM Camera Exposure Time setting to get good ICM video.

2.11 Start recording the ICM video.

2.12 Control the DMD to start curing samples until the UV curing profiles ends.

2.13 After the UV curing profiles end, wait at least 10 second until the dark curing period ends. Stop the ICM video recording. Unplug the Ethernet cable on the ICM video camera to power off the ICM video camera.

2.14 Turn off UV light source (OmniCure® S2000).

2.15 Turn off the DMD by unplugging the DMD power cord.

2.16 Turn off the laser source by unplugging the power cord of the laser diode.

(3) Washing process and post curing: Figure 26 shows a schematic of the washing procedure. Detailed description of washing process is described as following:

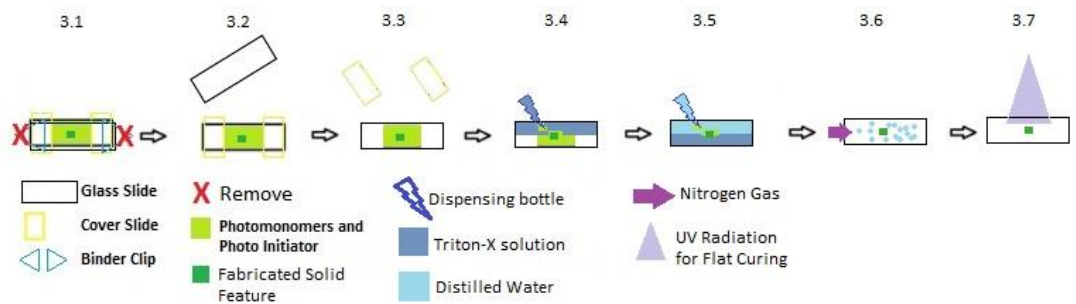


Figure 26. Schematic of Washing Process

3.1 Remove the two binder clips from the resin chamber.

3.2 Remove the top substrate of the resin chamber.

3.3 Remove the two spacers of the resin chamber.

3.4 Use the dispensing bottle to gently wash the bottom substrate (which contains the fabricated solid features) with the solution of water and Triton-X to remove the residual liquid photomonomers and photo-initiators.

3.5 After washing the bottom substrate with water and Triton-X solution, use dispensing bottle to gently wash the bottom substrate with distilled water until all the Triton-X solution are removed from the substrate. Repeat step 3.4 and 3.5 until (a) all the liquid photomonomers and photo-initiators are removed, and (b) all the Triton-X solution are removed.

3.6 Use compressed nitrogen gas to gently blow away the residual distilled water.

3.7 Place the cleaned sample under the UV projection for flat curing [33].

After the aforementioned steps, the desired features fabricated by the ECPL system are ready for dimension measurement. Both optical microscope and confocal microscope are used for measurements. Figure 27, Figure 28, and Figure 29 show three desired features cured by the ECPL system. Measurements from both the optical microscope and the confocal microscope are listed for each sample.

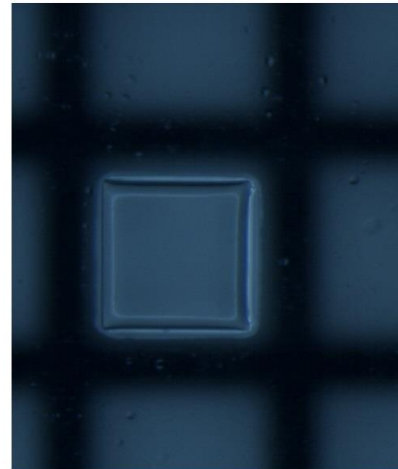
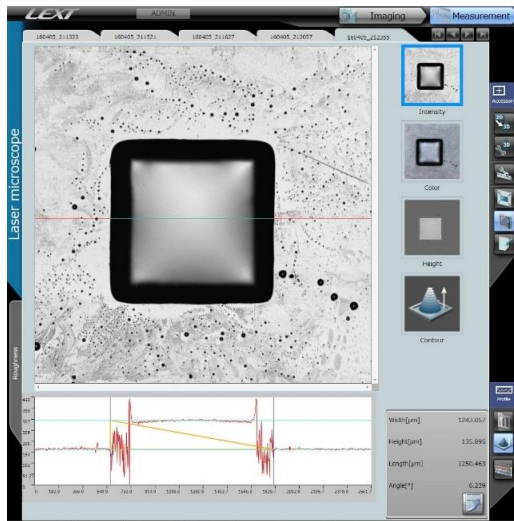


Figure 27. Desired Feature Fabricated By ECPL System Sample 1 (Left: Measurement from Confocal Microscope; Right: Measurement from Optical Microscope)

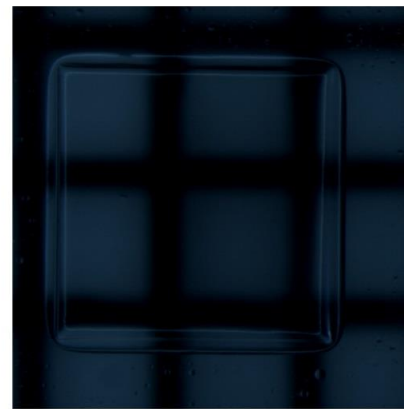
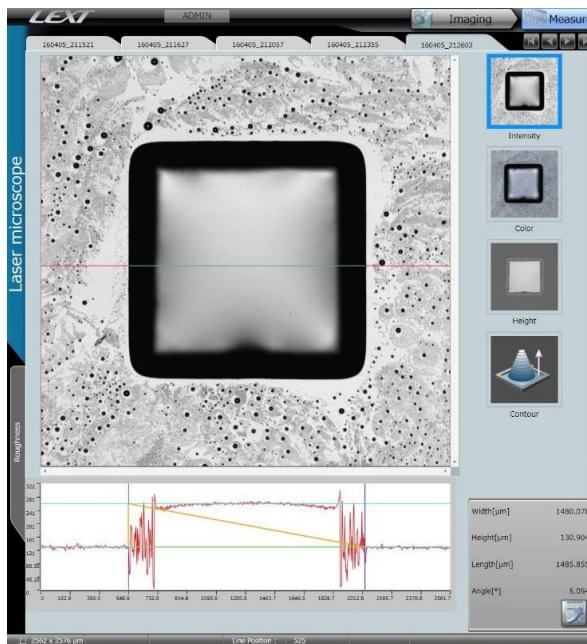


Figure 28. Desired Feature Fabricated By ECPL System Sample 2 (Left: Measurement from Confocal Microscope; Right: Measurement from Optical Microscope)

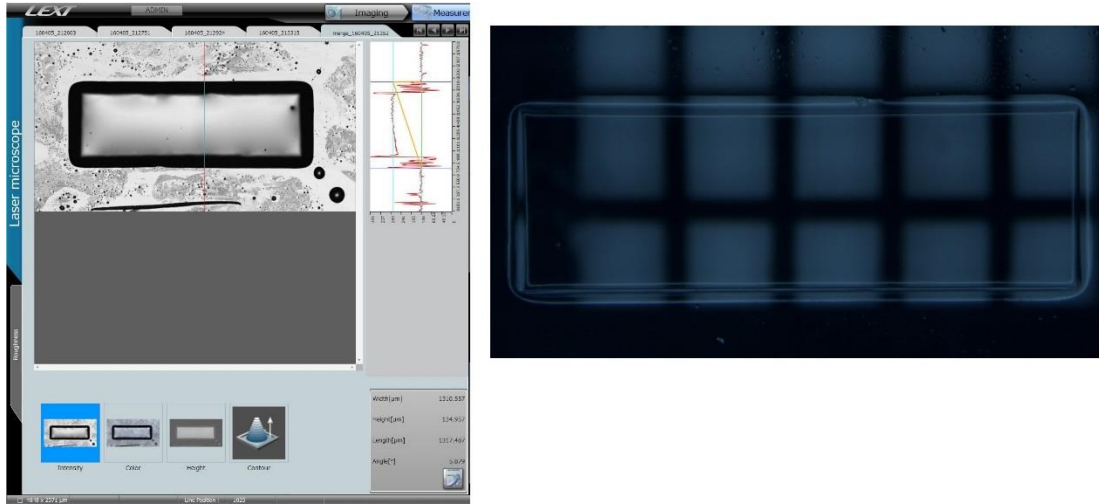


Figure 29. Desired Feature Fabricated By ECPL System Sample 3 (Left: Measurement from Confocal Microscope; Right: Measurement from Optical Microscope)

### 3.3 Chapter Summary

This chapter presented the design of the original ECPL and ICM system. The system setup and fabrication process was introduced. The limitation of using the lever-actuated iris was introduced. The experimental procedure of the ECPL fabrication was listed. The fabricated features of the ECPL system was presented.

## **CHAPTER 4. IMPROVED ICM SYSTEM AND WORKING PROCEDURE**

This chapter will introduce the existing ICM method with its limitation on causing errors. In order to improve the ICM method to better measure the dimensions of cured parts, the SLM is introduced into the system to reduce signal interference from measuring positions too close to each other. Improved ICM experiment procedure and related alignment procedure will be introduced in this chapter.

### **4.1 Improved ECPL and ICM System**

The original ECPL and ICM system has been introduced in CHAPTER 3. A photo of the original ECPL and ICM system is shown as Figure 23[42]. The ICM system includes part 1 to part 5 in green boxes in Figure 23, and the ECPL system includes part 1 to part 5 in blue boxes in Figure 23. During the curing process, the curing light from the UV source passes through the dynamic mask generator (DMD) which forms the curing light beam with its cross-section profile being controlled. The projection system focuses the light onto the resin chamber, and the light passes through the bottom transparent substrate of the resin chamber into the photopolymer resin to begin the curing process. The dynamic mask and exposure time determine the 3D dimensions of the part.

A schematic of the improved ICM system and the ECPL system is shown in Figure 30 [46]. Note that the Y axis is perpendicular into the paper. The ICM system includes part (1) to (8), and the ECPL system includes part (9) to (12) and the resin chamber and the UV filter.

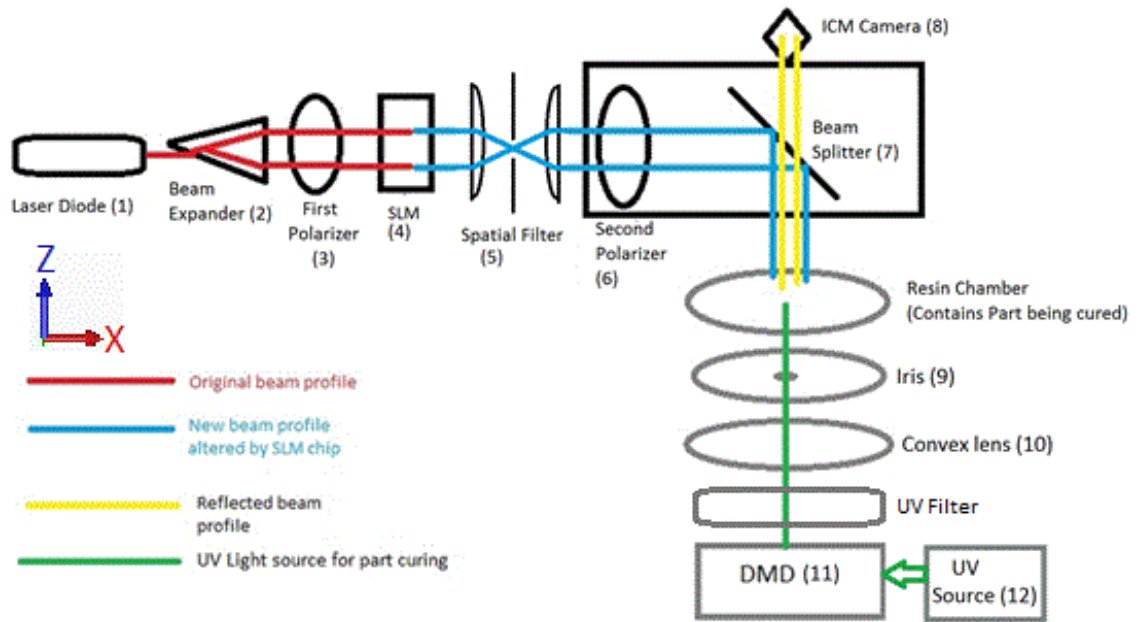


Figure 30. Schematic of ECPL system and ICM system (Y axis is perpendicular into the paper) [46]

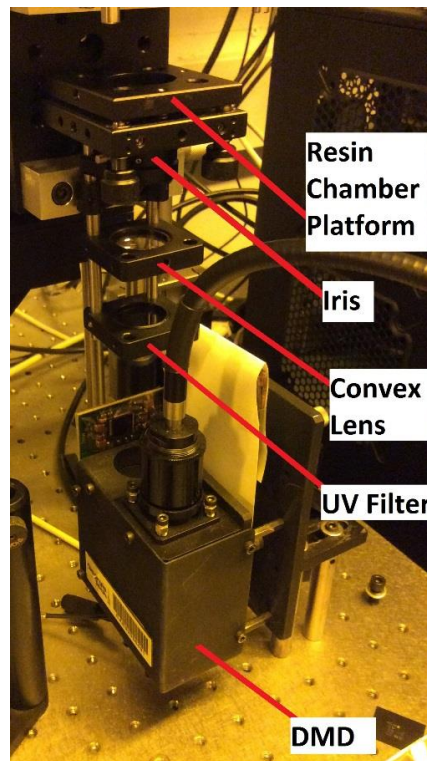


Figure 31. Photo of the ECPL System

Figure 31 shows a photo of the real ECPL system. Note that the UV source (refer to Figure 30) is not displayed on Figure 31. Note that the resin chamber (refer to Figure 30) is placed on the resin chamber platform (refer to Figure 31). During the curing process, the curing light from the UV source passes through the dynamic mask generator (DMD) which forms the curing light beam with its cross-section profile being controlled. The projection system focuses the light onto the resin chamber, and the light passes through the bottom transparent substrate of the resin chamber into the photopolymer resin to begin the curing process. The dynamic mask and exposure time determine the 3D dimensions of the part. The following paragraph shows detailed descriptions of the components of the ECPL system.

#### Radiation Source:

Refer to part (12) in Figure 30, the radiation source used is an Omnicure S2000 UV spot curing system produced by Lumen Dynamics. This radiation source produces UV radiation at wavelength centered at 365 nm. This wavelength was selected to initiate crosslinking in the photopolymer. The resulting beam was introduced into the DMD through a 7 mm optic fiber which guide the light.

#### Dynamic Mask Generator:

Refer to part (11) in Figure 30, the dynamic mask generator consists of a Digital Light Innovations' CEL5500 Light Engine. This is a Digital Micromirror Device (DMD) that consists of an array of micro-mirrors. The DMD is controlled as a secondary computer monitor using Microsoft PowerPoint software. The figures displayed by PowerPoint are

converted into grayscale information and are sent to the DMD. The DMD then projects the corresponding grayscale radiation upwards to the substrate of the resin chamber.

#### Projection System:

The projection system consists of an FB360 bandpass filter, a LA1255 convex lens (part (10) in Figure 30) (25 mm diameter and 50 mm focal length) and an SM1D12 Iris (part (9) in Figure 30) from ThorLabs, Inc. The bandpass filter could filter out the radiation source at wavelength other than 340-370 nm. The iris could open a pinhole with diameter ranging from 0.8-12 mm. This projection system is used to sharpen the acutance of the dynamic mask and reduce the noise from radiation at wavelength other than the curing wavelength.

#### Resin Chamber Platform:

Refer to Figure 31, the resin chamber platform consists of a KC1-T kinematic mount from Thorlabs, Inc. When fabricating features using the ECPL system, the resin chamber is placed on the top of this platform. This platform can adjust its angular positions (with respect to the X and Y axes in Figure 30) relative to the DMD. Thus, with these adjustments, the UV curing source from the DMD could hit the bottom substrate of the resin chamber at 90 degree angle, making the curing UV profiles accurate for fabrications.

#### Resin Chamber:

The resin chamber consisted of two glass slides separated by spacers of known thickness. The photopolymer resin was loaded between the two glass slides. The photopolymer resin crosslinks inside this resin chamber when exposed to UV radiation.

The improved ICM system, shown in Figure 32, was based on a Mach-Zehnder interferometer [43]. Note that the Y axis is perpendicular into the paper. A coherent laser is directed, through a beam expander, a polarizer, an SLM chip, a spatial filter, another polarizer, and beam splitter, at the resin chamber. Light reflecting off of the top and bottom surface of the resin chamber's two transparent bounding surfaces reflect through the beam splitter and into the camera.

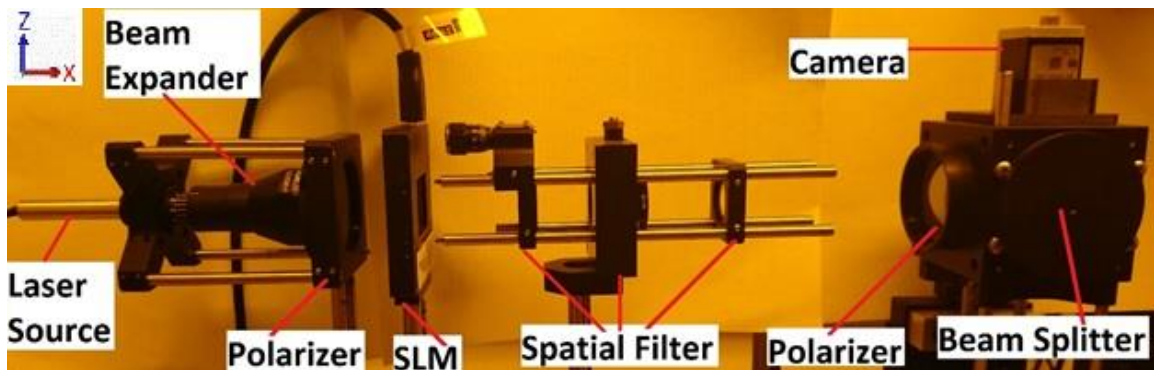


Figure 32. Photograph showing the experimental ICM System Setup (Y axis is perpendicular into the paper) [46]

### Laser Source

Refer to part (1) in Figure 30, the laser source consisted of a CPS532 Collimated Laser Diode from ThorLabs, Inc. The purpose of this diode was to provide the coherent laser light (at wavelength of 532 nm) required for interferometry.

### Beam Expander

Refer to part (2) in Figure 30, the purpose of the beam expander was to expand the narrow beam produced by the laser source such that the light output is capable of

selectively scanning at any location inside and near the curing region such that any point around the curing region can be analyzed by the camera.

### SLM system

The SLM system was composed of a polarizer (part (3) in Figure 30), an SLM chip (part (4) in Figure 30), the spatial filter (part (5) in Figure 30) which was composed of convex lens-iris-convex lens, and another polarizer (part (6) in Figure 30). The SLM allows laser light to pass through its transparent region. This transparent region features 36.9 x 27.6 mm in dimension, and the resolution of 1024 x 768 pixel. Each pixel region is 36 x 36  $\mu\text{m}$  [44]. The SLM could separately change the phase angle of the laser passing through each of the pixel regions on the SLM. The two polarizers, one before the SLM and the other after the SLM, together perform as a band-pass filter which only allow the light, within a certain range of phase angle, to pass through this two-polarizer combination. For a pixel region of the SLM, by using the SLM to change the laser beam's phase angle to a value which is outside the two-polarizer combination's transmittable phase angle range, the polarizer-SLM-polarizer system could block the laser beam passed through and controlled by this SLM pixel region. On the other hand, if the SLM changes the laser beam's phase angle to a value which is within the two-polarizer combination's transmittable phase angle range, the laser beam is able to pass through this polarizer-SLM-polarizer system. Thus, the SLM with the two polarizers together perform as an electronic iris with a resolution of 1024 x 768 pixel for a 36.9 x 27.6 mm rectangular region [44]. With a laser beam with large cross-section profile as an input, this system could generate multiple isolated beams of laser by blocking the surrounding regions of these isolated laser beams. In addition, this polarizer-SLM-polarizer system could be computer-programmed

to move these isolated laser beams with respect to time. Thus, the SLM chip with two polarizers on each side of it functions as a movable iris. The spatial filter was added to reduce the diffracted laser patterns which were created when the laser beam passes through the SLM chip.

### Camera

Refer to part (8) in Figure 30, the purpose of the camera was to capture the intensity of laser light reflected back from the resin chamber, across the entire curing area. The intensity profile of the resulting laser light shows the interference patterns. Tracking the interference patterns enables calculating the phase shift caused by change in refractive index of the photopolymer being cured inside the resin chamber.

Compared with the original ICM system, the improved ICM system replaces the lever-actuated iris by an electronic iris system. The SLM system has two functions: to reduce the radius of the laser profile from a circle with large radius to any shapes that were desired and with smaller dimensions, and to enable moving that small profile in lateral directions parallel to the resin chamber. These two functions are necessary to monitor the photopolymerization process.

The ICM system was found to be very dependent on the system alignment. Minimal misalignment of any parts in the ICM system will deteriorate the ICM measuring results since the laser path is misaligned. One special misalignment problem of the laser in the ICM system was caused by the spherical aberration in the spatial filter of the ICM system. The spherical aberration is an optical effect observed in normal convex lenses: the focal length of a convex lens is not homogeneous among different locations in the radial

direction. The focal point is closer to the convex lens when the light is hitting near the edge of the convex lens, whereas the focal point is further to the convex lens when the light is hitting near the center of the convex lens. As a result, there exist multiple focal points of a convex lens along its centerline. Figure 33 shows two light paths when the light passes through a convex lens. The top figure of Figure 33 shows the light path without spherical aberration, and the bottom figure of Figure 33 shows the light path with spherical aberration [45].

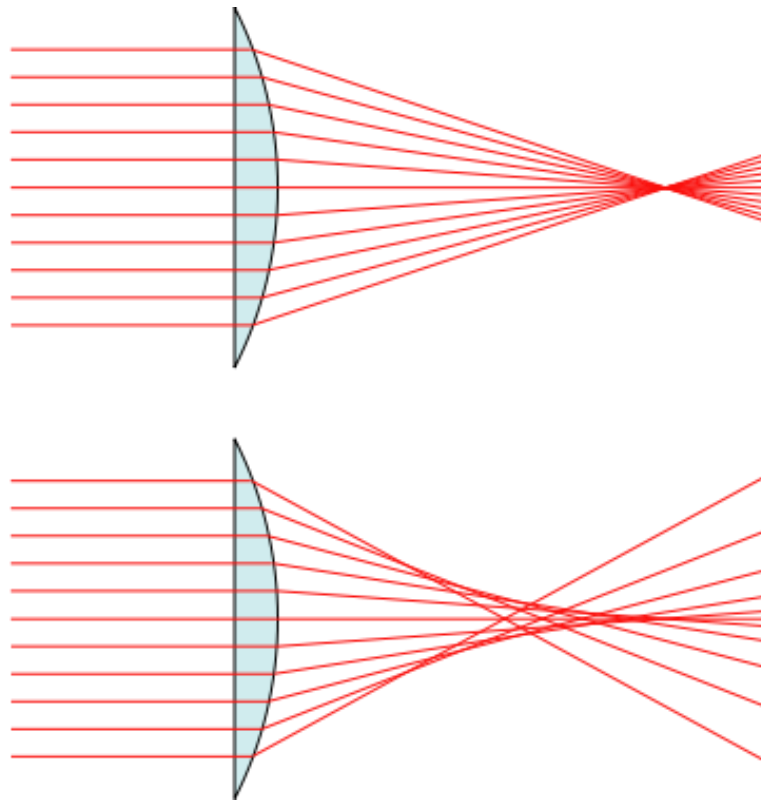


Figure 33. Top Figure: Light Passing Through a Convex Lens Without Spherical Aberration; Bottom Figure: Light Passing Through a Convex Lens With Spherical Aberration [45].

When the spatial filter system in the improved ICM system was firstly built, two normal convex lenses were used. The spherical aberration phenomenon caused the collimated laser profile, after passing through the spatial filter, became convergent then divergent. Figure 34 shows a schematic of the “un-collimated” light path when the laser passed through the spatial filter which consisted of two normal convex lenses that had the spherical aberration problem. Figure 35 shows a zoomed-in view of Figure 34 showing the details of the spherical aberration phenomenon. The gray lines in Figure 34 and Figure 35 shows the paths of laser light consisted in the large laser profile, and the green Lines in Figure 34 and Figure 35 shows the outer boundaries of the laser profiles.

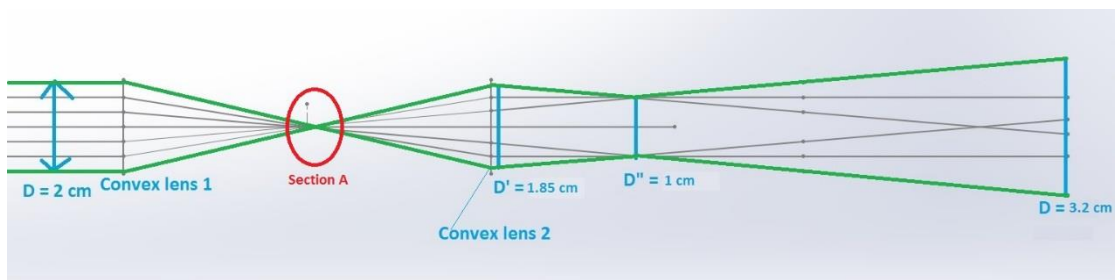


Figure 34. A Schematic of The “Un-Collimated” Light Path When the Laser Passed The Spatial Filter Consisting Of Two Normal Convex Lenses

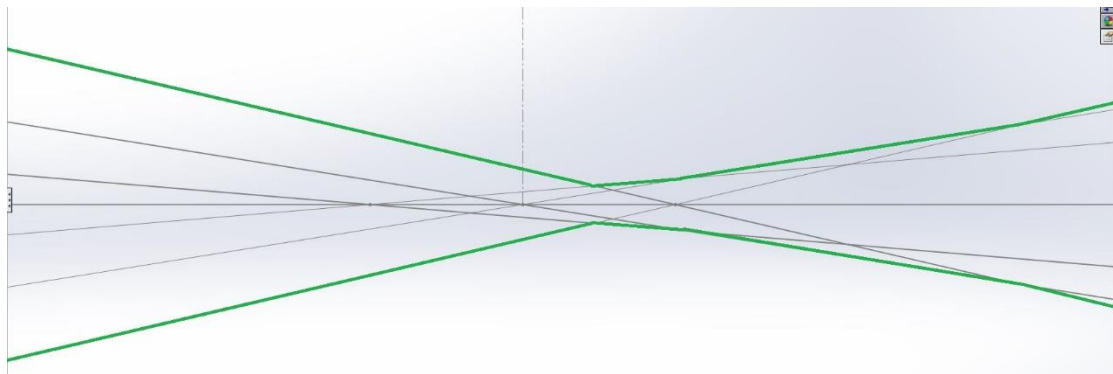


Figure 35. A Zoomed-in View of Section A in Figure 34

In order to keep the laser profile, after passing through the spatial filter, to be collimated, aspheric lenses from Edmund Optics (Stock No. #89-432) has been purchased and replaced the normal convex lenses in the spatial filter system. After the aspheric lenses has been introduced, the spherical aberration problem has been largely reduced.

Because the laser beams in the ICM system travels vertically upward from the resin chamber to the camera, the lateral dimensions of the cured part (refers to the X and Y axis in Figure 30 and Figure 32, in the directions vertical to the cured part growth) and the dimensions determined by the ICM camera should have conversion ratio of 1:1. The size of each pixel in the ICM camera is  $2.2 \times 2.2 \mu\text{m}$ , and the ICM camera utilizes a binning function of 4 [47]. Since the minimum pixel distance in the ICM camera detected by the improved ICM system is 5 pixels, the theoretical resolution of the improved ICM system is expected to be  $2.2 * 4 * 5 = 44 \mu\text{m}$ . However, due to the limitation in system alignment, the real resolution will be lower than 44 microns. The procedures of ICM system alignment, ICM frame identification and signal processing will be discussed in the next section.

## **4.2 Revised Experimental Procedure**

### *4.2.1 ICM System Alignment and Contrast Check*

Alignment plates with pinholes are used in order to check the alignment of the system. The procedure to align the ICM system is listed in the following:

1. To align the laser diode and beam expander (refer to part 1 and part 2 in Figure 30): place a pinhole at the center of the beam expander (referred as “Pinhole 1”) to get a small laser beam from the center of the beam expander. Place an alignment plate (with a

small pinhole at the center of the alignment plate) (referred as “Alignment Plate 1”) at the center of the second polarizer (refer to part 6 in Figure 30). Place an alignment plate at the center of the resin chamber platform (refer to the Resin Chamber in Figure 30) (referred as “Alignment Plate 2”).

1.1: To align the beam expander in z direction (refer to Z axis in Figure 30.) move the beam expander (as long as the laser diode, since the laser diode is mounted at the end on the beam expander) in z direction so that the small laser beam from the beam expander hits the center of the Alignment Plate 1 in z direction.

1.2: To align the direction in x and y and the rotation axis in z direction of the beam expander, change the position in x-y plane (refer to X and Y axis in Figure 30) and the rotation angle in z axis (refer to Z axis in Figure 30) so that the laser beam from the beam expander pass the center of the Alignment Plate 1 (in the y-z plane, refer to Figure 30). Make sure that the laser beam also hit the Alignment Plate 2 at its center in y direction (refer to Y axis in Figure 30).

2. To align the spatial filter (refer to part 5 in Figure 30): Remain Pinhole 1 at its original position. Place an alignment plate (with a small pinhole at the alignment plate’s center) (referred as “Alignment Plate 3”) at the center of the first aspheric lens (the aspheric lens that is closer to the beam expander) of the spatial filter. Remain the Alignment Plate 1 and Alignment Plate 2 at their original position.

2.1: To align the spatial filter with the beam expander in z direction (refer to Z axis in Figure 30), change the position of the spatial filter in z direction so that the small

laser beam from the beam expander hits the center of the Alignment Plate 3 in z direction.

2.2: To align the spatial filter in x-y plane and in the rotation axis of z-direction (refer to the X, Y and Z axes in Figure 30), change the position of the spatial filter in x-y plane so that the laser beam from beam expander hits the center of the Alignment Plate 3 in its y-z plane. Then change the position of the spatial filter in x-y plane and rotate it with respect to z-axis so that the laser beam also hits Alignment Plate 1 at its center in y-z plane and also the Alignment Plate 2 at its center in y direction.

3. To align the beam splitter (refer to part 7 in Figure 30): Remain pinhole 1 at its original position. Remain Alignment Plate 2 at its original position. Place an alignment plate (referred as “Alignment Plate 4”) on the top of the cage plate which the convex lens (refer to part 10 in Figure 30) is mounted on. Make sure the Alignment Plate 4 is at the center of the convex lens (refer to part 10 in Figure 30) in the x-y plane (refer to the X and Y axes in Figure 30)

3.1: To align the beam splitter position in the x-z plane (refer to the X and Z axes in Figure 30), make small changes to the position of the beam splitter in the x-z plane.

3.2: To align the beam splitter angle with respect to y-axis (refer to the Y axis in Figure 30), rotate the beam splitter with respect to the y-axis so that the laser beam hits the center of the Alignment Plate 2 in the x-y plane.

3.3: To align the beam splitter position in the x-z plane and its angle with respect to y-axis, check if the laser beam passes through the pinhole at the center of the Alignment

Plate 2 and hits the center of the Alignment Plate 4 in the x-y plane. If not, repeat step 3.1, 3.2 and 3.3 over and over again until the small laser beam from the beam expander hits both the centers of the Alignment Plate 2 and Alignment Plate 4 in the x-y plane.

4. To align the pinhole of the spatial filter (refer to part 5 in Figure 30) in y-z plane (refer to the Y and Z axes in Figure 30) and modify the pinhole size: Remove the Pinhole 1 to get a large laser profile at the resin chamber (refer to the Resin Chamber in Figure 30). Insert the SLM (refer to part 4 in Figure 30) into the ICM system. Gradually reduce the pinhole size and change the position of the spatial filter in y-z plane so that the laser profile shape and size at the resin chamber is the same as the laser profile shape and size after the beam expander. Make sure that there are no diffracted laser profiles coexisting with the original laser profile.

After the 4 steps mentioned above, the contrast of the SLM system should be set to the maximum. The contrast of the SLM system is defined by the difference between the intensities of the laser profiles, after passing through the second polarizer (refer to part 6 in Figure 30) and hitting at the resin chamber, when the SLM is controlled to project a white image and when the SLM is controlled to project a black image. The contrast is controlled by the relative angle between the two polarizers (refer to part 3 and part 6 in Figure 30) with respect to the x-axis (refer to the X axis in Figure 30). The procedure to maximize the contrast is listed as step 5:

5. To maximize the contrast of the SLM system: Use the computer to control the SLM to project a white image (which the intensity of the image is defined as 255/255). Rotate the second polarizer (refer to part 6 in Figure 30) with respect to x-axis (refer to the

X axis in Figure 30) to find the angular position such that the laser profile at the resin chamber is at its maximum.

After step 5, another step is needed to finely adjust the position of the SLM in y-z plane (refer to the Y and Z axes in Figure 30). This procedure is listed as step 6:

6. To finely align the SLM in y-a plane: Use the computer to create a black image with size of 1024x768 pixel and with a “+” mark in white at the center of this image. Project this image on the SLM. Place a glass slide on the top of the resin chamber platform (refer to the Resin Chamber in Figure 30). Start the ICM camera (refer to part 8 in Figure 30) to record reflected laser from the resin chamber. The image recorded by the ICM camera should have a bright “+” mark. Move the SLM in y-z plane so that the bright “+” mark is at the center of the video frames recorded by the ICM camera.

#### *4.2.2 Time-varying Scanning Method and ICM Detecting Frame Identification Procedure*

The time-varying scanning method utilized 6 sets of SLM detecting matrices. Each of these 6 detecting position sets sampled a 4x3 array of small regions, each of which was 10x10 pixels on the SLM in size (which is 88x88 microns). These regions were spaced 24 pixels apart, and each column of regions was offset 6 pixels from the previous column. These regions were defined to let the ICM detecting beam pass through the SLM. There were  $6 \times 4 \times 3 = 72$  positions to be monitored by the time-varying scanning method in this thesis study. The SLM system controlled the ICM detecting laser beams to sequentially measure these 6 sets of 4x3 positions, and the intensities from the reflected ICM laser at these 6 sets of 4x3 positions were sequentially captured by the ICM camera. During the

ICM monitoring process, the reflected ICM laser intensities captured by the ICM camera as a function of time, at these 6 sets of 4x3 positions, generated the interferograms at these  $6 \times 4 \times 3 = 72$  positions.

When the SLM was controlled to display these 6 SLM detecting matrix sets, there was also an additional 10x10 pixel region opened on the SLM which was called the SLM frame indicator. The position of the SLM frame indicator was unique for each of the 6 SLM detecting matrix sets. These unique positions were used to indicate which of the 6 SLM detecting matrix sets the current ICM video frame corresponded to. It is important to know the corresponding SLM detecting matrix set mentioned above, since for each of the SLM detecting matrix sets (which was 4x3 array of small regions) there was also a unique corresponding set of 4x3 point-positions defined on the ICM video frame which was called the ICM detecting positions.

These ICM detecting positions and SLM frame indicator positions were pre-calibrated before the experiment so that the ICM detecting position sit at the center of the corresponding reflected light from the 10x10 opened positions (the SLM detecting matrix) on the SLM. The grayscale intensity values (out of 255) at the SLM frame indicator positions were recorded to get the threshold intensities of these 6 SLM frame indicator positions.

Before each trial which the ECPL system starts curing samples and the ICM starts recording the interferograms, there is a “Pre-Experiment” step. In this step, the ICM camera records the reflected laser profiles when each of these 6 SLM detecting matrix sets are displayed on the SLM. This recorded ICM frames are needed to make sure that the

locations of the 6 SLM frame indicator positions on the ICM frames show observable higher intensities (i.e. the threshold intensities of the 6 SLM frame indicator positions) than their surroundings. This step also enables people to get the precise 6 SLM frame indicator positions and their corresponding threshold intensities for each ICM video which records the interferograms when the ECPL system cures the parts.

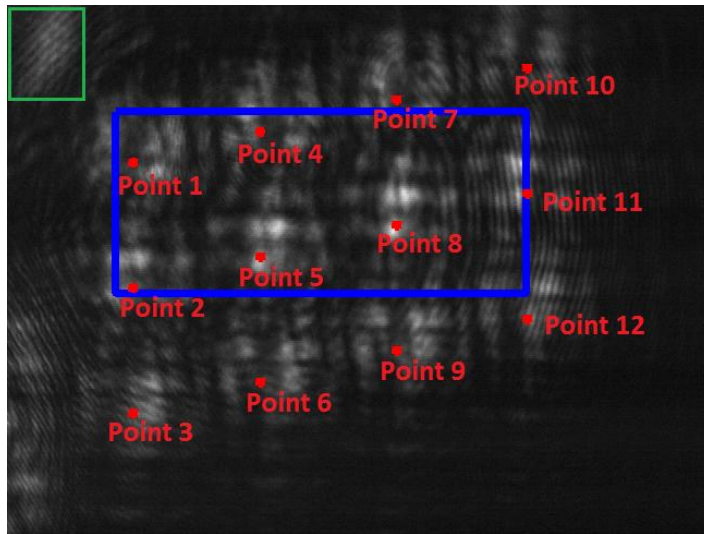


Figure 36. First set of ICM detecting locations on the ICM video

Figure 36 shows the ICM video frame in which light was gathered from the reflected ICM laser from the first SLM detecting matrix set. In addition, the first set of ICM detecting positions was indicated by the red points 1-12. The green rectangle indicates that the SLM frame indicator for the first set of the SLM detecting matrix (i.e. the ICM detecting position of the first set of the SLM detecting matrix) was located at the top-left corner of the ICM video frame where the intensity is higher than the black background. The blue rectangle indicates the UV radiation region on the ICM video frame. Note that the contrast of Figure 36 has been converted larger by a factor of 5. The reason of this conversion will be discussed later in this section.

Another important step is to convert the ICM videos to a higher contrast. One method to describe the contrast of the ICM videos is the amplitude of the intensity oscillations in the ICM-recorded interferograms. In the ICM system, the contrast is controlled by the Camera Exposure Time for each frames recorded by the ICM camera. If the Camera Exposure Time is set to be high, the camera is more sensitive to the reflected laser, the contrast of the interferograms will be large, and the SLM frame indicator positions can be easily gathered in the “Pre-Experiment” step. On the other hand, if the Camera Exposure Time is set too high, the high intensities in the interferograms will be over 255. However, since the maximum intensity recorded by the camera is 255, those intensities will be recorded as 255. Figure 37 shows an example of overly-exposed interferogram and its corresponding adequately-exposed interferogram.

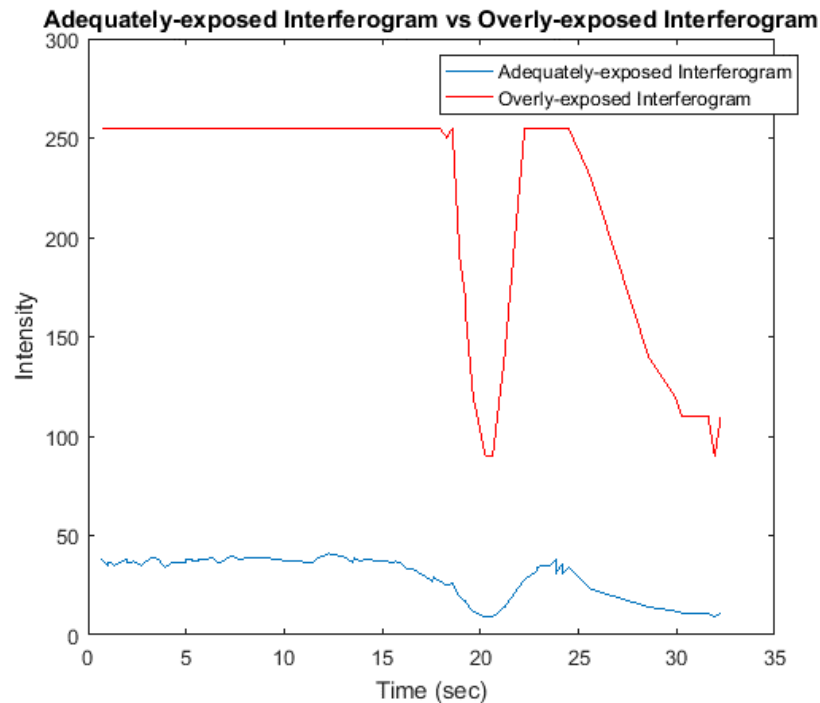


Figure 37. An example of overly-exposed interferogram and its corresponding adequately-exposed interferogram

As shown in Figure 37, the red line shows the interferogram when the Camera Exposure Time is set too high, and the blue line shows the corresponding interferogram when the Camera Exposure Time is adequately set. There exist flat tops in the red line which corresponds to intensities which should be over 255 but cannot be recorded. In this case, the Camera Exposure Time of the red line should be reduced so that the peaks of the interferograms could be correctly recorded.

Another reason that the Camera Exposure Time should not set to be high is to avoid “blurred” frames. Since the time shift between two SLM detecting frames is very small, the Camera Exposure Time should be set low enough so that each ICM video frame records sharp image. Otherwise, the ICM video will get “blurred” images where two SLM detecting frames are mixed together. Figure 38 shows an example of “blurred” ICM video frame.

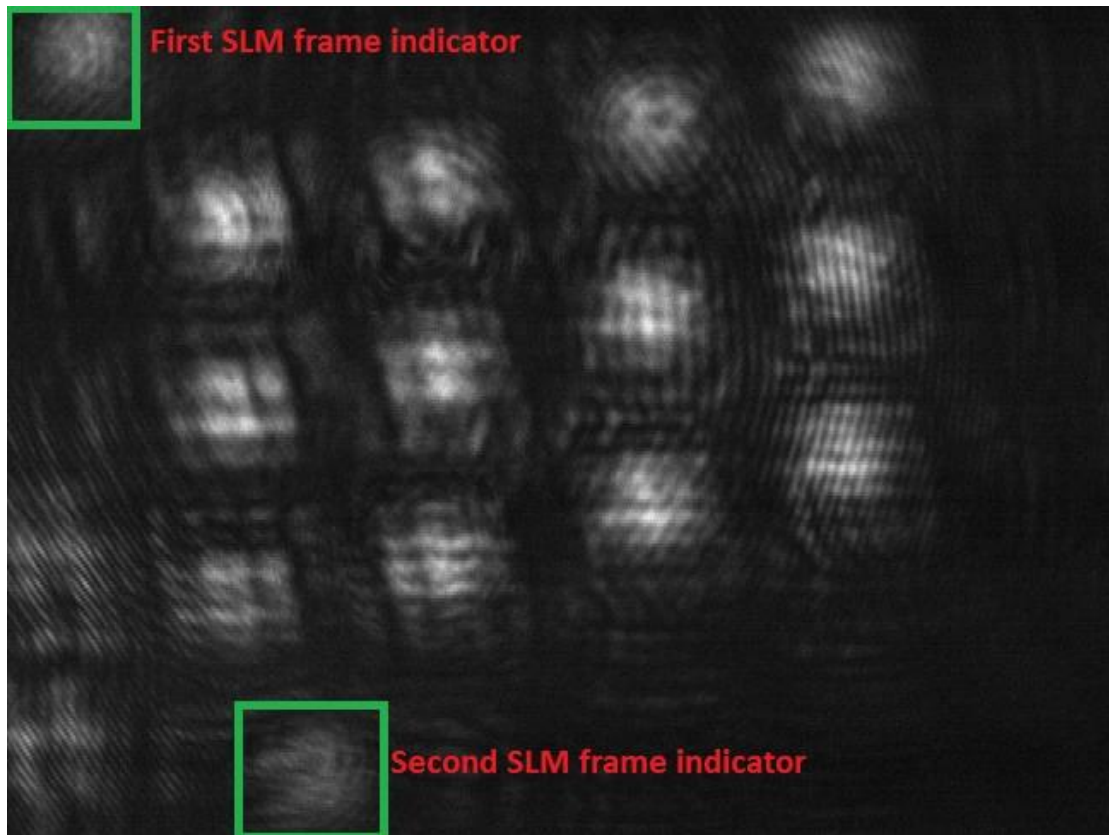


Figure 38. An Example of “Blurred” ICM Video Frame

As shown in Figure 38, both the SLM frame indicator positions of the first and second SLM frame indicators, indicated in the two green boxes, coexist in the same ICM video frame. This means that this ICM video frame contains information of interferograms of both the first and second SLM detecting frames, which cannot be possible. In this case, this ICM video frame cannot be used to compose the interferograms. Thus, the Camera Exposure Time should not be set too high.

Nevertheless, there are also drawbacks when the Camera Exposure Time is set too low. Firstly, the amplitude of the intensity oscillations will be too small to differ intensity oscillations from non-oscillations in the interferograms. Secondly, in the “Pre-experiment” step, if the Camera Exposure Time is set lower, the ICM camera is less sensitive to the

reflected laser profiles, and the SLM frame indicator positions are harder to be found. The threshold intensities of the SLM frame indicator positions are also hard to be set. Figure 39 shows the original frame showing the first set of ICM detecting locations on the ICM video. Note that Figure 36 is directly converted from Figure 39. Similar to Figure 36, the first set of ICM detecting positions was indicated by the red points 1-12. The green rectangle located at the top-left corner of the ICM video frame indicates the ICM detecting position of the first set of the SLM detecting matrix). The blue rectangle indicates the UV radiation region on the ICM video frame.

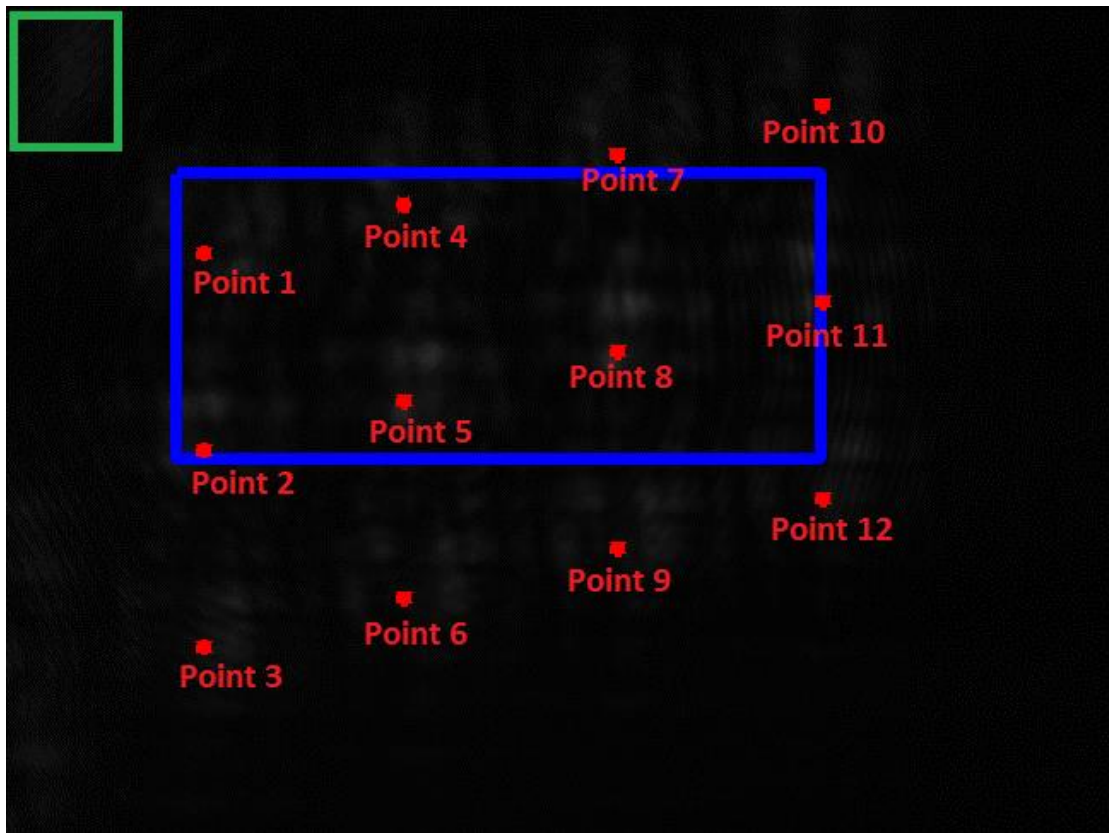


Figure 39. The Original ICM Video Frame of Figure 36

Compared with Figure 36, human eyes cannot differ the intensity in the green box from the intensities from its surroundings. In this case, if the original ICM video is used,

the SLM frame indicator positions could not be found in the “Pre-experiment” step, and the threshold intensities for each SLM frame indicator positions could not be set.

In order to overcome this problem, the Camera Exposure Time for the experiment is firstly set to be lower than the Camera Exposure Time which the SLM frame indicator positions are easy to be detected by human eyes, then the contrast of the video is manually converted to a higher value. The conversion of the contrast is done by multiplying all the pixel intensities in all the ICM video frames by a factor of 5. Figure 40 shows a comparison of the ICM-recorded interferograms of the same location of the same experiment, with the contrast converted to high and without the contrast conversion.

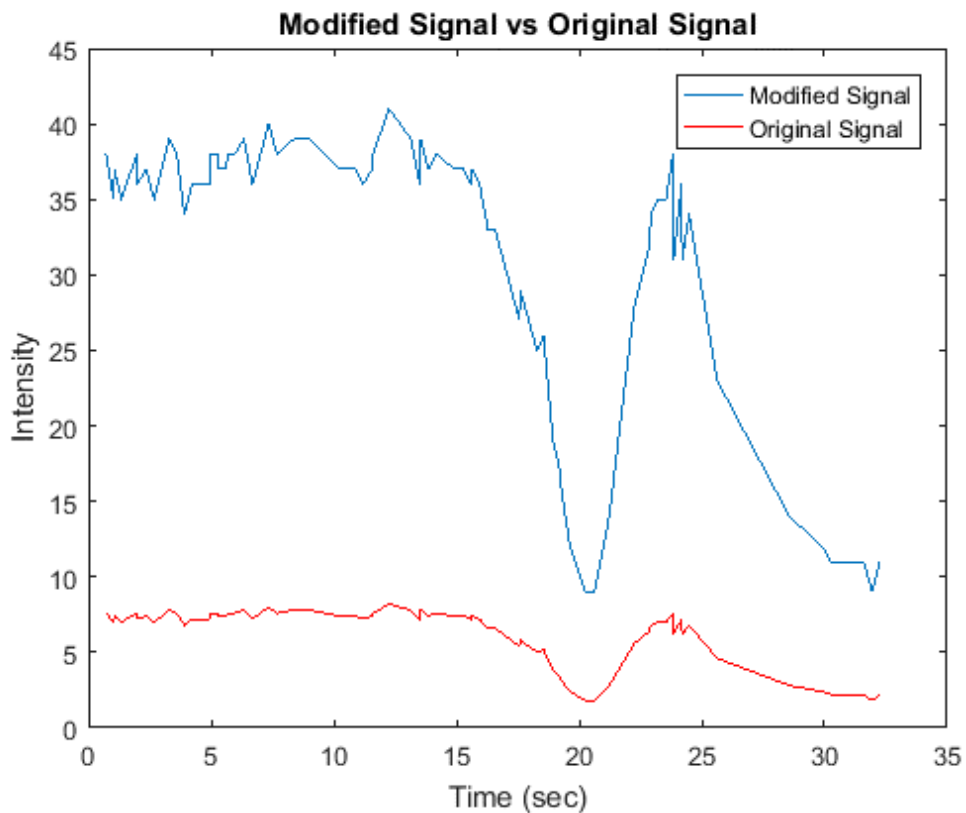


Figure 40. Comparison between Converted Interferogram and Original Interferogram

As shown in Figure 40, the modified signal which is gathered from converted ICM video (the video that the contrast is amplified by a factor of 5) shows larger amplitude of intensity oscillation. In addition, the comparison between Figure 39 and Figure 36 shows the effectiveness of amplifying the contrast of the ICM recorded video in finding the ICM detecting locations. These two illustration prove the necessity of amplifying the contrast of the ICM-recorded video.

Figure 41, Figure 42, Figure 43, Figure 44, and Figure 45 show the 5 typical converted ICM video (the video that the contrast is amplified by a factor of 5) frames other than Figure 36, and each of them corresponds to the other 5 SLM detecting matrix sets (i.e. the other 5 sets of 4x3 arrays of 10x10 small regions opened on the SLM) and their corresponding SLM frame indicators. Similarly, these 5 figures also correspond to the 5 sets of ICM detecting positions indicated by the red points.

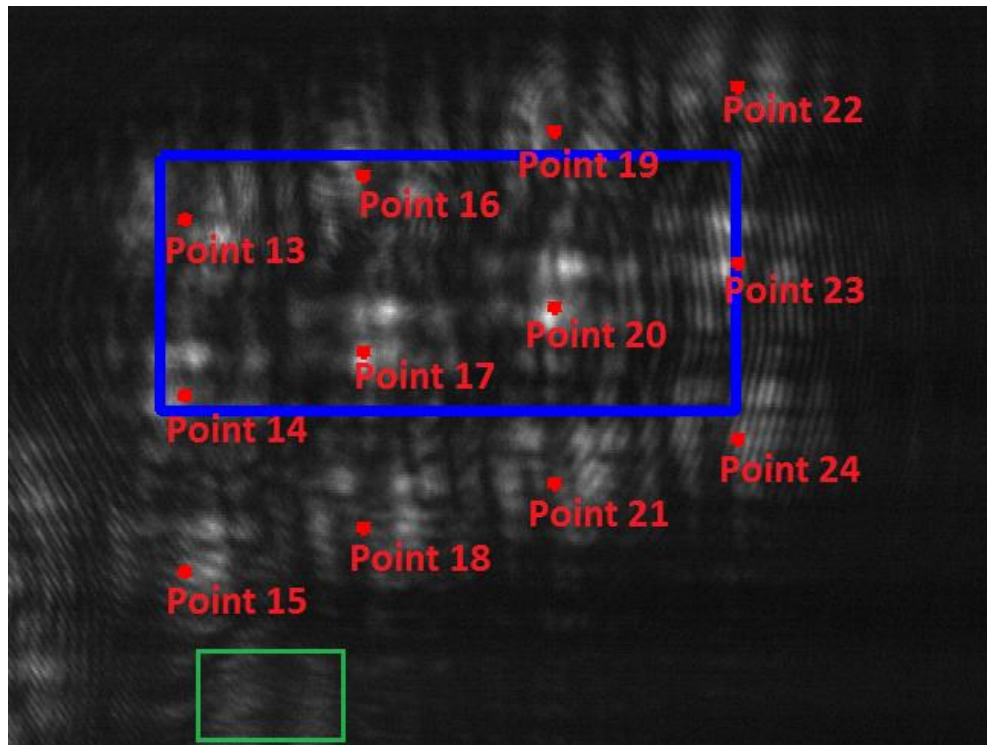


Figure 41. Second Set of ICM Detecting Locations on the Converted ICM Video

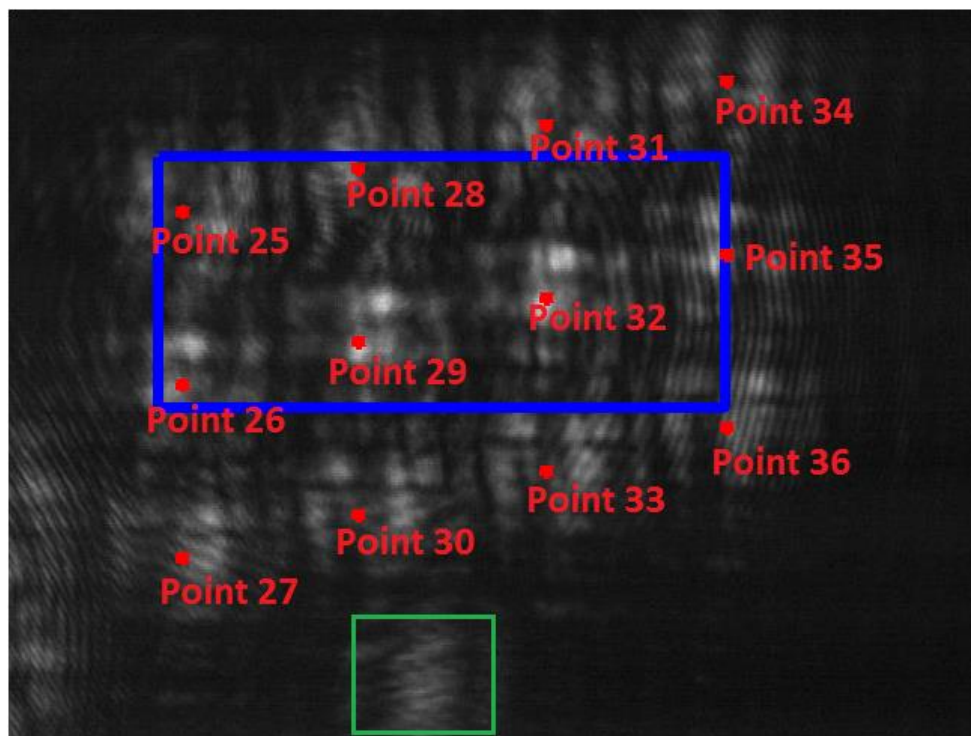


Figure 42. Third Set of ICM Detecting Locations on the Converted ICM Video

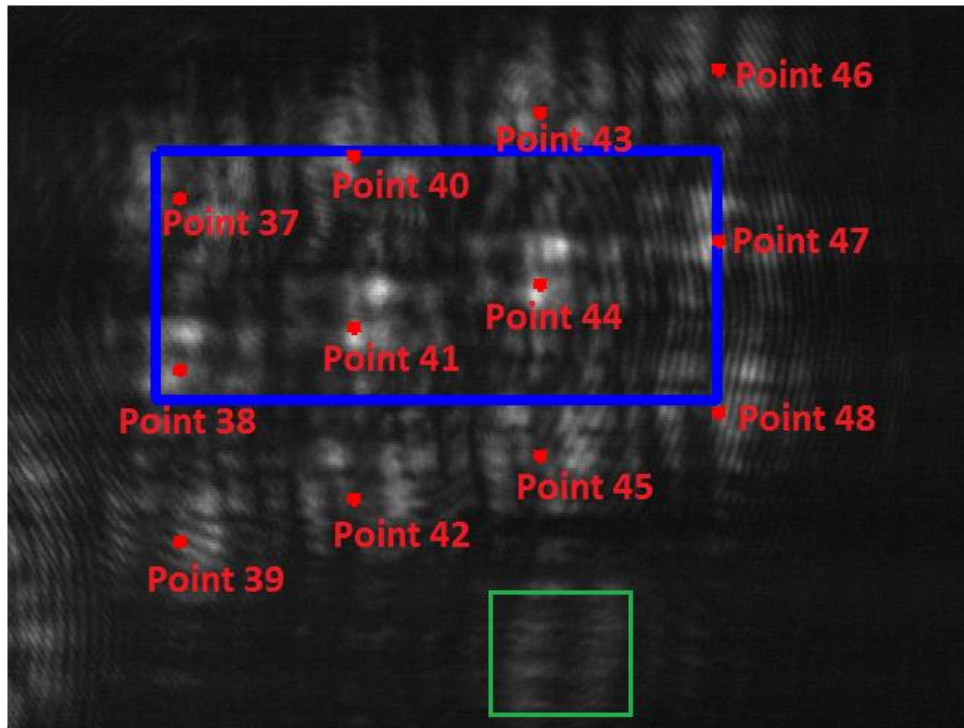


Figure 43. Fourth Set of ICM Detecting Locations on the Converted ICM Video

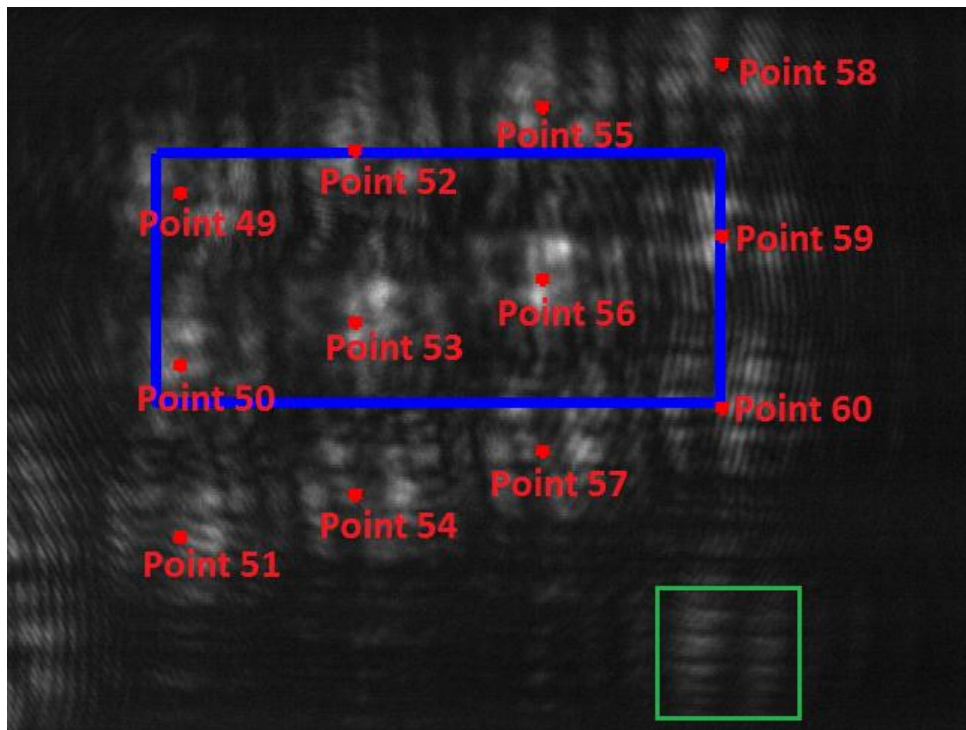


Figure 44. Fifth Set of ICM Detecting Locations on the Converted ICM Video

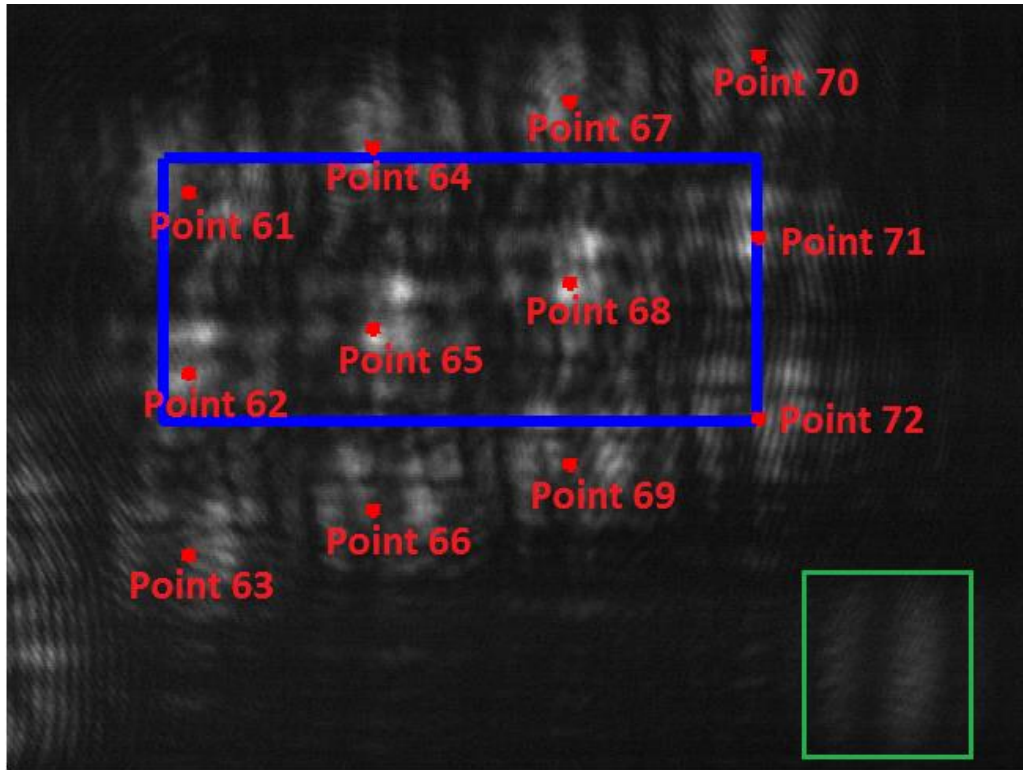


Figure 45. Sixth Set of ICM Detecting Locations on the Converted ICM Video

#### 4.2.3 Signal Processing Procedure

The frame rate for the ICM-captured video was set as 35 Hz. After the ICM camera capture the ICM video for the whole curing process, it is analyzed to get the interferograms at each of the SLM detecting matrices. There is an identification process, consisting of two steps, before analyzing each of the ICM video frames: 1) The first step is, for each frame in the ICM video, the frame is defined as “functional” if and only if it contains only one of the six sets of SLM detecting matrices; this evaluation is achieved by identifying if only one of the six SLM frame indicators showed reflected light (that reached a pre-calibrated threshold light intensity) in each ICM video frame. 2) The second step is, for each frame in the ICM video, after the frame is identified to be “functional”, the SLM frame indicator position is used to identify which ICM detecting position set is illuminated. For each ICM

video frame that passes the 2-step identification process, the intensity values (out of 255) at the corresponding ICM detecting positions, associated with the time step information of that ICM video frame, are stored to create the intensity vs time plots, which are the interferograms for each detecting positions. These interferograms are then analyzed by MATLAB to get the total number of phase changes and to estimate the cured part height at the 72 ICM detecting locations. Figure 46 shows a block diagram of the whole signal processing procedure. The following paragraph provides a summary of this flowchart:

Given a video captured by the ICM system, each frame of the video is either categorized as a video frame of one of the 6 sub-videos or deleted. For each of the ICM video frame, the average intensity at the 6 SLM frame indicator locations are calculated. For each SLM frame indicator location, if the intensity at this location is higher than the threshold intensity of this location, the ICM video frame is defined to have this SLM frame indicator “on”. The ICM video frame will be categorized if and only if only one SLM frame indicator is “on” for this video frame. This video frame will be categorized as a frame of the  $i^{\text{th}}$  sub-video based on the fact that only the SLM frame indicator of the  $i^{\text{th}}$  set of ICM Detecting Locations. After categorizing all the ICM video frames to form the 6 sub-videos, these sub-videos are analyzed, and the cured part dimensions are calculated based on the proposed signal decoding method, described in page 41, by Zhao X. et al. [40].

The meanings of the abbreviations mentioned in Figure 46 are listed as following:

SFIP1 – SFIP6: SLM frame indicator positions of 1<sup>st</sup> to 5<sup>th</sup> set of ICM detecting locations.

TISFIP1 – TISFIP6: Threshold intensity of the 1<sup>st</sup> to 5<sup>th</sup> SLM frame indicator positions.

TIVF: The timestep of the current ICM video frame.

ISFIP1 – ISFIP6: Average intensities at the 1<sup>st</sup> to 5<sup>th</sup> SLM frame indicator positions.

IIDP1 – IIDP6: Intensity values of the 1<sup>st</sup> to 5<sup>th</sup> set of ICM detecting locations.

SICMV1 – SICMV6: 1<sup>st</sup> to 5<sup>th</sup> Sub-videos of the ICM video.

PIDL1 – PIDL72: Total phase angle change at the 1<sup>st</sup> to 72<sup>th</sup> ICM detecting location.

HIDL1 – HIDL72: Estimated cured part height at the 1<sup>st</sup> to 72<sup>th</sup> ICM detecting location.

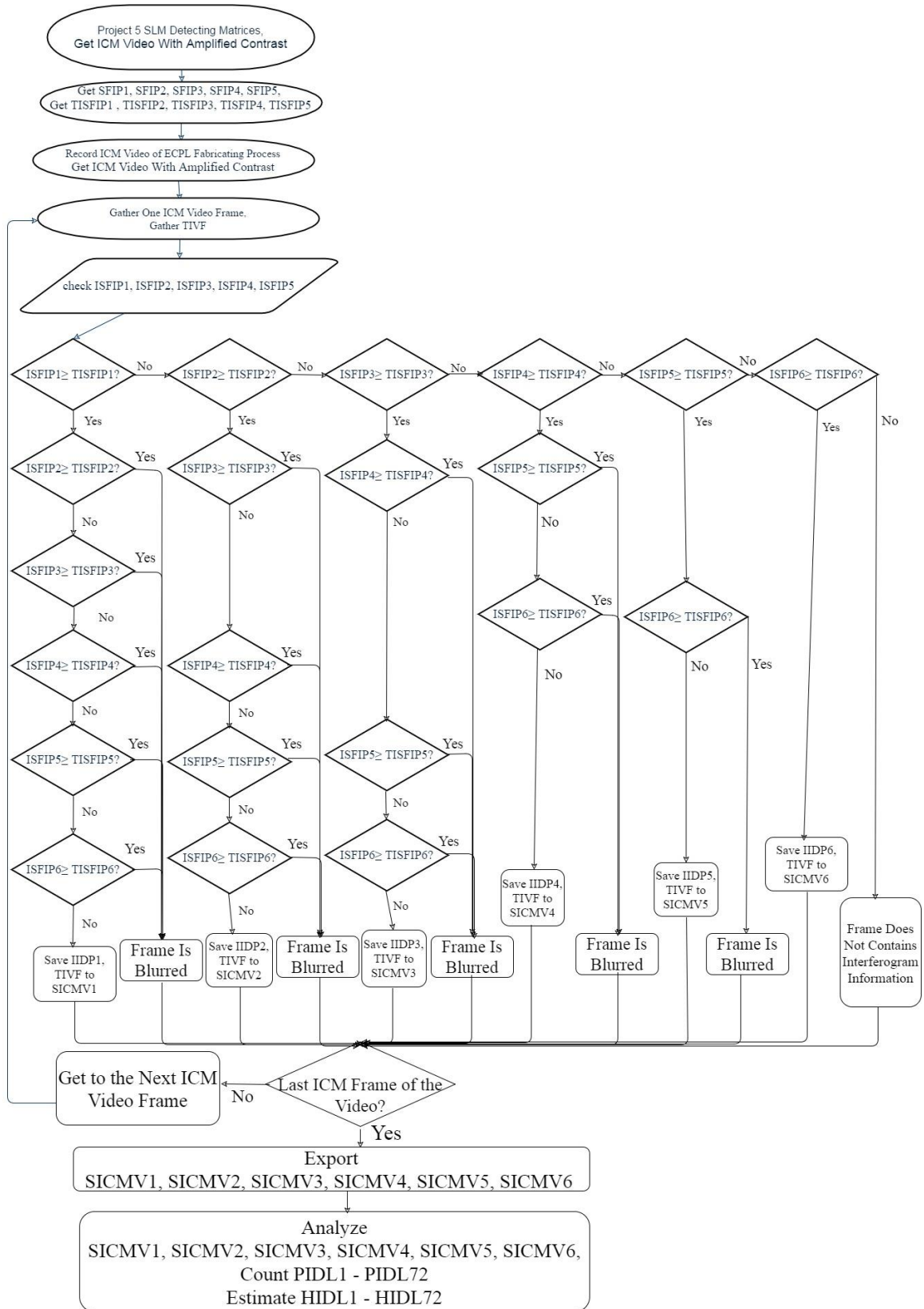


Figure 46. Flow Chart of the ICM Signal Processing Procedure

### **4.3 Chapter Summary**

This chapter presented the improved ECPL and ICM system. The system setup and equipment of the improved ECPL and ICM system were introduced. The improvements in the ICM system with electronic iris was introduced. The ICM system alignment method, the ICM frame identification procedure and the overall signal processing procedure is described. Based on this improved ICM system, the cured part dimensions could be estimated.

## CHAPTER 5. EXPERIMENTAL VALIDATION

In this chapter, two sets of experiments have been done to validate the hypothesis mentioned in Section 2.4. The first set of experiments validates the ICM system's ability to measure the cured part heights with respect to location variance in 1 dimension (in the direction perpendicular to the cured part height). The second set of experiments validates the ability of the time-varying scanning method in increasing the resolution of the ICM. The third set of experiments validates the ability of the ICM to measure the 2D lateral dimensions (perpendicular to the cured part height) of the cured part.

### 5.1 Experimental Validation and Analysis

#### 5.1.1 *Experiment 5.1.1: Using Time-varying ICM Scanning Method to Determine Multiple Heights in One Sample*

To validate the research hypothesis, 7 samples were cured by the ECPL system, and interferograms gathered by the ICM system were used to estimate the cured part height. For each of these 7 samples, the ECPL system firstly used the DMD to project a rectangular curing region, 768 x 350 pixel defined by the DMD, to cure the sample for 20 seconds. Then the curing profile changed to project another rectangular curing region, 384 x 350 pixel defined by the DMD, to continue cure the left half of the part for 23 seconds. Figure 47 shows the curing profile defined on the DMD and the curing time for each curing profile.

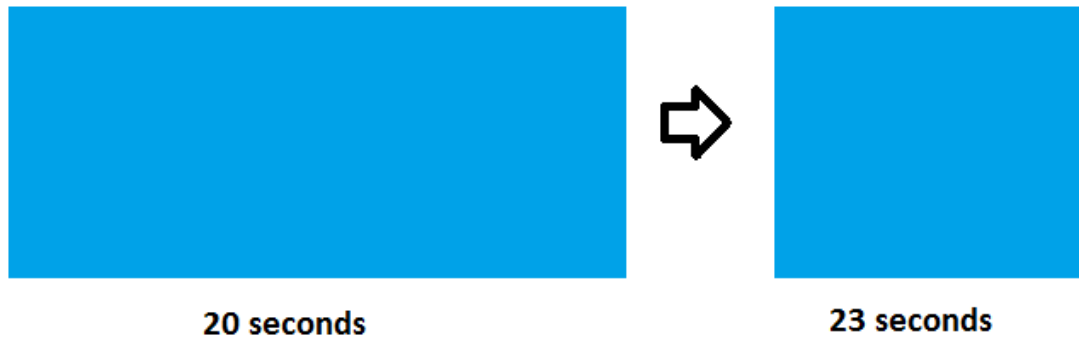


Figure 47. Curing Profiles and Exposure Times Used to Fabricate 8 Samples in Experiment 5.1.1

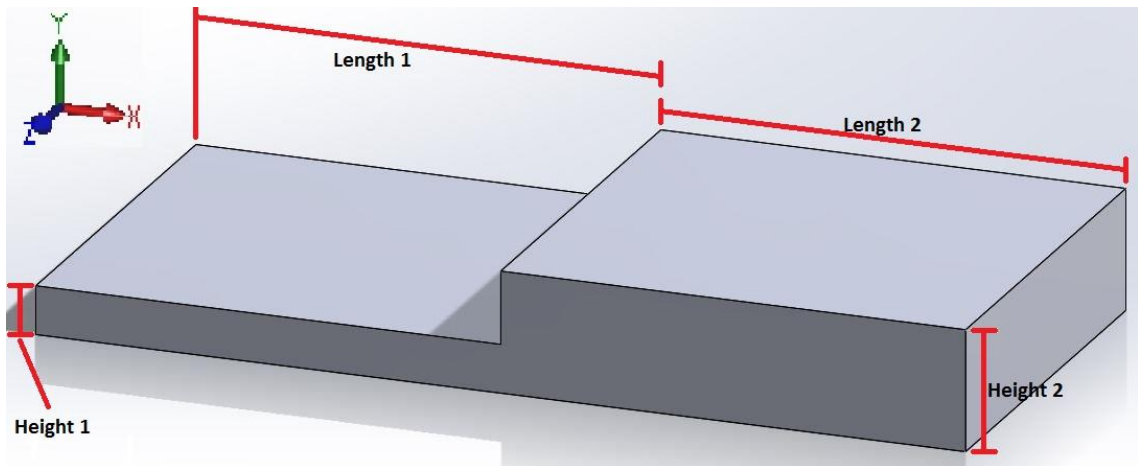


Figure 48. 3D View of the Expected Cured Sample and Measured Parameters in Experiment 5.1.1

Figure 48 shows 3D view of the expected cured sample and the measured parameters in this experiment. After the interferograms were gathered by the ICM system, the height distribution with respect to x direction (refer to the x-axis in Figure 48) was estimated by the ICM system. Confocal microscope was used to gather the height distributions with respect to x direction (refer to the x-axis in Figure 48) of the 7 experiment samples. The

confocal microscope results of the 7 samples were used as a reference to validate the ICM results. Figure 49 to Figure 55 show the height distributions with respect to the x direction of the 7 samples, estimated by the ICM system and measured by the confocal microscope. Note that the impulsive changes in the height distributions measured by the confocal microscope, i.e. the extremely high and low height measurements compared with the ICM-determined height measurements, were due to the limitation of the confocal microscope. These extreme measurements were caused by the relatively low magnification of the confocal microscope when measuring the edges of the fabricated features, and these extreme measurements should be ignored. For these 7 samples, since the ICM-estimated height distributions match the measured height distributions from confocal microscope, the experiments prove that the ICM can accurately measure the dimensions of the cured part. Quantitative descriptions of Height 1 and Height 2 (refer to Figure 48) of the 7 samples, measured by the ICM system and confocal microscope, are listed in Table 2. For each sample, the measurements of Height 1 and Height 2 were made using the average of the heights at the “low-height (but non-zero height)” and “high-height” regions of the 72 measured positions. Standard deviations of these height measurements are also listed in Table 2. Quantitative descriptions of Length 1 and Length 2 (refer to Figure 48) of the 7 samples, measured by the ICM system and confocal microscope, are listed in listed in Table 3. Error between the ICM measurements and the confocal microscope measurements will be listed in Section 5.2.

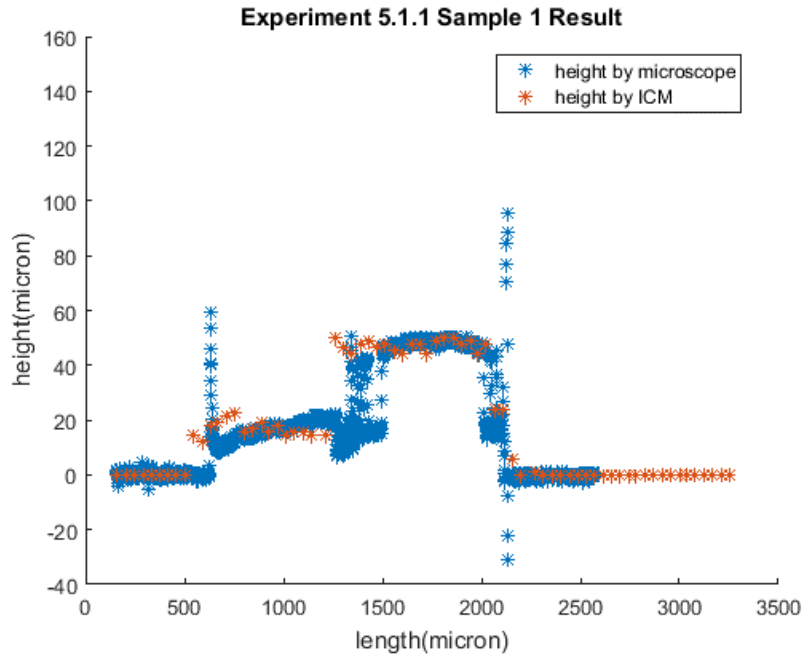


Figure 49. Height Distribution vs Length in X Direction of Sample 1

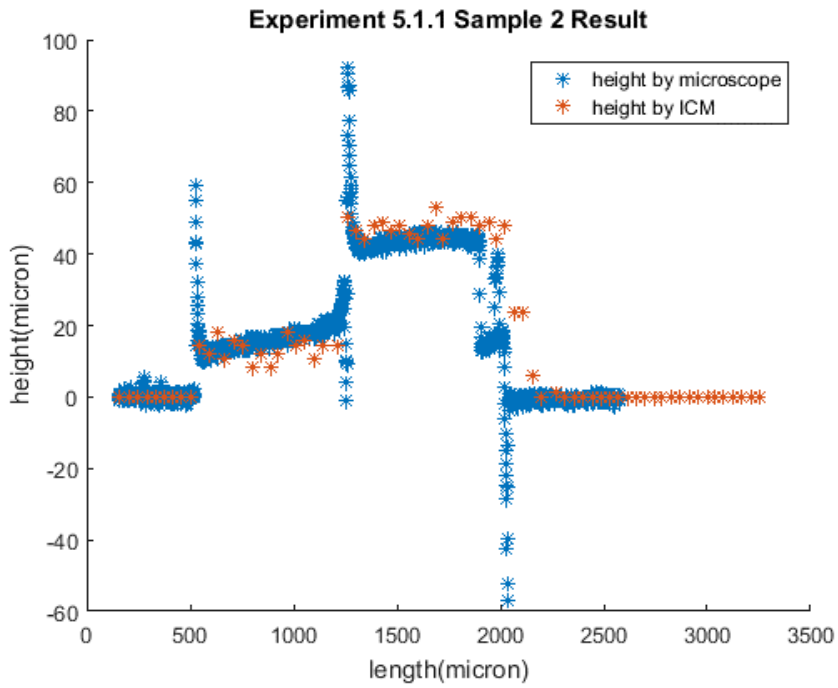


Figure 50. Height Distribution vs Length in X Direction of Sample 2

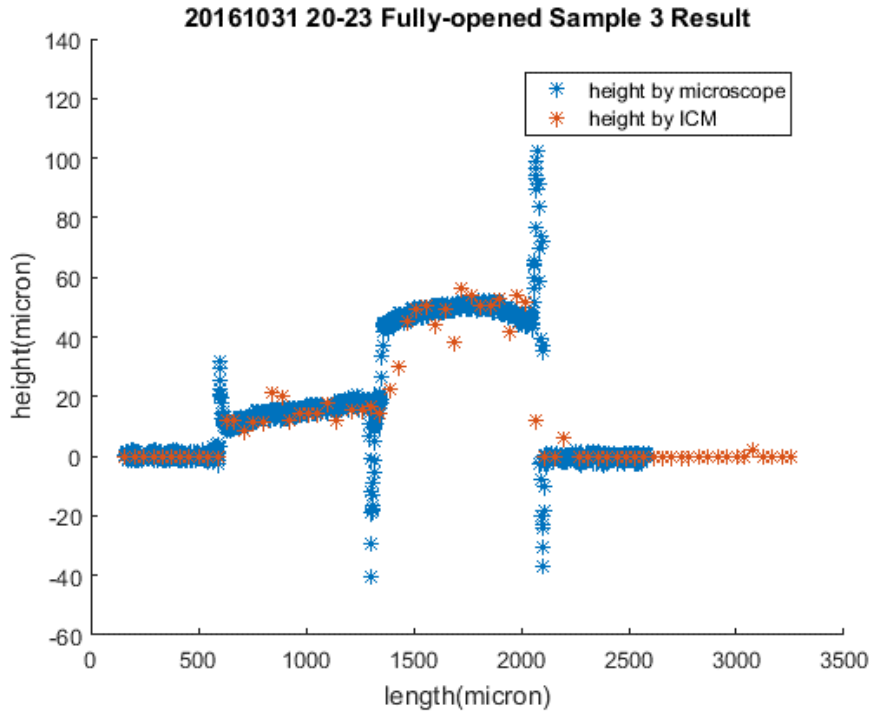


Figure 51. Height Distribution vs Length in X Direction of Sample 3

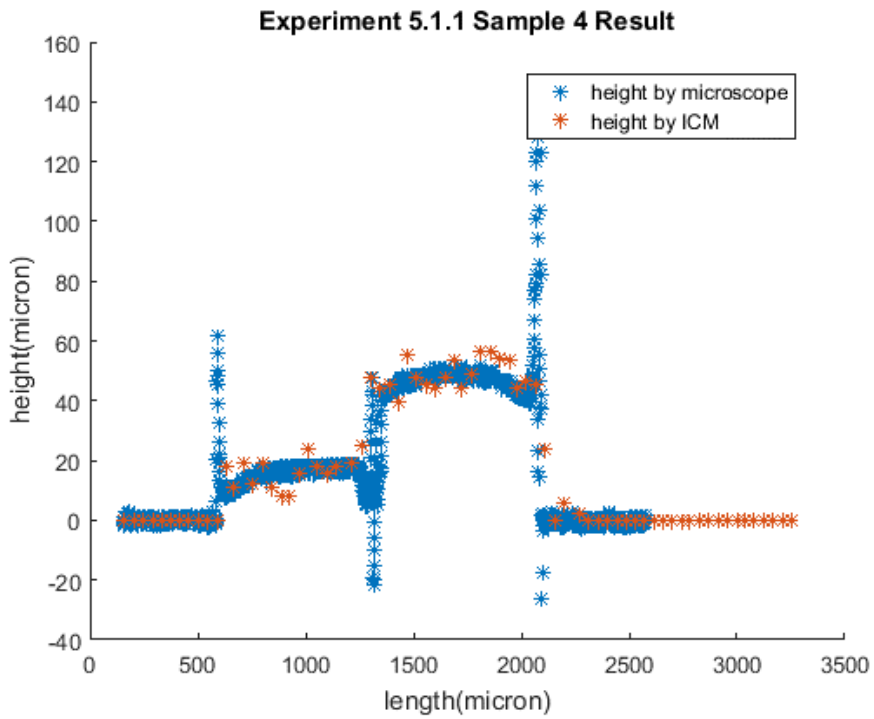


Figure 52. Height Distribution vs Length in X Direction of Sample 4

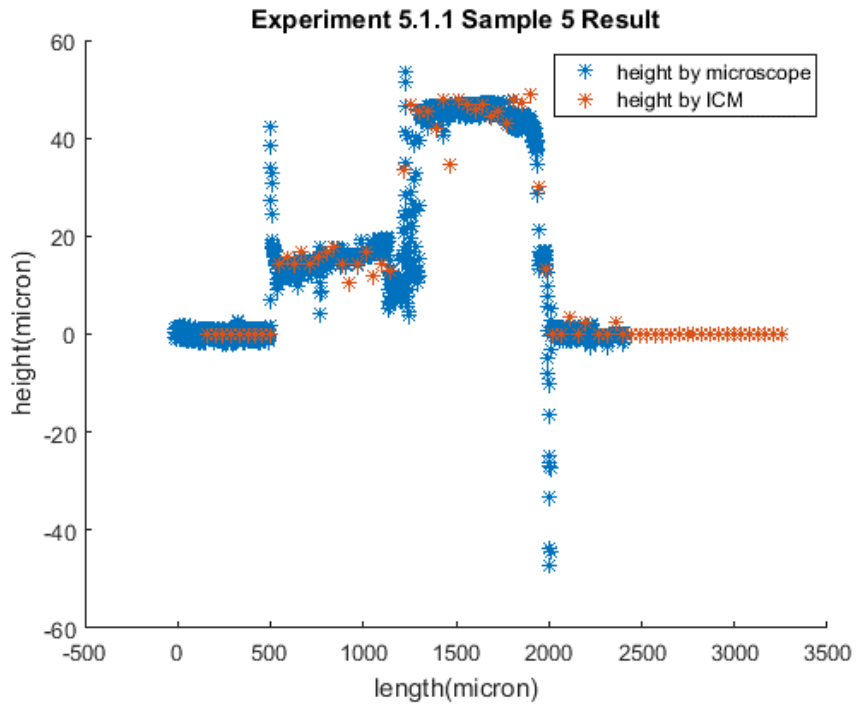


Figure 53. Height Distribution vs Length in X Direction of Sample 5

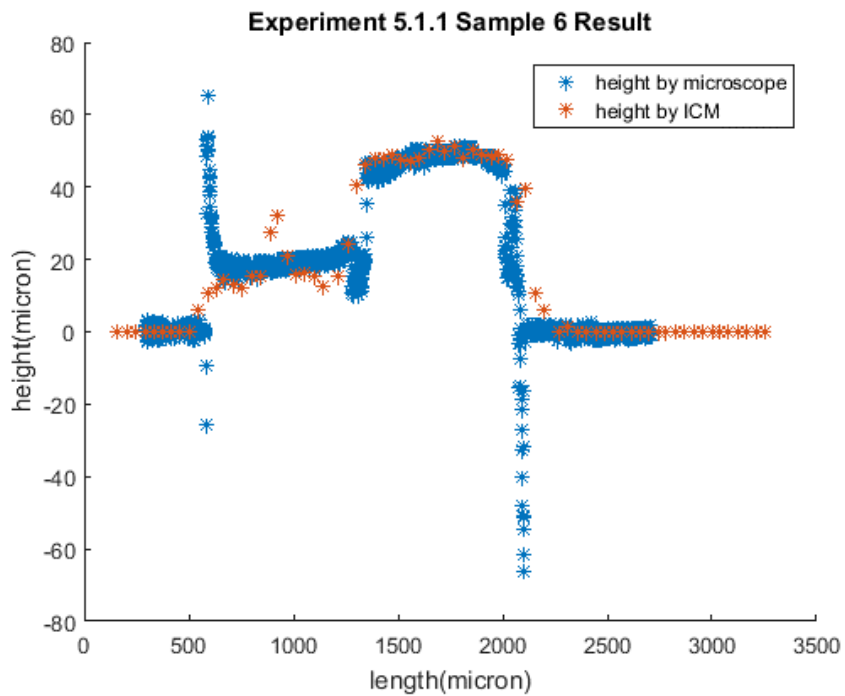


Figure 54. Height Distribution vs Length in X Direction of Sample 6

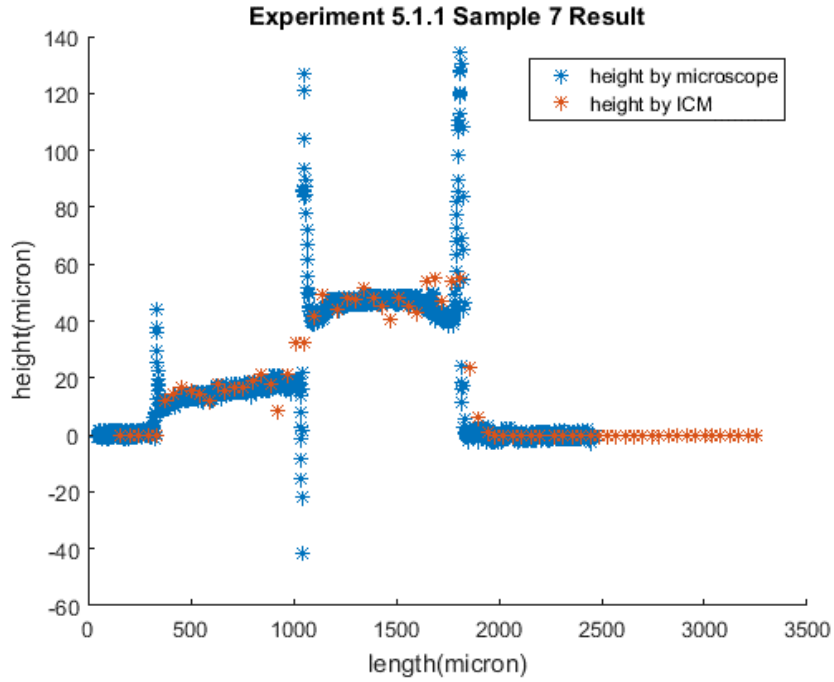


Figure 55. Height Distribution vs Length in X Direction of Sample 7

Table 2. Average Value and Standard Deviation of Height 1 and Height 2 Measured by ICM System and Confocal Microscope

Sample Number	Average Height 1 from ICM $\pm$ Standard Deviation ( $\mu\text{m}$ )	Height 1 from Microscope $\pm$ Standard Deviation ( $\mu\text{m}$ )	Average Height 2 from ICM $\pm$ Standard Deviation ( $\mu\text{m}$ )	Height 2 from Microscope $\pm$ Standard Deviation ( $\mu\text{m}$ )
1.1	$17.7 \pm 2.5$	$16.1 \pm 3.4$	$46.3 \pm 5.5$	$48.5 \pm 7.7$
1.2	$13.3 \pm 2.8$	$14.7 \pm 2.5$	$43.7 \pm 5.7$	$45.0 \pm 4.0$
1.3	$15.6 \pm 5.0$	$15.9 \pm 2.1$	$46.6 \pm 4.8$	$49.6 \pm 2.2$
1.4	$16.1 \pm 4.5$	$17.8 \pm 5.2$	$47.3 \pm 6.9$	$49.3 \pm 4.7$
1.5	$14.7 \pm 1.9$	$14.8 \pm 2.0$	$45.4 \pm 8.8$	$45.9 \pm 5.4$
1.6	$17.1 \pm 5.8$	$19.6 \pm 1.5$	$47.4 \pm 4.0$	$49.0 \pm 2.1$
1.7	$15.2 \pm 2.6$	$16.5 \pm 2.6$	$48.1 \pm 4.4$	$47.3 \pm 4.2$

Table 3. Length 1 and Length 2 Measured by ICM System and Confocal Microscope

Sample Number	Length 1 from ICM ( $\mu\text{m}$ )	Length 2 from ICM ( $\mu\text{m}$ )	Length 1 from Microscope ( $\mu\text{m}$ )	Length 2 from Microscope ( $\mu\text{m}$ )
1.1	712.8	853.6	711.7	820.2
1.2	712.8	897.6	736.0	808.4
1.3	800.8	686.4	761.5	739.0
1.4	668.8	809.6	720.5	787.9
1.5	668.8	765.6	712.2	774.3
1.6	712.8	853.6	766.0	769.2
1.7	677.6	800.8	693.9	815.8

*5.1.2 Experiment 5.1.2: Using Time-varying ICM Scanning Method to Determine 1D Lateral Dimension with High Resolution*

In order to validate the research hypothesis, a series of experiments was performed to demonstrate the capability of the SLM-based ICM system to monitor the lateral extents of a curing part and the part's height distribution in real time. The experiment reported here utilized DMD images of 200x768, 220x768, 230x768, 240x768, 250x768, 260x768, 270x768, 280x768, 290x768, 300x768, 310x768, 320x768, 330x768, 340 x 768 and 350x768 pixels to cure a rectangular part for 24 seconds. The length of the irradiation region was approximately 4200 microns which corresponded to the 768 pixel length defined on DMD), and the width of the irradiation region approximately ranged from 1100 microns to 1900 microns which corresponded to the 200-350 pixel length range defined on the DMD. The interferograms were analyzed, and the total phase shifts at each monitored

positions were recorded. Figure 56 shows the interferograms recorded at sampled points 20, 28, and 30. The interferogram from point 20 had large amplitude oscillations, while at point 30 the interferogram was flat. At point 28 which is close to the edge of the irradiated region, oscillations with much smaller amplitudes were observed.

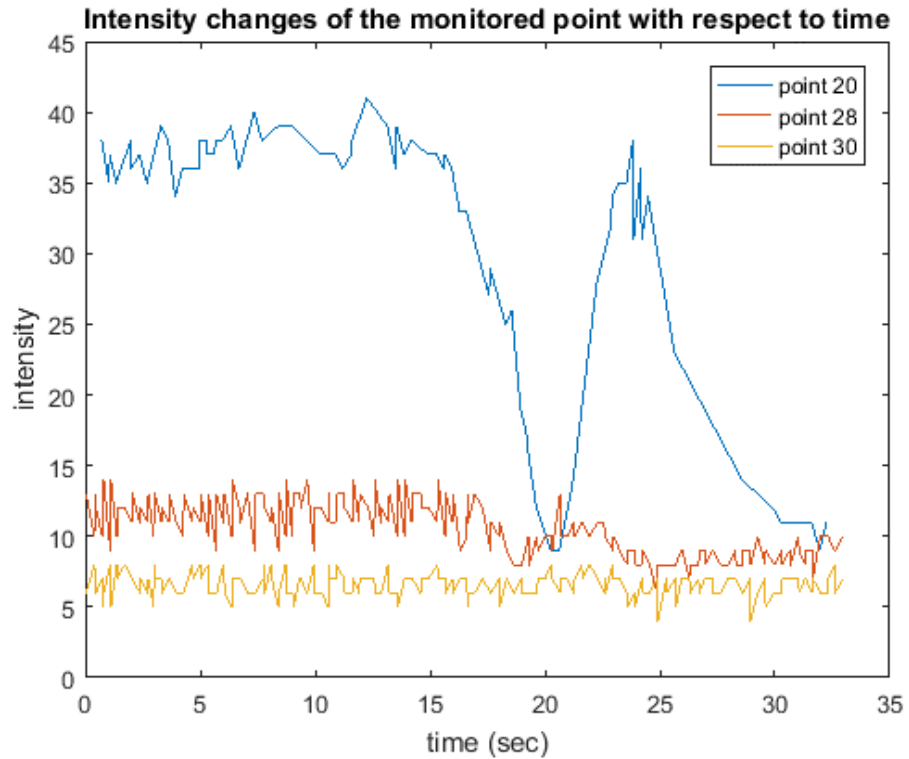


Figure 56. Interferograms at point 20, 28, and 30 [46]

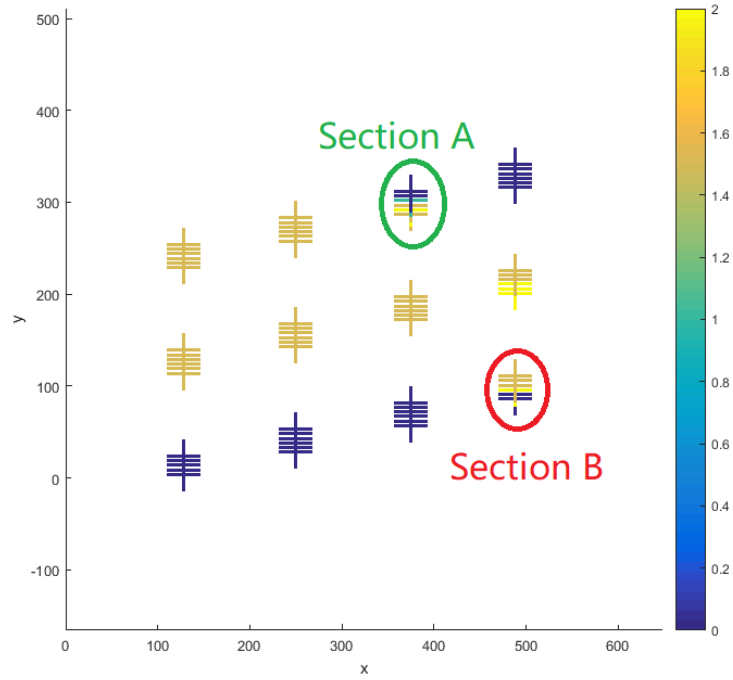


Figure 57. Resultant number of oscillation periods among the monitored points

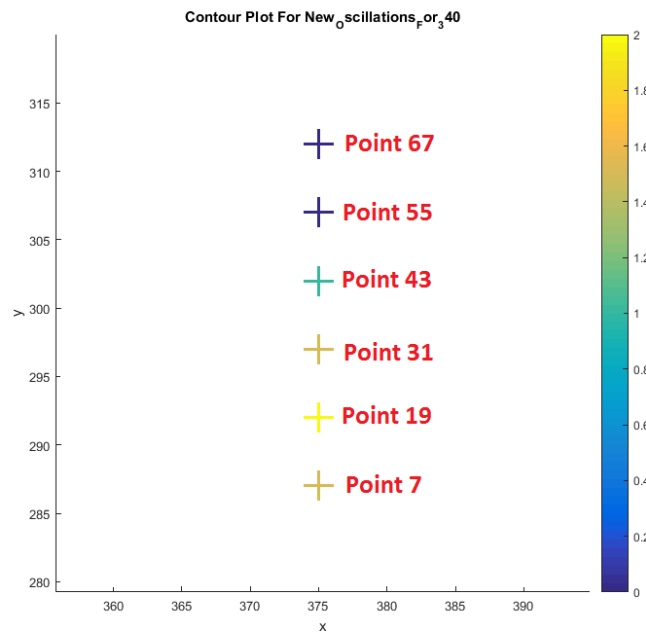


Figure 58. Zoomed-in view of Figure 57 for the section A

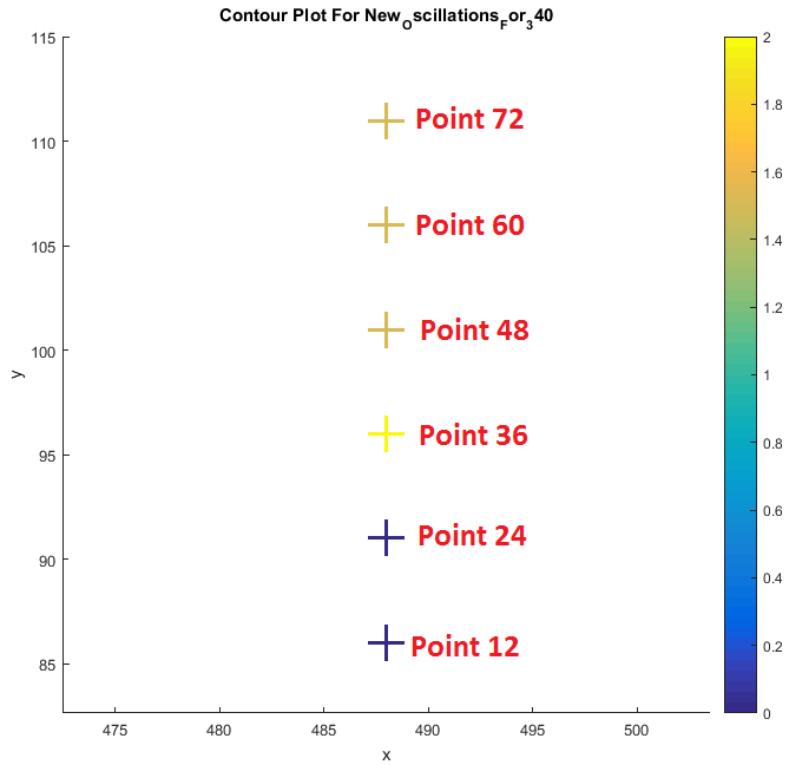


Figure 59. Zoomed-in view of Figure 57 for the section B

As an example, Figure 57 shows the resultant number of intensity oscillation periods at each monitored point for an experiment that used the DMD image of 340 x 768 pixels to cure a rectangular part for 24 seconds. Figure 58 and Figure 59 show the zoomed in view of Figure 57 at section A and B. In Figure 57, the number of oscillations at each ICM detecting position is indicated in a 2D layout where the number of oscillations was indicated by the color bar on the right. Each cross-mark indicates one ICM detecting position. This plot helped determine the 1D vertical dimension (i.e. the width) of the cured part. From Figure 58, since point 43 had 1 oscillation period while point 55 did not have any oscillation period, it could be concluded that the top edge of the curing region was located between point 43 and point 55. Similarly, from Figure 59, point 36 had 2 oscillation

periods while point 24 did not have any oscillation periods, it could be concluded that the bottom edge was between point 36 and point 24. The width of the cured part should be defined by the distance between the top and bottom edges of the curing region.

As mentioned in the last paragraph of Section 4.2, it is assumed that there is no scaling relationship nor distortion between the dimensions determined by the ICM camera and the cured part dimensions in real world in microns. Thus, Equation 13 was used to determine the distance in real world from the pixel distance defined on the ICM video frames:

$$D = 4 * 2.2 * d \quad \text{(Equation 13)}$$

where  $D$  is the distance in the real world in microns,  $d$  is the distance defined on the ICM video frame in pixels. The second factor 2.2 [microns/pixel] was determined from the specifications of the ICM camera which stated that both the horizontal and vertical size of a pixel of the camera was 2.2 micron [48]. The first scaling factor 4 was introduced since the ICM camera used both horizontal and vertical binning factors of 4, i.e. the camera took the average of an array of  $4*4=16$  pixels to form one pixel for the ICM video frames [47]. In this case, the binning function scaled the ICM frame size  $\frac{1}{4}$  time as its original size.

Using Equation 13, it was determined that the vertical width of this cured part was approximately 1857 microns. On the other hand, the measurement from microscope indicated that the width of this cured part was 1863 microns. Table 4 shows more experiment results with different sizes of the irradiation region defined by pixel lengths on the DMD.

Table 4. Estimated and Measured Part Widths

Sample Number	Irradiation Size Defined by DMD pixel length	Width in [ $\mu\text{m}$ ] From ICM	Width in [ $\mu\text{m}$ ] From Microscope
2.1	200x768	1012.0	1075
2.2	210x768	1091.2	1133
2.3	220x768	1091.2	1194
2.4	230x768	1135.2	1248
2.5	240x768	1179.2	1306
2.6	250x768	1267.2	1399
2.7	260x768	1311.2	1425
2.8	270x768	1390.4	1466
2.9	280x768	1412.4	1529
2.10	290x768	1496.0	1583
2.11	300x768	1540.0	1618
2.12	310x768	1641.2	1710
2.13	320x768	1689.6	1767
2.14	330x768	1768.8	1801
2.15	340x768	1856.8	1863
2.16	350x768	1892.0	1920

## 5.2 Error Analysis

Table 5 shows the errors for the ICM measurements of Length 1 and Length 2 in Experiment 5.1.1. Table 6 shows the errors for the ICM measurements of Height 1 and

Height 2 in Experiment 5.1.1. Table 5 shows the errors for the ICM measurements of cured part widths in Experiment 5.1.2. For Table 5, Table 6, and Table 7, the error is defined as Equation 14

$$Error = (ICM) - (Microscope) \quad (\text{Equation 14})$$

The percentage error was calculated using Equation 15

$$Percentage\ Error = \frac{(ICM) - (Microscope)}{(Microscope)} * 100\% \quad (\text{Equation 15})$$

where *(ICM)* stands for the measurement from the ICM system, and *(Microscope)* stands for the measurement from the microscope.

Table 5. Errors and Percentage Errors for the ICM Measurements of Length 1 and Length 2 in Experiment 5.1.1

Sample Number	Error for Length 1 (µm)	Error for Length 2 (µm)	Percentage Error for Length 1	Percentage Error for Length 2
1.1	1.1	33.4	0.2%	4.1%
1.2	-23.2	89.2	-3.2%	11.0%
1.3	39.3	-52.6	5.2%	-7.1%
1.4	-51.7	21.7	-7.2%	2.8%
1.5	-43.4	-8.7	-6.1%	-1.1%
1.6	-53.2	84.4	-6.9%	11.0%
1.7	-16.3	-15.0	-2.3%	-1.8%

Table 6. Errors and Percentage Errors for the ICM Measurements of Height 1 and Height 2 in Experiment 5.1.1

Sample Number	Error for Height 1 ( $\mu\text{m}$ )	Error for Height 2 ( $\mu\text{m}$ )	Percentage Error for Height 1	Percentage Error for Height 2
1.1	1.6	-2.2	9.9%	-4.5%
1.2	-1.4	-1.3	-9.3%	-2.9%
1.3	-0.3	-3.0	-1.8%	-5.9%
1.4	-1.7	-2.0	-9.3%	-4.1%
1.5	-0.1	-0.5	-0.5%	-1.0%
1.6	-2.5	-1.6	-12.7%	-3.3%
1.7	-1.3	0.8	-8.0%	1.7%

Table 7. Errors and Percentage Errors for the ICM Measurements of Cured Part Widths  
in Experiment 5.1.2

Sample Number	Irradiation Size Defined by DMD Pixel Length	Error in [ $\mu\text{m}$ ]	Percentage Error in %
2.1	200x768	-63.0	-6%
2.2	210x768	-41.8	-4%
2.3	220x768	-102.6	-9%
2.4	230x768	-112.5	-9%
2.5	240x768	-126.8	-10%
2.6	250x768	-131.7	-9%
2.7	260x768	-113.8	-8%
2.8	270x768	-75.6	-5%
2.9	280x768	-116.9	-8%
2.10	290x768	-87.5	-6%
2.11	300x768	-78.0	-5%
2.12	310x768	-68.8	-4%
2.13	320x768	-77.4	-4%
2.14	330x768	-31.8	-2%
2.15	340x768	-6.2	0%
2.16	350x768	-28.0	-1%

According to Zhao, X. et al. [42], the ICM system resolution for height measurement can be calculated using Equation 16

$$\text{Height Resolution} = \frac{dz}{d\phi} * (MTI * IF) \quad (\text{Equation 16})$$

where  $\frac{dz}{d\phi}$  in the experiments for this thesis is 11.982  $\mu\text{m}$ , *MTI* stands for the measurement time interval in second and is 2 seconds in the experiments, *IF* is the maximum frequency occurred in the intensity oscillation in the ICM-gathered interferograms. *IF* is 0.13 Hz in the experiments for this study. Thus, the resolution for the height measurements of ICM in this study is

$$\text{Height Resolution} = 11.982 * (2 * 0.13) \cong 3.12 \mu\text{m}$$

Comparing Table 6 with the ICM resolution for height measurements, all the errors fall within the resolution, indicating that the ICM system is able to accurately measure the cured part height. This validates the research hypothesis in Section 2.4. On the other hand, both the theoretical resolution in height measurement and the errors for height measurements in Experiment 5.1.1 were worse than the original ICM system presented by Zhao X. et al. [51]. The theoretical height resolution of the original ICM system proposed by Zhao X. et al. was 2  $\mu\text{m}$  [51]. This is due to the fact that the Time-Varying Scanning Method introduced in the improved ICM system introduces time-variance for the measurements. Since the measuring positions are measured at different time steps, the sampling frequency for the improved ICM system with Time-Varying Scanning method is lower than that used in the original ICM system. In the validation experiments, since there was a sequence of six measuring position sets, the sampling frequency of the improved ICM system was 1/6 of the sampling frequency of the original ICM system. The Time-Varying Scanning method compromises the sampling frequency to achieve better lateral resolution.

As mentioned in the last paragraph of Section 4.1, the ICM system resolution for length and width measurements should be  $44\ \mu\text{m}$ . Comparing Table 5 and Table 7 with the ICM system resolution in lateral dimensions measurement, part of the errors exceeds the ICM system resolution.

Five reasons could explain the discrepancy between the ICM measurements and the microscope measurements in lateral dimension. Firstly, this error consisted of the theoretical resolution of the ICM measurement which was  $\pm 44\ \mu\text{m}$ . Secondly, the deviations of the results could come from the errors of the microscope measurement. When defining the edges of the cured part on the microscope, there could be a manual error of  $\pm 15\ \mu\text{m}$ . Thirdly, the edges of the fabricated parts were not walls that were perfectly perpendicular to the substrate glass slides, but some slanted walls. This caused the height distribution at the slanted edges to be a transition from the desired height of the fabricated part to zero in height, which made the edge fuzzy to be observed by the ICM. This fuzzy edge zone could contribute to  $\pm 10\ \mu\text{m}$  to the deviation between the ICM measurements and the microscope measurement. In addition, within the fuzzy boundary at the slanted edges of cured samples, the height gradually grows from  $0\ \mu\text{m}$  at the furthest position (away from the center of the cured sample) to the “desired” height at the nearest position of the fuzzy boundary to the center of cured sample. Due to the limitation of ICM resolution in height measurement, only the inner part of the fuzzy boundary (which has height closer to the desired height) could be recognized by the ICM system. Compared with microscope measurements which could recognize all the fuzzy boundary zone, the width detected by the ICM system will be smaller than the width measurements taken by microscope. This explains why all the ICM width measurements were smaller than the corresponding

measurements taken by the microscope. Fourthly, imperceptible damage during the washing process could be an explanation for the error between the ICM measurements and the microscope measurements. These damage could contribute to an error of  $\pm 20 \mu\text{m}$ . Fifthly, during the alignment procedure mentioned in Section 4.2.1, the alignment of the optical path for the ICM system could add errors to the ICM measurements. The misalignment of the optical path of the ICM laser beams, after being reflected by the bottom substrate of the resin chamber, could contribute to a deviation of  $\pm 50 \mu\text{m}$ . Table 8 summarizes these 5 sources of error and categorizes these error sources as either system error or experimental error.

Table 8. Allowable Error Sources and Corresponding Error Contributions for ICM Edge Detection

Error Category	Source of Error	Error Contribution ( $\mu\text{m}$ )	Total Error Contribution ( $\mu\text{m}$ )
System Error	ICM Resolution	$\pm 44$	$\pm 54$
	Fuzzy Edge Zone to be Detected by ICM	$\pm 10$	
Experimental Error	Defining Edge on Microscope	$\pm 15$	$\pm 85$
	ICM System Misalignment	$\pm 50$	
	Washing Damage	$\pm 20$	
Total Error Allowable ( $\mu\text{m}$ )			$\pm 139$

As shown in Table 8, the total possible discrepancy can be  $\pm 139 \mu\text{m}$  between width measurements from the ICM system and from microscope. Comparing the total possible error to the errors listed in Table 5 and Table 7, all the errors are within the total possible error. However, the total  $\pm 139 \mu\text{m}$  possible error is not good enough to accurately measure the lateral dimensions of the features fabricated by the ECPL system. As shown in Table 8, the inherent system error of the ICM system was  $\pm 54 \mu\text{m}$ , and the experimental error which could be improved was  $\pm 85 \mu\text{m}$ . Thus, the large measurement errors shown in Table 7 might be due to the experimental error, and the ICM system's true ability in measurement accuracy in lateral dimension could be better than the large errors shown in Table 7.

Without changing the ICM system equipment, there are five possible improvements for the ICM system to improve the lateral dimension accuracy and to reduce discrepancy between ICM width measurements and corresponding microscope width measurements. Firstly, the current ICM camera utilizes a binning function of 4, which limited the theoretical resolution of the ICM system to  $44 \mu\text{m}$  [47]. If the binning function is set to 1, the resolution of the ICM camera will be improved, and the theoretical resolution of the ICM system could be improved to  $36 \mu\text{m}$  which is the resolution of the SLM [44]. Secondly, the system error due to the aforementioned fuzzy edge could also be reduced to  $\pm 3 \mu\text{m}$ . Thirdly, the alignment of the optical path could be further improved to reduce the experimental error contribution to be less than  $\pm 5 \mu\text{m}$ . Fourthly, with higher magnification factor to be used when measuring the fabricated features using the confocal microscope, this experimental error could be further reduced to less than  $\pm 2 \mu\text{m}$ . Lastly, washing process could be improved to reduce the experimental error contribution to be less than  $\pm 3 \mu\text{m}$ . With these possible improvements, the total inherent ICM system error could be  $\pm 39$

$\mu\text{m}$ . The total allowable experimental error could be reduced to  $\pm 10 \mu\text{m}$ . Thus, the lateral resolution of the improved ICM system in this thesis study would could be improved as  $\pm 39 \mu\text{m}$ , and the maximum allowable error of lateral dimension measurements with such improved ICM system could be  $\pm 49 \mu\text{m}$ . If  $\pm 5\%$  measurement accuracy is a good requirement for the ICM system's ability in monitoring the ECPL fabrication process, the ICM system, with the aforementioned improvements, should be able to accurately monitor the ECPL fabrication process with feature size larger than  $780 \times 780 \mu\text{m}$  in its lateral dimensions.

For discrepancy of height measurements, as mentioned in page 100, the theoretical height measurement resolution for the improved ICM system is  $3.12 \mu\text{m}$ . In addition, the microscope measurement could contribute to a discrepancy of  $\pm 8 \mu\text{m}$ . Thirdly, the top surface of fabricated samples were not homogeneously flat, and the surface roughness could add up to an error of  $\pm 8 \mu\text{m}$ . Lastly, the damage of the top surface of fabricated samples, during the washing process, could add up to an error of  $\pm 3 \mu\text{m}$ . Table 9 summarizes these 4 sources of error and categorizes these error sources as either system error or experimental error.

Table 9. Allowable Error Sources and Corresponding Error Contributions for ICM Height Measurements

Error Category	Error source	Error Contribution ( $\mu\text{m}$ )	Total Error Contribution ( $\mu\text{m}$ )
System Error	ICM Resolution	$\pm 3.12$	$\pm 3.12$
Experimental Error	Microscope Measurement Error	$\pm 8$	$\pm 19$
	Surface Roughness of Sample	$\pm 8$	
	Washing Damage	$\pm 3$	
Total Allowable Error ( $\mu\text{m}$ )			$\pm 22.12$

Thus, as shown in Table 9, the inherent system error for ICM height measurement is  $\pm 3.12 \mu\text{m}$ , and the experimental error for height measurements in the validation experiments was  $\pm 19 \mu\text{m}$ . The total allowable error for height measurements was  $\pm 22.12 \mu\text{m}$ . The maximum observed total error for height measurements, which is the maximum value among the summations of the observed error from Table 5 plus the corresponding measurement standard deviations (from both the ICM measurement and the corresponding microscope measurement) from Table 2 for each measured sample, was  $\pm 15.4 \mu\text{m}$  (Height 2 measurement of Sample 1.1). Since the maximum observed total error is within the total allowable error, the height measurement results in Experiment 5.1.1 validates the research hypothesis. In addition, the large deviations between the ICM measured part height and the microscope measurements, compared with the theoretical resolution of the ICM system presented in this thesis ( $\pm 3.12 \mu\text{m}$ ), might be due to the large experimental error shown in Table 9. If 5% measurement accuracy is an adequate requirement, the practical usage of

the ICM system presented in this thesis is to measure cured part height that is larger than  $63\ \mu\text{m}$ , and the building speed of the part in vertical dimension should be less than  $1.55\ \mu\text{m}/\text{second}$ , refer to Equation 16. As for improvements of ICM height measurements, the resolution in the vertical direction could be improved if the ICM camera could be improved to have higher sampling frequency.

As a summary, the practical usage of the ICM system presented in this thesis, is to accurately measure the ECPL fabrication process for building rectangular cuboids with lateral dimensions larger than  $780 \times 780\ \mu\text{m}$  and height larger than  $63\ \mu\text{m}$  and the building speed in the vertical dimension no more than  $1.55\ \mu\text{m}/\text{second}$ . This measurement capability is not good enough for practical usage, as the current ICM system presented in this thesis could monitor the ECPL fabrication processes with no less than 40.6 second for the fabrication duration, based on the  $63\ \mu\text{m}$  minimum height and  $1.55\ \mu\text{m}/\text{second}$  maximum building speed requirements. If the lateral resolution could reach up to  $\pm 10\ \mu\text{m}$ , and if the resolution for height measurement could remain below  $\pm 5\ \mu\text{m}$  with maximum building speed (in the direction of height) up to  $5\ \mu\text{m}/\text{second}$ , the ICM system should be good for practical usage. To achieve this objective, the resolution of the SLM should be improved, and a new ICM camera with higher sampling frequency is required.

Compared with the alternative ICM system developed by Zhao X. et al. [51], the ICM system presented in this thesis features worse dimension measurement resolutions. The proposed lateral resolution of the old ICM system by Zhao X. et al. [51] was  $8.8\ \mu\text{m}$ , and the discrepancy between width from ICM and width from microscope was  $30\ \mu\text{m}$ . These proposed values are even better than the highest possible lateral resolution the ICM

system presented in this thesis could achieve. The reason is that the alternative ICM system developed by Zhao X. et al. [51] intends to analyze the interferograms at all the pixels of the ICM video, whereas the ICM system presented in this thesis only analyze the interferograms every 5 pixels in lateral dimensions. However, the lateral resolution proposed by Zhao X. et al. [51] does not have any validation experiments. The proposed resolution in the direction of height by the alternative ICM system proposed by Zhao X. et al. [51] is 2  $\mu\text{m}$  with the building speed of 5.991  $\mu\text{m}/\text{second}$  in the direction of height, which is also better than the ICM system presented in this thesis. This is due to the lower sampling frequency of the ICM camera used in the ICM system presented in the ICM system presented in this thesis. Since the Time-varying Scanning Method utilized in this thesis periodically measures six sets of lateral positions at different time steps, the resulting sampling frequency of the recorded ICM interferogram (for each detecting location) used in the ICM system in this thesis is 1/6 of the sampling frequency of that used in the alternative ICM system developed by Zhao X. et al. [51]. This lower sampling frequency results in lower resolution capability (in the direction of height) of the ICM system developed in this thesis. The ICM system developed in this thesis has higher requirement in ICM camera sampling frequency than the alternative ICM system developed by Zhao X. et al. [51].

One inherent problem with the alternative ICM system developed by Zhao X. et al. [51] is that since this alternative ICM system uses a single large beam to cover the whole curing region and analyzes the interferograms at all the pixel locations (which these pixels continuously locate next to each other) within the interested region, the noise signal depicted in Figure 24 could deteriorate the original signals that contain the interferogram

at the interested locations. Zhao X. et al. [51] proposed 3 solutions, during the data decoding and analyzing period, to cancel these noise signals for their alternative ICM system. Firstly, when the alternative system (developed by Zhao X. et al. [51]) gather the interferograms from the recorded ICM video, the intensity at each time step at each interested location is the intensity (at that time step) that averaged from intensities of a  $3 \times 3 = 9$  locations which centered at the interested location [51]. Secondly, for these  $3 \times 3$  locations, Zhao X. et al. [51] gathers the range of the intensities at each time step. For each time step, if the range is larger than an empirically-determined value, the intensity at that time step at that location is inferred as affected by noise and will not be counted into the phase change calculation. Thirdly, Zhao X. et al. proposed thresholds on range and standard deviation of the intensity set within each time interval  $I_M(t_i \sim t_{i+1})$ : if either (or both) the range or standard deviation of the intensities from the interferogram within each time interval  $I_M(t_i \sim t_{i+1})$  is larger than the empirically-determined maximum allowable range or standard deviation, the interferogram at that time interval  $I_M(t_i \sim t_{i+1})$  is inferred to be affected by noise, and the total phase change within this noise-affected time interval will not be counted into the total phase change calculation. By these 3 noise-canceling solutions, the measurement accuracy of the alternative ICM system developed by Zhao X. et al. [51] is guaranteed.

Compared with the alternative ICM system developed by Zhao X. et al. [51], the new ICM system presented in this thesis does not require as much noise-cancellation techniques as that in the alternative system developed by Zhao X. et al., since the isolated beams of ICM laser used in the new ICM system and the discrete locations (which are not

continuously next to each other) analyzed by the new ICM system are inherently less affected by the noise generated by international reflections described by Figure 20.

As a summary, Table 10 describes different characteristics of the new ICM system developed in this thesis and the alternative ICM system developed by Zhao X. et al. [51].

Table 10. Comparison Between the New ICM System Developed in This Thesis and the Alternative ICM System Developed by Zhao X. et al. [51]

Attribute Type	New ICM System Presented in This Thesis	Alternative ICM System Developed by Zhao X. et al [51]
ICM Scanning Laser	Multiple isolated small laser beams	Single laser beam with large cross-section radius
	Laser beam moves sequentially with respect to time	Stable laser beam
ICM Detecting Location	Isolated locations	Continuous locations one next to another
ICM Detecting Region (Lateral)	3176.8 * 2974.4 $\mu\text{m}$	5684.8 * 4259.2 $\mu\text{m}$
Proposed Lateral Resolution (Lateral)	36 $\mu\text{m}$	8.8 $\mu\text{m}$
Proposed Height Resolution	3.12 $\mu\text{m}$ with building speed 1.55 $\mu\text{m}/\text{sec}$ in height	2 $\mu\text{m}$ with building speed 5.991 $\mu\text{m}/\text{sec}$ in height
Advantage	<ul style="list-style-type: none"> <li>• Less affected by noise signal from internal reflection</li> <li>• Less requirement on software-based noise cancellation</li> </ul>	<ul style="list-style-type: none"> <li>• Require Lower Sampling Frequency</li> <li>• Simpler System Setup</li> <li>• Higher height resolution</li> </ul>
Disadvantage	<ul style="list-style-type: none"> <li>• Require Additional SLM System</li> <li>• Require Higher Sampling Frequency</li> <li>• Lower height resolution</li> </ul>	<ul style="list-style-type: none"> <li>• Easier to be Affected by Internal Reflection Noise</li> <li>• Require additional Noise Cancellation</li> </ul>

### 5.3 Limitations

There are four major limitations existing for the ICM system. Firstly, the robustness of the ICM system can be improved. The ICM system, as an optical system, is very sensitive to the alignment of its optical paths. However, for the current ICM system used in this study, since the beam expander, the SLM, and the spatial filter are constrained to the system using cylinder posts, these equipment are vulnerable to minor changes in their angular position with respect to z axis (refer to Z axis in Figure 30). If the angular position of any equipment of the ICM system is off, the misaligned laser paths in the ICM system will cause large error in the lateral dimension measurements of the cured part. However, this limitation could be reduced if the constrains for the components' alignments in the ICM system are improved. Better alignment equipment and more efficient alignment will also improve the performance of the ICM system.

Secondly, as mentioned in Section 2.3, the ICM signal could be affected by the internal interference of large laser beams. The ability to reduce the size of the laser beams is limited by the resolution of the SLM. Thus, to improve the ICM resolution in lateral dimensions measurements, the SLM system with better resolutions is needed.

Thirdly, the sensitivity of the ICM system to the background fringes is a limitation to the system. Due to the inherent interferential patterns of the resin chamber, there exist continuous dark-and-bright background fringes, captured by the ICM video frames, even if there is no curing happened. If any of the SLM frame indicators, mentioned in Section 4.2.2, falls within the dark zone of the background fringes, the ICM system could not detect that ICM indicator, and the ICM video frames, containing the associated set of the ICM

measurement locations (mentioned in Section 4.2.2), cannot be gathered by the detecting frame identification procedure mentioned in Section 4.2.2. As a result, the interferograms at that set of the ICM measurement locations cannot be gathered, the ICM system will not work at those ICM measurement locations, and the ICM resolution in lateral dimension measurements will be deteriorated.

Lastly, the efficiency of height measurement of the ICM system is limited when using the time-varying scanning method, and this limitation requires additional upgrade for the ICM camera than the traditional ICM methods which all the locations are measured at the same time. Since the time-varying scanning method of the ICM system measures different locations at different times, the measuring frequency at each location is reduced, compared with the original ICM methods which all the locations are measured at the same time. This reduces the  $MTI$  mentioned in Equation 15, and the ICM system resolution of height measurements will be reduced. The more sets of ICM measurement locations people want for the ICM system, the more SLM detecting matrix sets (mentioned in Section 4.2.2) the ICM system is needed, the less the parameter  $MTI$  will be, and the less height measurement resolution the ICM will have. One solution to this limitation is to get better ICM camera which the measuring frequency is high. However, this adds additional cost to the ICM system.

## **5.4 Chapter Summary**

This chapter presented the experimental validation for the research hypothesis. Both the height and the 1D lateral dimension has been determined by the ICM system. The ICM system measurements shows adequate accuracy in measuring these dimensions that the

percentage errors of all the measured dimension were within 15%. The ICM system resolution in height and width measurements were introduced. The error sources for the ICM system measurements were discussed which explains why the errors in some measurements exceeded the theoretical resolution. The hypothesis was validated since the errors of all the ICM measurements fell within the total possible error allowed. The limitation of the ICM system was discussed. The ICM system presented in this thesis was compared with the alternative ICM system developed by Zhao X. et al. [51] for their characteristics, advantages, and disadvantages. To further improve the ICM system, better alignment and an ICM camera with higher recording frequency should be expected. With improvements in both the ECPL process and the ICM monitoring process, the percentage errors of the measured dimension could be less than 7.5%. The theoretical resolution could be up to  $\pm 36 \mu\text{m}$ , which is less than 4% percentage error.

## **CHAPTER 6. CLOSURE AND RECOMMENDATIONS**

This chapter summarizes the concepts and findings through the entire document. In Section 6.1, a summary of the thesis will be conducted to get an overall understanding of the research. In Section 6.2, the research question and the hypothesis will be restated and evaluated. In Section 6.3, the contribution of this thesis study will be addressed. In Section 6.4, future work will be discussed and suggested.

### **6.1 Summary of the Thesis**

Overall, the objective of this thesis is to develop an in-situ monitoring system that is capable for measuring the lateral dimension and the height distribution of the features fabricated by the ECPL process. Compared with the monitoring systems mentioned in the literature, the goal of this alternative monitoring method is to accurately measure the dimensions of ECPL fabricated features in three dimensions and keep the system setup to be simple. In this thesis study, the background of the ECPL and ICM system was comprehensively discussed in CHAPTER 1 and CHAPTER 2. Basic introduction for Mask Projection Micro-stereolithography process and commercial applications were presented in CHAPTER 1. Basic principles and applications of interferometer was introduced in CHAPTER 1. The role of ICM system during the ECPL fabrication process was presented. The research motivation was presented.

In CHAPTER 2, existing process planning method and photopolymerization model was introduced. Existing process monitoring methods for additive manufacturing methods were presented. The advantages and disadvantages for each monitoring methods and their

suitability to the ECPL process were discussed. The fundamentals of the ICM system were introduced in CHAPTER 2. Previous work for the ICM system has been introduced and discussed. Optical model for the ICM laser path was presented in CHAPTER 2, which forms the fundamentals for the signal decoding algorithm for the ICM system used in this thesis study. The research question and hypothesis has been illustrated in CHAPTER 2.

CHAPTER 3 and CHAPTER 4 presented the ECPL and ICM system setup in details. In CHAPTER 3, the original ECPL and ICM system were introduced for further comparison. The detailed procedure for ECPL fabrication process was introduced in CHAPTER 3, and the fabricated micro-features used in this thesis study were presented. In CHAPTER 4, the improved ICM system setup was presented in details and compared with the original ICM system. The necessity of implementing aspheric lenses (instead of regular convex lenses) to enhance laser collimation was discussed. The time-varying scanning method developed in this thesis study was presented in CHAPTER 4. Proper ICM camera settings were discussed. The ICM video frame identification procedure was presented. The flow chart indicating how the time-varying scanning method proceeds to estimate cured part dimensions was presented in CHAPTER 4.

In CHAPTER 5, the validation experiments were presented. The experiment procedure and results were presented, and the measurement errors were analyzed and discussed. The experimental results shows that all the dimension measurements done by the improved ICM system had percentage error less than 15%, and this validated the ability of the improved ICM system in measuring both heights and lateral dimension of the features fabricated by the ECPL process. The ICM system presented in this thesis was compared with the alternative ICM system developed by Zhao X. et al. [51] for their

characteristics, advantages, and disadvantages. The limitations of the improved ICM system with time-varying scanning method was discussed. Further improvements in the ICM system was discussed. The improved ICM system developed in this thesis shows its ability in measuring the dimensions of the transparent parts fabricated by the ECPL process, and this ICM system is able to be used to measure the dimensions of features, in transparent in color and in micro-scale, fabricated by other stereolithographic processes.

## **6.2 Evaluation of Hypothesis**

This section provides evaluation of the research question and hypothesis. The objective of this research, aforementioned at the beginning of the paper, is listed as follows:

*To develop the ICM monitoring system that is capable for measuring the lateral dimensions and the height distribution at different lateral locations of the transparent parts fabricated by the ECPL process.*

To accomplish this research objective, the research question was identified, and the hypothesis was formed. The validation of the hypothesis is discussed as follows:

**Research Question: How to modify the ICM system to accurately measure the dimensions of the cured part fabricated by the ECPL system?**

**Hypothesis:** The dimension measurements of the cured part can be done by using isolated laser beams with small cross-section profiles to cover the interested area. By measuring neighboring positions that are too close to each other at different time steps, the resolution in lateral dimension could be improved.

**Explanation:** The existing literatures shows ICM's ability in determining the height of a flat cured part. The ICM utilizes laser beams to radiate the interested positions and gather the interferograms at these locations to estimate the cured part height at these positions. However, the literature [24] shows that the lateral dimension detection was largely influenced by noise signals caused by internal reflections. Isolated laser beams are introduced into the ICM system in order to reduce these noise signals. By using laser beams which are isolated with each other and which are with small cross-section profiles, the interference between two neighboring laser beams will be avoided. By only measuring the centers of the isolated laser beams, the effects of noise signals, caused by internal reflections of the ICM laser beams, onto the lateral dimension measurements, will be reduced. The reduced effects of the noise signals in the ICM system will improve the accuracy of the measurement. To improve the lateral resolution of the ICM system, more positions should be monitored. However, with more positions being monitored within a certain area, the neighboring monitored positions could be too close to each other that interference between reflected laser beams at these neighboring locations adds noise signals and reduces the accuracy of the ICM measurements. In order to gather information at both of these neighboring positions, the information at these positions must be measured at a different time steps. The time-varying scanning method developed in this thesis sequentially measures these neighboring positions, which are too close to each other, at different time steps. In addition, the time-varying scanning method sequentially measures these neighboring positions with high sampling frequency. The Spatial Light Modulator (SLM) can move the locations of the small laser beams with respect to time. Thus, it enables the ICM to measure the locations (where the locations will cause interference with

the other locations) at different time steps. This can increase the ICM resolution in 2D lateral dimensions by introducing time variance in addition to the 2D spatial dimensions.

**Validation:** An electronic iris system was used to improve the ICM system in this study. This electronic iris system enables generating multiple isolated laser beams and moving these beams with respect to time. The dimensions of parts fabricated by the ECPL process was measured by the ICM system using isolated laser beams with small cross-section profiles to scan across the curing region. The Experiment 5.1.1 validated the hypothesis by showing ICM's ability in measuring parts with multiple heights. The Experiment 5.1.2 validated the hypothesis by showing that ICM is capable for measuring the lateral dimension (width) of the cured part. The measurement errors in all the experiments were within the total possible error discussed in Section 5.2, and all the percentage errors for the experimental measurements were within 15%. With further improvements in ECPL and ICM processes, the possible percentage error could be less than 7.5%. The theoretical resolution could be improved to be  $\pm 36 \mu\text{m}$ , which corresponds to the percentage error less than 4%.

### 6.3 Contributions

Several ICM monitoring systems for the Exposure Controlled Projection Lithography process were available in the literature. However, the existing ICM systems for the ECPL process were only testified to be able to determine the heights for ECPL-fabricated features with flat top. The existing ICM systems only utilize one laser beam to measure the height of the cured part. One approach [24] tried to use a small laser beam to reduce the noise signals caused by internal reflections, and this approach showed the

capability of using a small laser beam to detect edges of the cured part. This approach also proposed an experimentally determined relationship between the interference patterns and the cured part height. However, only one small laser beam in that approach was not able to cover the whole curing region and detect the lateral dimensions. Another approach [40] proposed well-defined optical model to relate the ICM interference patterns captured by the ICM camera with the cured part height. However, no validation experiments have been done to test its ability in lateral dimension measurements, and the large laser beam utilized in that ICM system will suffer from the noise signals caused by internal reflections. The ICM system developed in this study utilized isolated laser beams with small cross-section profiles to scan through the curing region, and the optical model in the literature [40] was used to decode the ICM signals and gather the height distributions of the parts fabricated by the ECPL system.

The primary contribution of this thesis study is to develop a monitoring system that is capable to measure both the height distributions and also the lateral dimensions of the fabricated parts. The contributions could be concluded as follows:

1. It has been shown that the ICM system developed in this study is capable in measuring the lateral dimensions of the cured parts. There exist no validation experiments for the previous ICM systems to prove their ability in determining the lateral dimension and multiple heights of the parts fabricated by the ECPL system. The validation experiments in this study shows that the ICM system is able to measure multiple heights and lateral dimensions of the cured parts with less than 15% error.

2. The electronic iris system developed in this thesis study makes the ICM system able to generate multiple detecting laser beams, whereas all the previous ICM system was only able to utilize a single detecting laser beam with the lever-actuated iris system. The usage of aspheric lenses in the electronic iris system improves the collimation for the ICM laser beam, and the alignment procedure has been summarized in this study. In addition, the electronic iris system allows using the small ICM laser beam to point at (and monitor) a large range of area on the resin platform, whereas the lever-actuated iris used in the previous ICM systems allows the small ICM laser beam to point at (and monitor) a much smaller range of area at the center of the resin platform.
3. The time-varying scanning method developed in this thesis introduces time variance in addition to the spatial variance in the 2D lateral dimensions during the ICM monitoring and measuring process. By sequentially measuring different locations at different time steps with high sampling frequency, this time-varying scanning method is able to measure the neighboring positions that were too close to be measured at the same time step (which the reflected ICM laser at these neighboring positions will interfere with each other and add noise signals) by the previous ICM systems. With these additional positions available to be measured, the time-varying scanning method is able to improve the resolution in lateral directions without physically upgrading the equipment.
4. The thesis provided more matured ICM system, since the ICM system equipment setup was improved, and since the general procedure for ICM system alignment was developed in this thesis.

## 6.4 Future Work

Future work is expected to improve the ICM monitoring system as a robust monitoring system to improve both the accuracy and the precision for the ECPL fabrication process.

For the design for the ICM system setup, the optical path for the ICM laser is expected to be shortened. Keeping all other parameters unchanged, the shorter distance between the SLM and the ICM camera results in larger Fresnel Number which further guarantees that the principles of geometrical optics still applies. Designing the ICM system setup with shorter optical path for the ICM laser will enable further reduction in aperture size in the SLM system, and this will further reduce the minimum cross-section profile for the laser beam that is possible to be generated by the SLM system. This reduction in the laser beam profile will further reduce the noise signals caused by the internal reflections. Using the laser beams with smaller cross-section profile could also result in a “denser” distribution of isolated ICM laser beams, i.e. more isolated ICM laser beams which are located within a certain interested region on the resin chamber, for monitoring the ECPL process. This will further improve the lateral resolution for the ICM system. The ICM camera should also be managed to have more recording frequency (i.e. frames per second). This increased recording frequency could further improve the resolution for height measurements of the ICM system. In addition, the ICM system should be further investigated to enable measuring inclined and curved surfaces. In this study, the validation experiments show ICM’s ability in measuring two heights within one ECPL-fabricated feature. However, as shown in Figure 48, each of the measured sample is assumed to have two flat-top surfaces (with Length 1 and Length 2 for the lengths of these two flat-top

surfaces) for these two heights. Since both the two top surfaces of the feature are parallel to the resin chamber substrate, it was assumed that all the angle of incidence and angle of refractions and reflections are 90 degree for reflections and refractions which happen as the ICM laser propagates and travels through the optical paths  $E_0$ ,  $E_1$ ,  $E_2$ ,  $E_3$ ,  $E_4$ , and  $E_5$  shown in Figure 21. However, if the fabricated part has a curved or inclined surface, the angle of incidence and angle of refractions and reflections, for refractions and reflections happens along the optical path  $E_0 \rightarrow E_3$ ,  $E_0 \rightarrow E_4$ , and  $E_0 \rightarrow E_5$  shown in Figure 21, might not be 90 degree. As a result, if one ICM laser beam  $E_0$ , which travels from the laser source to the top substrate of the resin chamber and have an angle of incidence of 90 degree, propagates through the resin chamber, there might be 4 resultant reflected laser beams, each travels toward a different direction, after refractions and reflections within the resin chamber: a) from a combination of  $E_0 \rightarrow E_1$  and  $E_0 \rightarrow E_2$ ; b)  $E_0 \rightarrow E_3$ ; c)  $E_0 \rightarrow E_4$ ; d)  $E_0 \rightarrow E_5$ . In addition, since these four reflected laser beams (when measuring curved surface) was combined together when measuring a flat-top surface, the intensity of each of these four reflected laser beams would be lower than that of the single and combined reflected laser beam when the ICM was used to measure a flat-top surface. Thus, in order to measure curved or inclined surface using ICM, the reflected laser intensities at the surrounding of the interested positions should also be analyzed. More precise models should be investigated for the ICM laser path when the ICM is used to measure curved surfaces or inclined surfaces of an ECPL-fabricated lens-shaped features.

For signal processing, more effective robust signal noise cancellation algorithms should be developed to improve the quality of the signal. With less noise contained in the ICM signal, the ICM system could determine smaller change in refractive index and thus

improve its resolution in height measurements. In addition, more efficient signal decoding algorithm is expected. Existing signal decoding algorithm used in this thesis study, proposed by Zhao X et al. [41], was able to conduct online, in-situ, and real time measurement for the ECPL fabricated part. However, the limitation of computational power made this algorithm only capable for monitoring 3 positions with acceptable resolution in height measurements without the time-varying scanning method. Since the time-varying scanning method developed in this thesis requires additional steps for SLM frame identification, the computational power requirement is even larger. Thus, in order to make the ICM system in this thesis able to conduct on-line and in-situ measurement, and in order to fit this ICM system into the proposed close loop control [39] which involves even more steps, more research should be done to improve the efficiency in ICM signal decoding.

In addition, more research should be done to interpret the ICM captured interferograms with photopolymerization model. Previous work has been done by Jariwala et al. [9] to qualitatively relate the ICM signal with initial inhibition, cross-linking process and dark-curing. More work should be done to determine quantitative relationships between the dark-curing effect and the given curing radiation profiles. Additionally, comparing and correlating the ICM signals with the COMSOL simulation model presented by Ying et al. [23] forms the validation and calibration experiments for the simulation model, which could further improve the process planning method and could help improve the accuracy of the ECPL fabrication.

## APPENDIX A. MATLAB CODES

### A.1 MATLAB Code for Controlling the SLM

```
function repeatplay(filename,whichmonitor,pausetime,totaltime)
% this function repeatatively plays the video at specified
framerate(i.e.
% specified pause time between frames) for a specified duration (i.e.
% 'totaltime'), on a specified monitor
a = get(0,'MonitorPosition');
hmfr = video.MultimediaFileReader(filename);
hdvp = vision.DeployableVideoPlayer;
hdvp.WindowSize = 'Full-Screen'; % this command set the video to be
displayed in full-screen
hdvp.Location = a(whichmonitor,1:2); % this defines the location where
the video should display.
% use get(0,'MonitorPosition') to get the locations of the monitors
% e.g.: get(0,'MonitorPosition')
%
% ans =
%
%      -1279      150      1280      1024
%           1         1      1680      1050
% then setting hdvp.Location = [1,1] will get the viodeo to show on the
% second screen; setting hdvp.Location = [-1279,150] will get the video
to
% show on the first screen
% see
http://www.mathworks.com/help/vision/ref/vision.deployablevideoplayer-
class.html
% for details
numberofframes = size(hmfr);
total_times_to_play = ceil(totaltime ./ (numberofframes .* pausetime));
for ndx = 1:total_times_to_play
    while ~isDone(hmfr)
        frame = step(hmfr);
        pause(pausetime)
        step(hdvp,frame);
    end
end
end
```

### A.2 MATLAB Code for Convert the Contrastness of ICM Gathered Video

```
%% Updated 2016.10.07
function convertcontrast3(videoname,ContractConvertingFactor)
% note: usually I set the "contract converting factor" to 5
workingDir = tempname;
mkdir(workingDir)
shuttleVideo = VideoReader(videoname);
ii = 1;
```

```

outputnamea = 'Converted_';
outputnameb = 'Contrastfactor_';
outputnamec = num2str(ContractConvertingFactor);
outputnamed = '_';
outputname = [outputnamea outputnameb outputnamec outputnamed
videoname];
% Note: 'Grayscale AVI' in line 23 asks the file to write Uncompressed
AVI
% file with grayscale video. For more information, please see the
following
% website:
% https://www.mathworks.com/help/matlab/ref/videowriter.html
outputVideo = VideoWriter(fullfile(workingDir,outputname), 'Grayscale
AVI');
outputVideo.FrameRate = shuttleVideo.FrameRate;
open(outputVideo)
while hasFrame(shuttleVideo)
    img = readFrame(shuttleVideo);
    img = ContractConvertingFactor .* img;
    writeVideo(outputVideo,img)
    ii = ii+1;
end
close(outputVideo)
workingDir
end

```

### A.3 MATLAB Code for Splitting the ICM Gathered Video

```

% updated 2016.9.9
% This code add the function which can get the corresponding ICM frame
indices for
% each SLM testing matrix, which can fit into Xiayun's code
function frameindexnumber =
Split_read_matrix_moving_video_Without_Reference(videoname,pointrow,poi
ntcolumn, ...
    indicatorrow,indicatorcol,indicatorintensity,framerate)
v = VideoReader(videoname); % read the video
% [numberofdetectingmatrix, pointsineachmatrix] = size(pointrow);
% numberofpoints = pointsineachmatrix; % get the number of points you
want to gather from each frame
[numberofdetectingmatrix, trash] = size(pointrow);
frameorder = 1;
[numberofindicator trash] = size(indicatorrow);
framerate = framerate; % set up the recording frame rate, usually it
equals 35.81
timeperframe = 1 ./ framerate;
result_intensity = cell(numberofdetectingmatrix,2); % initialize the
matrix containing the intensity of each point at each frame
%% Create cell array that contains the frame indices for each SLM
% matrix set
frameindexnumber = {[], [], [], [], [], [], []];
%%
while hasFrame(v)
    video = readFrame(v);

```

```

    findifblurredimage = 0; % set an indicator to see if the video
frame
                                % contains multiple "detecting matrices"
                                % i.e. the image is "blurred"
    whichmatrix = 0; % initialize the indicator to see which detecting
matrix the video frame is reflected to
    for ddx = 1:numberofindicator
        if
mean(mean(double(video(indicatorrow{ddx,1}(1,:),indicatorcol{ddx,1}(1,:
)))) >= indicatorintensity(ddx,1)
            whichmatrix = ddx;
            findifblurredimage = findifblurredimage + 1;
        end
    end
    if whichmatrix ~= 0 && findifblurredimage == 1
        ppointrow = pointrow{whichmatrix,1};
        ppointcolumn = pointcolumn{whichmatrix,1};
%         rrefrow = rrefrow(whichmatrix,:);
%         rrefcol = rrefcol(whichmatrix,:);
        numberofpoints = length(ppointcolumn); % get the number of
points you want to gather from each frame
        [currentrow currentcol] =
size(result_intensity{whichmatrix,1});
        for pointorder = 1:numberofpoints
            result_intensity{whichmatrix,1}(pointorder,currentcol+1) =
double(video(ppointrow(pointorder),ppointcolumn(pointorder)));
%             -double(video(rrefrow(pointorder),rrefcol(pointorder)));
            result_intensity{whichmatrix,2}(pointorder,currentcol+1) =
frameorder;
        end
        frameindexnumber{whichmatrix} = [frameindexnumber{whichmatrix},
frameorder];
    end
    frameorder = frameorder + 1;
end
whos video
[points trash] = size(result_intensity);
% Convert the "x-coordinates" from frame order to real time [in sec]
for ndx = 1:points
    result_intensity{ndx,2} = result_intensity{ndx,2} ./ framerate;
end
figure
hold on
for matrixframenum = 1:numberofindicator
    ppointcolumn = pointcolumn{matrixframenum,1};
    numberofpoints = length(ppointcolumn); % get the number of points
you want to gather from each frame
    rresult_intensity = result_intensity{matrixframenum,1}(:,:);
    ttime = result_intensity{matrixframenum,2}(:,:);
    plot(ttime(1,:),rresult_intensity(1,:))
    hold on
    for pointorder = 2:numberofpoints
        plot(ttime(pointorder,:),rresult_intensity(pointorder,:))
    end
end
hold on
end
xlabel('time (sec)')

```

```
ylabel('intensity')
titlea = videoname(1:end-4);
titleb = ' Results';
title([titlea titleb])
legendsnumber = 1:72;
legendsnumber = legendsnumber';
beforelegendsnumber = num2str(ones(72,1).* 100000);
for ndx = 1: 72
    beforelegendsnumber(ndx,:) = 'Point ';
end
legendtitles = [beforelegendsnumber num2str(legendsnumber)];
legend(legendtitles)
end
```

## REFERENCES

- [1] Kodama, Hideo. "Automatic method for fabricating a three-dimensional plastic model with photo-hardening polymer." *Review of scientific instruments* 52.11 (1981): 1770-1773.
- [2] Hull, Charles W. "Apparatus for production of three-dimensional objects by stereolithography." U.S. Patent No. 4,575,330. 11 Mar. 1986.
- [3] Sun, C. Fang, N. Wu, D. M. and Zhang, X. "Projection micro-stereolithography using digital micro-mirror dynamic mask Sensors Actuators", *Sensors and Actuators A Physical*, 2005.
- [4] Limaye A., Rosen D., 2007, "Process Planning Method for Mask Projection Micro-Stereolithography", *Rapid Prototyping Journal*, 13(2), pp. 76-84.
- [5] Chatwin C., Farsari M., Huang S., Heywood M., Birch P., Young R., Richardson J., 1998, "UV Microstereolithography System That Uses Spatial Light Modulator Technology", *Applied Optics*, 37(32), pp. 7514-22.
- [6] Monneret S., Loubere V., Corbel S., 1999, "Microstereolithography Using Dynamic Mask Generator and A Non-Coherent Visible Light Source", *Proc. SPIE*, 3680, pp. 553-561.
- [7] Jariwala A.S., Zhao X., Ding F., and Rosen D. W., 2007, "A Process Planning Method for Thin Film Mask Projection Micro-Stereolithography," *Proceedings of the ASME 2009 International Design Engineering Technical Conferences & Computers and*

*Information in Engineering Conference*, San Diego, California, USA. DETC2009-8732.

- [8] Zheng X., Deotte J., Alonso M.P., Farquar G.R., Weisgraber T.H., Gemberling S., Lee H., Fang N., Spadaccini C.M. "Design and optimization of a light-emitting diode projection microstereolithography three-dimensional manufacturing system." *Review of Scientific Instruments* 83.12 (2012): 125001.
- [9] Jariwala A.S., Schwerzel R., and David W. Rosen. (2011). "Real-Time Interferometric Monitoring System for Exposure Controlled Projection Lithography." *Proc. of the Solid Freeform Fabrication Sym*, vol. 22, pp. 99-110.
- [10] <http://www.carbon3d.com/> (Accessed March 1, 2017)
- [11] <http://www.carbon3d.com/clip-process> (Accessed March 1, 2017)
- [12] [http://www.rapidshape.de/images/dental/datasheet/RASH\\_Datasheet\\_D40.pdf](http://www.rapidshape.de/images/dental/datasheet/RASH_Datasheet_D40.pdf)  
(Accessed March 1, 2017)
- [13] <http://www.rapidshape.de/products/dental.html> (Accessed March 1, 2017)
- [14] <https://formlabs.com/3d-printers/form-2/> (Accessed March 1, 2017)
- [15] Bunch, Bryan H; Hellemans, Alexander (April 2004). "The History of Science and Technology." *Houghton Mifflin Harcourt*. p. 695. ISBN 978-0-618-22123-3.
- [16] Lightman, Allan J., and Ronald E. Anderson. "Studies of photopolymerization for stereolithography using optical diagnostics." No. 911117. *SAE Technical Paper*, 1991.

- [17] <https://www.zygo.com/?/met/profilers/newview8000/> (Accessed March 2, 2017)
- [18] [https://www.zygo.com/met/profilers/Nexview,NewView8000,ZeGage\\_ObjectiveChart.pdf](https://www.zygo.com/met/profilers/Nexview,NewView8000,ZeGage_ObjectiveChart.pdf) (Accessed March 2, 2017)
- [19] Inoue, Kyosuke, et al. "Local deformation in photo-crosslinked polymer blends monitored by Mach-Zehnder interferometry." *Journal of Polymer Science Part B: Polymer Physics* 43.20 (2005): 2898-2913.
- [20] Tran-Cong-Miyata, Qui, et al. "The roles of reaction inhomogeneity in phase separation kinetics and morphology of reactive polymer blends." *Chinese Journal of Polymer Science* 27.01 (2009): 23-36.
- [21] Jariwala A., Ding F., Zhao X., Rosen D., 2008, "A Film Fabrication Process on Transparent Substrate Using Mask Projection Stereolithography", D. Bourell, R. Crawford, C. Seepersad, J. Beaman, H. Marcus, eds., *Proceedings of the 19th Solid Freeform Fabrication Symposium*, Austin, Texas, pp. 216-229.
- [22] Jariwala A., Ding F., Boddapati A., Breedveld V., Grover M. A., Henderson C. L., Rosen D. W., 2011, "Modeling effects of oxygen inhibition in mask-based Stereolithography", *Rapid Prototyping Journal*, 17(3), pp. 168-175.
- [23] Zhang, Y., Jariwala A., Rosen, D. "Empirical process planning for exposure controlled projection lithography", Master Thesis, Georgia Institute of Technology, School of Mechanical Engineering, Atlanta, 2016.

- [24] Jones, H.H., et al. "Real-time selective monitoring of exposure controlled projection lithography." *Proceedings of the 24th Solid Freeform Fabrication Symposium*, 2013: p. 55-65.
- [25] Zhao, X., Rosen, D.W. "A data mining approach in real-time measurement for polymer additive manufacturing process with exposure controlled projection lithography." *Journal of Manufacturing Systems* (2017).
- [26] Zhao, X., Rosen, D.W. "Real-time interferometric monitoring and measuring of photopolymerization based stereolithographic additive manufacturing process: sensor model and algorithm." *Measurement Science and Technology* 28.1 (2016): 015001.
- [27] Dudi, O., Grubbs, W. T. 1999. "Laser interferometric technique for measuring polymer cure kinetics", *Journal of Applied Polymer Science*, 74, pp. 2133-2142.
- [28] Decker C., "Photoinitiated Curing of Multifunctional Monomers," *Acta Polymerica*, vol. 45, pp. 333-347, Oct 1994.
- [29] Boddapati, A. "Modeling Cure Depth during Photopolymerization of Multifunctional Acrylates," Masters thesis, School of Chemical & Biomolecular Engineering, Georgia Institute of Technology, Atlanta, 2010.
- [30] Boddapati A., Rahane S. B. Slopek R. P., Breedveld V., Henderson C. L., Grover M. A. "Gel time prediction of multifunctional acrylates using a kinetics model," *Polymer*, vol. 52, pp. 866-873, 2011.

- [31] Flory, P. J. "Molecular size distribution in three dimensional polymers. I. Gelation," *Journal of the American Chemical Society*, vol. 63, pp. 3083-3090, Jul-Dec 1941.
- [32] Jariwala A., Jones H., Kwatra A., Rosen D. W., 2013, "Process Planning Method For Exposure Controlled Projection Lithography", *Proceedings of the 24th Solid Freeform Fabrication Symposium*, Austin, Texas, pp. 95-110.
- [33] Jariwala A. S., Rosen D. "Modeling and process planning for exposure controlled projection lithography", P.H.D Thesis, Georgia Institute of Technology, School of Mechanical Engineering, Atlanta, 2015.
- [34] Smith R. J., et al. "Spatially resolved acoustic spectroscopy for selective laser melting." *Journal of Materials Processing Technology* 236 (2016): 93-102.
- [35] Smith R.J., Li W., Coulson J., Clark M., Somekh M.G., Sharples S.D., "Spatially resolved acoustic spectroscopy for rapid imaging of material microstructure and grain orientation," *Meas. Sci. Technol.* 25 (5) (2014) 055902.
- [36] Hirsch M., et al. "Assessing the capability of in-situ nondestructive analysis during layer based additive manufacture." *Additive Manufacturing* 13 (2017): 135-142.
- [37] Lewis A., et al. "In-situ process monitoring and ex-situ part quality assessment of selective laser sintering using optical coherence tomography", *Proceedings of the 27th Solid Freeform Fabrication Symposium*, Austin, Texas, pp. 1397-1411.
- [38] <http://www.ebay.com/itm/Ziess-Cirrus-5000-HD-OCT-/261967321395> (Accessed March 16, 2017)

- [39] Jones H.H., Jariwala A.S., Rosen D.W., "Towards Real Time Control of Exposure Controlled Projection Lithography." *Proceedings of International Symposium on Flexible Automation*, Japan, 2014.
- [40] Zhao X., Rosen D.W., "Parameter estimation based real-time metrology for exposure controlled projection lithography." *Proceedings of the 26th Annual International Solid Freeform Fabrication Symposium*. Austin. 2015.
- [41] Zhao X., Rosen D.W., "Experimental validation and characterization of a real-time metrology system for photopolymerization-based stereolithographic additive manufacturing process." *The International Journal of Advanced Manufacturing Technology*: 1-19.
- [42] Zhao X., Rosen D.W., 2016, "Experimental Validation and Characterization of a Real-time Metrology System for Photopolymerization Based Stereolithographic Additive Manufacturing Process", *The International Journal of Advanced Manufacturing Technology*, pp. 1-19.
- [43] Schwerzel R.E., Jariwala A.S., Rosen D.W., 2013, "A Simple, Inexpensive, Real-Time Interferometric Cure Monitoring System for Optically Cured Polymers," *J. Applied Polymer Science*, Vol. 129, No. 5, pp 2653-2662.
- [44] "LC 2012 Spatial Light Modulator (transmissive)", Accessed Jan. 28 2017, <http://holoeye.com/spatial-light-modulators/lc-2012-spatial-light-modulator/>
- [45] Mglg, "Spherical aberration 2.svg", Wikipedia, Accessed Jan. 29 2017, [https://upload.wikimedia.org/wikipedia/commons/9/92/Spherical\\_aberration\\_2.svg](https://upload.wikimedia.org/wikipedia/commons/9/92/Spherical_aberration_2.svg).

- [46] Zhao C., Jariwala A.S., Rosen David W., "Real Time Monitoring of Exposure Controlled Projection Lithography with Time-varying Scanning Points." *Proceedings of the 27th Solid Freeform Fabrication Symposium*, Austin, Texas, pp. 1126-1144.
- [47] Basler Ace USER'S MANUAL FOR GigE CAMERAS. Exton: Basler, 2016. AcA2500-14gm. Basler, Inc., 01 June 2016. Sec. 8.13. Web. Accessed April 2, 2017. [http://s.baslerweb.com/media/documents/AW00089323000\\_ace%20GigE%20Users%20Manual.pdf](http://s.baslerweb.com/media/documents/AW00089323000_ace%20GigE%20Users%20Manual.pdf)
- [48] "AcA2500-14gm Specifications." Basler AG, 2016. Web. Accessed 15 July 2016. <http://www.baslerweb.com/en/products/cameras/area-scan-cameras/ace/aca2500-14gm>
- [49] Simonin L., et al., "Characterization of heterogeneous structure in a polymer object manufactured by stereolithography with low-frequency microechography." *Journal of Materials Chemistry* 6.9 (1996): 1595-1599.
- [50] Simonin L., Lougnot D. J., "Scanning acoustic microscopy: a tool for measuring crosslinking gradients in photopolymer materials." *Sensors and Actuators A: Physical* 74.1 (1999): 156-160.
- [51] Zhao X., Rosen D., "Process Measurement and Control for Exposure Controlled Projection Lithography," P.H.D Thesis, Georgia Institute of Technology, School of Mechanical Engineering, Atlanta, 2017.